University of Nevada, Reno

Analysis and Modeling of Magnetized Microswimmers: Effects of Geometry and Magnetic Properties

A dissertation submitted in partial fulfillment of the requirements for the degree of Doctor of Philosophy in Mechanical Engineering

by

Farshad Meshkati

Dr. Henry C. Fu/Dissertation Advisor

December 2016

THE GRADUATE SCHOOL

We recommend that the dissertation
prepared under our supervision by

FARSHAD MESHKATI

Entitled

**Analysis and Modeling of Magnetized Microswimmers:
Effects of Geometry and Magnetic Properties**

be accepted in partial fulfillment of the
requirements for the degree of

DOCTOR OF PHILOSOPHY

Henry C. Fu, Ph.D., Advisor

Matteo Aureli, Ph.D., Committee Member

Miles Greiner, Ph.D., Committee Member

Hassan Masoud, Ph.D., Committee Member

Xiaoshan Zhu, Ph.D., Graduate School Representative

David W. Zeh, Ph. D., Dean, Graduate School

December, 2016

Abstract

In recent years, much effort has been placed on development of microscale devices capable of propulsion in fluidic environments. These devices have numerous possible applications in biomedicine, microfabrication and sensing. One type of these devices that has drawn much attention among researchers is magnetic microswimmers—artificial microrobots that propel in fluid environments by being actuated using rotating external magnetic fields. This dissertation highlights our contribution to this class of microrobots. We address issues regarding fabrication difficulties arising from geometric complexities as well as issues pertaining to the controllability and adaptability of microswimmers.

The majority of research in this field focuses on utilization of flexible or achiral geometries as inspired by microbiological organisms such as sperm and bacteria. Here, we set forth the minimum geometric requirements for feasible designs and demonstrate that neither flexibility nor chirality is required, contrary to biomimetic expectations. The physical models proposed in this work are generally applicable to any geometry and are capable of predicting the swimming behavior of artificial microswimmers with permanent dipoles. Through these models, we explain the wobbling phenomena, reported by experimentalists. Our model predicts the existence of multiple stable solutions under certain conditions. This leads to the realization that control strategies can be improved by adjusting the angle between the applied magnetic field and its axis of rotation. Furthermore, we apply our model to helical geometries which encompass the majority of magnetic microswimmers. We demonstrate the criterion for linear velocity-frequency response and minimization of wobbling motion. One approach to improve the adaptability of swimmers to various environments is to use modular units that can dynamically assemble and disassemble on-site. We propose a model to explain the docking process which informs strategies for successful assemblies. Most studies conducted so far are to elucidate permanent magnetic swimmers, but the literature is lacking on analysis of swimmers made of soft ferromagnetic materials. In this work, we develop a model for soft-magnetic microswimmers in the saturation regime in order to predict the swimming characteristics of these types of swimmers and compare to those of hard-magnetic swimmers.

Contents

List of Tables

List of Figures

Chapter 1

Introduction

1.1 Motivation

This dissertation aims to elaborate on modeling and simulation of magnetic microswimmers, micro-scale robots that are capable of generating thrust in the fluid. Micro- and nano-scale swimming robots have been broadly investigated during the past decade due to their numerous applications. Some of these applications include micro-manipulation and micro-fabrication [5] such as scaffold-based tissue engineering [6], drug delivery systems, for example, for the purpose of drug injection into retinal vessels [7, 8], in situ sensing [9], tissue manipulation [7, 10] and in vivo diagnostics in artery [11], brain [12], and cardiovascular system [13] using magnetized particles and MRI machines.

Different types of micro-robots have been devised. Some of them use electrically- and optically-controlled bacteria, such as the microbiorobots developed by Steager *et al.*, controlled by ultraviolet light and electric currents [14]. Some others use magnetically steered swimming cells [15]. Others use external fuels to cause a phoretic propulsive force [16–24] such as the one developed by Paxton *et al.*, which take advantage of a chemical reaction to cause oxygen gradient and induce propulsion [17]. The microswimmers we investigate in this dissertation belong to another broad class of microswimmers: those that are actuated by externally rotating magnetic fields. Although chemically actuated swimmers can move very fast and dielectrophoretically-

manipulated robots can be controlled very precisely, magnetically actuated swimmers have advantages *in vivo*. Chemical fuels such as hydrogen peroxides are toxic in the body; and velocity and directional control are limited by the need to apply chemical gradients [25] or magnetic fields [24]. Dielectrophoretic methods require intricate close-range electrodes and are affected by ionic screening or nearby conductors. However, magnetic fields can provide the necessary energy to a long distance and provide adequate control with minimal health risks.

1.2 Objectives

We report a modeling procedure for magnetically actuated rigid microswimmers. Although magnetized microswimmers have been investigated in the literature, certain fabrication difficulties associated with the complexity of the geometries have hindered the development of these microswimmers. These manufacturing difficulties call for development of simpler geometries. In this respect, we establish the geometric criteria for an effective swimmer through a symmetry analysis. We report the minimum requirements to achieve propulsion and explain the simplest effective geometry.

Our proposed swimmers generate thrust motion under homogeneous, constant strength magnetic fields rotating with a constant angular velocity. We describe a modeling and simulation method that can predict swimming properties such as swimming speed and rotation axis of the swimmer.

Another obstacle towards the utilization of magnetized microswimmers is the limitation in controllability, which is caused due to dynamical bistability of these swimmers under certain conditions. We introduce a method for dynamic stability analysis of swimmers that can be applied to any geometry. We show that multi-stability can be avoided by adjusting certain experimental parameters. This contributes to improvement of the control capacity by allowing us to deterministically choose swimming

speed and direction in a repeated manner.

The majority of the rigid magnetic microswimmers proposed so far have been comprised of helical shapes. We contribute to the controllability of these swimmers by proposing magnetic dipoles and helical geometries that lead to linear velocity-frequency responses. These linear responses facilitate controlling the swimming velocity by only varying the rotational frequency of the magnetic field. We also identify helical geometric requirements for maximizing swimming velocities of these types of swimmers.

Successful utilization of microswimmers for drug delivery and other *in vivo* applications requires them to be able to navigate through various media. In this respect, one of the present obstacles toward successful implementation of microrobotic systems is the lack of versatility to handle different environments. We propose a type of modular microswimmer, consisting of simple spherical particles that can dynamically assemble and disassemble and provide size and shape versatility, which in turn, have an impact on swimming speed. We developed a physical model to explain and improve the assembly process.

From the magnetic properties point of view, the swimming models developed so far only investigate those swimmers made of permanent magnetic materials and paramagnets. While these models are useful, they are not directly applicable to the microrobotic systems that are made of soft magnetic material. For these types of materials (contrary to the hard magnets) the magnetization is a function of the applied magnetic field. The crystal and shape anisotropies often result in nonlinearity within these systems. We develop a physical model that can handle an important category of microswimmers: those that are made from soft ferromagnets with shape anisotropy.

1.3 Context

Many studies have investigated magnetically actuated miniature swimmers, employing various models depending on the type of the swimmer. The majority of the swimmers studied so far can be classified under three main categories: flexible swimmers, swimmers that operate near solid boundaries, and rigid helical swimmers.

Flexible geometries have been the focus of many of the previous studies. among these studies, many utilize classical elasticity models. Kosa *et al.* [26] modeled the motion of a swimming tail as an elastic beam and solved the beam's deflection differential equation to find the acting forces and displacements. Belovs and Cebers [27] used structural mechanics and resistive force theory to simulate the swimming of a flexible ferromagnetic swimmer. Livanovics and Cebers [28] reported on the swimming motion of a flexible filament attached to magnetic dipole. They use Kirchhoff model of the elastic rod and by applying the magnetic torque and boundary conditions at both ends of the filament, they solved for the deflection of the filament. Roper *et al.* [29,30] investigate swimming of an elastic filament which is constructed by self-assembled micron-sized superparamagnetized beads, tethered to red blood cells. They find an equation for the internal magnetic torque on the filament by considering both the external field and dipole-dipole interactions. They established a balance between elastomagnetic and viscous stresses on an infinitesimal element of chain and used resistive force theory to account for the drag forces on the filament. Ogrin *et al.* [31] studied a swimmer comprised of a soft and a hard ferromagnetic particle connected by a linear spring. They used the Stokes approximation to model the hydrodynamics of the particles.

There are also studies that focus on microswimmers that operate close to solid surfaces. For example, Masoud and Alexeev [32] modeled crawling magnetic microcapsules in microchannels. Sing *et al.* [33] designed a swimmer made up of self-

assembled colloidal rotors that can walk along surfaces in the presence of a rotating magnetic field. Tierno *et al.* [34] studied the propulsion of paramagnetic colloidal doublets above a surface, actuated by an external magnetic field. Zhang *et al.* [35] investigated the propulsion of Ni nanowires near complex surfaces. They observed that dissimilar boundary conditions at the two ends of a nanowire can lead to propulsion.

There are also a number of previous studies that investigated rigid geometries, but they are usually focused on particular geometries. Abbott *et al.* [36] modeled a helical magnetic swimmer utilizing resistive force theory and derived equations, expressing the swimming velocity and torque relative to the frequency of the magnetic field. Ghosh *et al.* [2] studied the configuration of helical objects under external torques. They used an ellipsoid to model the precessional motion of the swimmer. They showed that such systems can exhibit bistable traits.

The studies discussed above have been mostly focusing on modeling of either flexible tails or particular rigid geometries. Most of these studies are case specific. For example, researchers have used the resistive force theory to account for the drag forces on slender bodies [36]. On the other hand, our method as explained in chapter 3 and 4, can be harnessed to analyze any rigid geometry in low-Reynolds-number regimes. Additionally, previous studies did not provide generalized approaches toward the geometric requirements for the swimming of magnetically actuated microswimmers. We address this question in chapter 3 through a mathematical investigation of the geometry. Finally, although stability analysis of magnetically driven systems has been studied before in the literature [2,37], those studies have been limited to distinct cases such as ellipsoids. In chapter 4 we introduce a novel stability analysis method that can be applied to a broad range of magnetically actuated swimmers.

In typical experiments done using helical microswimmers, the magnetic field is usually kept constant. In these cases, the direction of swimming is controlled by the direction of rotation of the applied field and the swimming speed is controlled

by the frequency of rotation. It is often beneficial to have a linear correlation between frequency and swimming speed. This can be done by adopting constant axis of rotation; however, for general geometries, the axis of rotation changes as frequency changes while keeping the field strength constant [2, 3, 38]. This change of axis results in nonlinear velocity-frequency response and makes controlling of the swimmers harder. We also address the wobbling behavior that was observed in previous studies. Wobbling happens when the swimmer obtains an axis of rotation which is different from the long axis of the helix. Previous studies claimed that the wobbling can be avoided or minimized if the magnetization is perpendicular to the helical axis [3, 39]. We show that even though wobbling cannot be avoided altogether, there are ideal directions for magnetization that can result in linear velocity-frequency responses. These matters, as well as other questions regarding helical geometries, are addressed in chapter 5.

The concept of modular microrobotics has been previously discussed by Tottori *et al.* [40]. They successfully demonstrated a process to assemble and disassemble helical microswimmers using magnetic and hydrodynamic forces. The helical geometries, though effective for swimming, may not be ideal for modularity since researchers could assemble merely up to three helices. In chapter 6, we show how magnetic beads can be used as building blocks. This allows for much wider range of achievable shapes and sizes. We then describe a model that improves the assembly strategies.

Although models for magnetized microswimmers are available in the literature [39, 41–44], these models may not directly apply to a wide range of microswimmers that are built from soft magnetic materials [3, 45]. In chapter 7, we propose a model that can describe a wide range of microswimmers made from soft magnetic materials.

Chapter 2 covers some fundamental concepts, which are necessary for development of the models in the following chapters. We start with a brief discussion of important terminologies in magnetism, followed by introductory concepts of low-

Reynolds-number hydrodynamics and method of regularized stokeslets.

Chapter 3 encompasses an article [46] published in Physical Review E journal and was coauthored with U Kei, Cheang, Dalhyung Kim and Min Jun Kim from Drexel University and my advisor Henry Chien Fu from the University of Nevada, Reno. My contribution to this manuscript was to perform data analysis and numerical modeling, as well as commenting on and revising the manuscript.

Chapter 4 focuses on the simulation details, stability analysis, wobbling and controllability of swimmers. This chapter was also published as a manuscript [42] to Physical Review E. My contribution to this chapter entailed: numerical simulation, computational stability analysis, data analysis and writeup.

Chapter 5 includes another PRE manuscript [43] specifically about magnetic helical swimmers coauthored with Henry Chien Fu and Mehdi Jabbarzadeh. I contributed to this project by calculating mobility matrices and paper revisions.

In Chapter 6 we investigated modular microswimmers. This work [47] was published in Scientific Reports and was coauthored with U Kei Cheang, Hoyeon Kim, Kyoungwoo Lee, Hnery Chien Fu and Min Jun Kim. My contribution to this project was to formulate the model and analyze its predictions for assembly as well as revising the manuscript.

Chapter 7 deals with soft-magnetic microswimmers. This project is still under development. We present some preliminary results corresponding to these types of swimmers in saturated regime.

Chapter 8 is a brief conclusion for the entire dissertation.

Chapter 2

Background

This chapter aims to set the background necessary for development of the models explained in this dissertation. The models presented incorporate principles of magnetism and low-Reynolds-number fluid dynamics. These two topics are discussed below.

2.1 Magnetism

In this section, some concepts of magnetism which are applicable to our work are presented. We start with relevant definitions and briefly discuss different types of materials from magnetic properties perspective. Then we specifically focus on ferromagnets from which most of the magnetic microswimmers are fabricated.

2.1.1 Definitions

NOTE: The material in this and next chapter follows the presentation of the books *"Introduction to magnetism and magnetic materials"* by David Jiles [48], and *"Introduction to magnetic materials"* by Bernard Cullity [1].

Table 2.1: Principal unit systems used in magnetism

Quantity	Symbol	SI (*Sommerfeld*)	SI (*Kennelly*)	EMU (Gaussian)
Field	$\mathbf{H}$	Am^{-1}	Am^{-1}	*oersteds*
Induction	$\mathbf{B}$	*tesla*	*tesla*	*gauss*
Magnetization	$\boldsymbol{\mathcal{M}}$	Am^{-1}	-	emu/cc
Intensity of magnetization	$\mathbf{I}$	-	*tesla*	-

Magnetic field

The magnetic field is one of the most important concepts in electromagnetism. When a magnetic field is present, it can be identified by the force it exerts on moving electric charges, the force acted on a current-carrying object, the torque acted on a magnetic dipole or by reorientation of electron spins in certain atoms. Magnetic fields can be produced by moving charges or by permanent magnets. In either case, there are moving electrons that cause magnetic field. Magnetic field has both direction and magnitude and therefore, can be represented as a vector field. In this work we denote magnetic field as $\mathbf{H}$. The units of magnetic field are *ampere per meter* (Am^{-1}) in SI and *oersteds* in EMU system.

Note that magnetic field, $\mathbf{H}$ is closely related to the magnetic induction, $\mathbf{B}$ (which will be explained later.) In fact, some references use the term magnetic field for $\mathbf{B}$. Furthermore, there are several conventions used for defining magnetic entities. The most well known conventions in SI system are *Sommerfeld* and *Kennelly*. Table 2.1 summarizes the units of main magnetic quantities in Sommerfeld, Kennelly, and EMU (Gaussian) systems. In this work, all the parameters and equations will be expressed in SI system using the *Sommerfeld* convention unless otherwise specified.

The *Biot-Savart* law predicts the magnetic field caused by moving charges in a

conductor. [48]

$$\delta \mathbf{H} = \frac{1}{4\pi r^2} i \delta \mathbf{l} \times \hat{\mathbf{r}} \tag{2.1}$$

where r is the radial distance from the length element $\delta \mathbf{l}$ and i is the electric current.

Using the *Biot-Savart* law, we can provide an explanation of the unit of the magnetic field. One *ampere per meter* is the magnitude of the magnetic field produced at the center of a circular coil of diameter $d = 1m$, carrying an electric current of $i = 1A$

Magnetic induction

The magnetic induction $\mathbf{B}$ is closely related to the magnetic field $\mathbf{H}$. When a magnetic field is applied, the response of the medium will be through the magnetic induction. The unit of magnetic induction in SI is *tesla* (T). The *Ampere's Force Law* helps us understand magnetic induction better.

$$\mathbf{F} = i\hat{\mathbf{l}} \times \mathbf{B}. \tag{2.2}$$

Equation 2.2 states that if a conductor carrying current i in the unit direction $\hat{\mathbf{l}}$ is placed in a magnetic induction field $\mathbf{B}$, there will be a force per unit length $\mathbf{F}$ acting on the conductor in the direction normal to both $\mathbf{l}$, and $\mathbf{B}$. Hence, the unit *tesla* is the magnitude of the magnetic induction that can cause a $1N$ force on a $1m$ long conductor carrying $1A$ of electric charge.

Magnetic dipole

The two fundamental entities in magnetization are the current loop (the limit when the radius of a current carrying loop goes to zero) and the magnetic dipole (the limit when a pair of magnetic poles get infinitely close to each other). In both cases, a

magnetic moment $\mathbf{m}$ can be associated with the entity. For the case of the current loop, the magnetic moment is given by the product of the area of the loop, A and the electric current in the loop, i. For the magnetic dipole, the moment is given by the product of the pole strength, p and separation distance between the poles, d. It can be shown that the torque on a magnetic dipole is given by

$$\boldsymbol{\tau} = \mathbf{m} \times \mathbf{B}. \tag{2.3}$$

The units of magnetic moment in *Sommerfeld* convention are Am^2. Equation 2.3 shows that the magnetic induction tends to align the dipole such that $\mathbf{m}$ lies parallel to $\mathbf{B}$; hence, when $\mathbf{m}$ and $\mathbf{B}$ are not parallel, there will be a potential energy in the system

$$E_p = -\mathbf{m} \cdot \mathbf{B}. \tag{2.4}$$

Magnetization

We can define the magnetization $\mathbf{M}$ as

$$\boldsymbol{\mathcal{M}} = \frac{\mathbf{m}}{V} \tag{2.5}$$

where V is the volume of the magnetized object. Hence the units of magnetization are the same as the units of the magnetic field (Am^{-1}).

Permeability

The permeability tensor, $\boldsymbol{\mu}$ can be defined as

$$\mathbf{B} = \boldsymbol{\mu}\mathbf{H}. \tag{2.6}$$

Permeability has units of *henries per meter* (Hm^{-1}). In free space and air, because of isotropic properties, the permeability tensor reduces to a scalar, denoted as μ_0. This permeability is a universal constant and its value is $\mu_0 = 4\pi \times 10^{-7} Hm^{-1}$. Note that, in general, μ is not a constant. It is often useful to consider the permeability with respect to the free space permeability. Hence we can also define the relative permeability tensor as

$$\boldsymbol{\mu}_r = \boldsymbol{\mu}/\mu_0. \tag{2.7}$$

Susceptibility

One can establish a relationship between the magnetic field and magnetization using the susceptibility tensor, $\boldsymbol{\chi}$ through

$$\boldsymbol{\mathcal{M}} = \boldsymbol{\chi}\mathbf{H}. \tag{2.8}$$

Depending on the type of material, $\boldsymbol{\mathcal{M}}$ and $\mathbf{H}$ may not have a linear relationship.

Relationship between H, B, and $\mathcal{M}$

It is known that the magnetic induction gets contributions from both the applied magnetic field and the magnetization of the solid material; therefore,

$$\mathbf{B} = \mu_0 \left(\mathbf{H} + \boldsymbol{\mathcal{M}}\right). \tag{2.9}$$

In eq. 2.9, $\mathbf{H}$ is the magnetic field generated outside the material, and $\boldsymbol{\mathcal{M}}$ is the magnetization which is generated inside the solid object.

Relationship between susceptibility and permeability

Considering equations 2.6, 2.7, 2.8, and 2.9, we can derive a relationship between susceptibility and permeability.

$$\boldsymbol{\mu}_r = \boldsymbol{\chi} + \boldsymbol{I} \tag{2.10}$$

In eq. 2.10, $\boldsymbol{I}$ is the identity matrix.

Demagnetization field

Let us investigate a magnetized bar. Since the magnetization outside the bar (in free space) is zero, it can be shown through eq. 2.9 that $\mathbf{H}$ and $\mathbf{B}$ are parallel outside the bar. Inside the bar, however, it can be shown using Ampere's Circuit Law that $\mathbf{H}$ and $\mathbf{B}$ point in opposite directions. This is due to the magnetization of the material.

Since $\mathbf{H}$ and $\boldsymbol{\mathcal{M}}$ point in opposite directions inside the material, it is possible to define a demagnetizing field, $\mathbf{H}_d$ whenever opposite poles are created in a material. It is known that the demagnetizing field only depends on the magnetization of the material and the geometry.

$$\mathbf{H}_d = -\mathbf{N_d}\boldsymbol{\mathcal{M}}. \tag{2.11}$$

Here $\mathbf{N_d}$ is the demagnetizing tensor and mainly a function of the geometry of the magnetized object. For example, the axial (N_a) and radial (N_r) demagnetizing coefficients for a prolate ellipsoid can be calculated from

$$\begin{aligned} N_a &= \frac{1}{R^2-1}\left(\frac{R}{2\sqrt{R^2-1}}\ln\left(\frac{R+\sqrt{R^2-1}}{R-\sqrt{R^2-1}}\right)-1\right) \\ N_r &= \frac{1-N_a}{2}, \end{aligned} \tag{2.12}$$

where R is the ratio of the semi-major axis to the semi-minor axis of the ellipsoid. In the unit system and conventions used in this work, $\mathbf{N_d}$ is dimensionless.

Now that the demagnetizing field is defined, the total field in the object ($\mathbf{H}_{in}$) can be expressed in terms of the applied field $\mathbf{H}_{app}$ and the demagnetizing field.

$$\mathbf{H}_{in} = \mathbf{H}_{app} - \mathbf{N_d}\boldsymbol{\mathcal{M}}. \tag{2.13}$$

2.1.2 Different types of magnetic material

Magnetic materials can be categorized based on their magnetic properties. This chapter is a brief introduction to three major types of magnetic materials: diamagnets, paramagnets, and ferromagnets.

Diamagnets

The differences in magnetic material are usually signified by their bulk susceptibility, χ. Diamagnets tend to have small negative susceptibilities (of the order of 10^{-5}); therefore, they tend to have a magnetic response, opposite to the applied field. This behavior can be explained using quantum models. But heuristically, one can state that this behavior comes from the fact that there are no unpaired atoms in diamagnet orbits and according to Lenz's law, in presence of a magnetic field, a current will be induced in the direction that causes a magnetic field that opposes the change that produced it. Therefore, the response of the orbit will be in the opposite direction of the field.

Some common examples of diamagnets are copper, silver, gold, bismuth, and beryllium.

Paramagnets

These types of materials have small and positive susceptibility ($\chi \approx 10^{-3} - 10^{-5}$); therefore, the magnetic response is aligned with the applied field. This comes from

the alignment of the unpaired electrons with the external magnetic field, causing a supporting response.

Examples of paramagnets are aluminum, platinum and manganese.

Ferromagnets

Ferromagnets have positive and much larger susceptibilities ($\chi \approx 50 - 10000$). Ferromagnets are the most recognized type of magnetic materials. Examples of ferromagnets are iron, nickel, and cobalt.

There are a number of other types of magnetic materials, which are closely related to ferromagnets since they are magnetically ordered (as will be explained later). These include: ferrimagnets, antiferromagnets, helimagnets, and superparamagnets.

For the rest of this text, we will focus on the ferromagnetic material.

2.1.3 Ferromagnetics

Hysteresis

In ferromagnets, neither the magnetic induction nor the magnetization are generally linear with the magnetic field. Moreover, the crystal structure of ferromagnets cause anisotropy which will be explained later. Therefore, nonlinear and hysteretic behavior can be observed when magnetic induction is plotted versus magnetic field strength. Figure 2.1 shows a typical hysteresis loop of a ferromagnetic material. Note that one can also get a hysteresis loop by plotting magnetization versus field strength, but these are essentially equivalent according to eq. 2.9.

Saturation magnetization

It is clear from figure 2.1 that the magnetization of a (nonmagnetized) ferromagnet is initially zero when the field strength is zero. As the field strength is increased, the

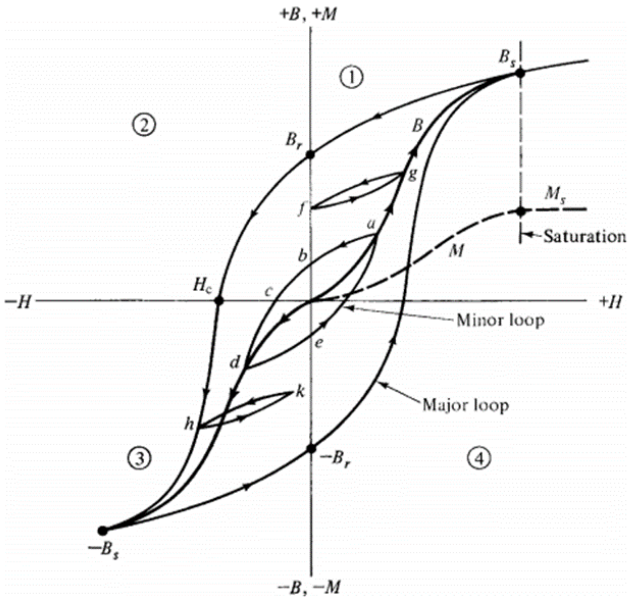

Figure 2.1: Typical Hysteresis loop for a ferromagnet. [1]

magnetization also increases. In the far limit of magnetic strength, the magnetization reaches an asymptotic value called *saturation magnetization* that we denote as $\mathcal{M}_0$. When the material is saturated, all of its dipoles are aligned with the external magnetic field. Note that $\mathcal{M}_0$ only depends on the material; it is not structure sensitive. Another closely related concept is the *spontaneous magnetization*, $\mathcal{M}_s$. Spontaneous magnetization is the value of magnetization within the domains of a material. At temperatures significantly less than the *Curie temperature* (as will be defined later), spontaneous and saturation magnetization are equal.

Remanence

It is clear from the hysteresis loop (figure 2.1) that once a material is magnetized, the removal of the magnetic field will not reduce the magnetization (or the induction) to zero. The remaining induction is called the remanent induction $\mathbf{B}_r$ (see figure 2.1) and the remaining magnetization is called the remanent magnetization $\boldsymbol{\mathcal{M}}_r$. The

term remanence is used to describe the remanent induction or magnetization when the material has been magnetized to saturation before removing the magnetic field.

Coercivity

Since the magnetic induction (and magnetization) of ferromagnets are not generally zero in the absence of magnetic field, one needs to apply a reverse magnetic field to bring the magnetic induction (and magnetization) to zero. This magnetic field is called the coercive field. As with remanence, a distinction can be draw between coercive field for a ferromagnet that was magnetized to an arbitrary level and a ferromagnet which was magnetized to its saturation level. In the case of saturation, the corresponding coercive field is called the coercivity, $\mathbf{H}_c$ as depicted in figure 2.1.

Hard and soft magnets

One way to classify ferromagnets is based on their coercivity. Materials with relatively high coercivity (generally $\mathbf{H}_c \geq 10kAm^{-1}$) are called hard magnets and materials with relatively low coercity (generally $\mathbf{H}_c \leq 1kAm^{-1}$) are considered soft magnetic materials. Historically it was observed that mechanically hard metals such as iron and steel also possessed high coercivity and softer material exhibited lower coercivity; hence, they were named as magnetically hard and soft respectively.

Curie temperature

All ferromagnets when heated up to certain temperatures exhibit paramagnetic behaviors. The temperature at which this transition takes place is called the Curie temperature, T_c. At this temperature, the permeability of the material decreases significantly and coercivity and remanence become zero. In other words, there is no hysteresis involved.

Rayleigh law and low-field behavior

Rayleigh observed that the initial magnetization curve (from the demagnetized state) can be represented using a parabolic equation

$$\mu(\mathbf{H}) = \mu(0) + \nu\mathbf{H} \tag{2.14}$$

and the induction would be

$$\mathbf{B}(\mathbf{H}) = \mu(0)\mathbf{H} + \nu\mathbf{H}^2. \tag{2.15}$$

Rayleigh also showed that small-amplitude hysteresis can be represented by

$$\mathbf{B} = [\mu(0) + \nu\mathbf{H}_m]\,\mathbf{H} \pm \left(\frac{\nu}{2}\right)\left(\mathbf{H}_m^2 - \mathbf{H}^2\right) \tag{2.16}$$

where $\mathbf{H}_m$ is the maximum field at the loop tip.

Molecular Field Theory

Assume that the magnetization of a substance increases with field as represented by curve 1 of figure 2.2. Also assume that the only field acting on the material is a molecular field H_m, proportional to the magnetization:

$$H_m = \gamma\mathcal{M}. \tag{2.17}$$

The mean field theory can explain why ferromagnets are spontaneously magnetized (self-saturating). Equation 2.17 is represented by curve 2 on figure 2.2. These two curves intersect at the origin and point p. In the demagnetized state (at the origin), slightest applied field (for example the earth's magnetic field) can cause the material to be magnetized to state A, but that magnetization would result in a small molecular

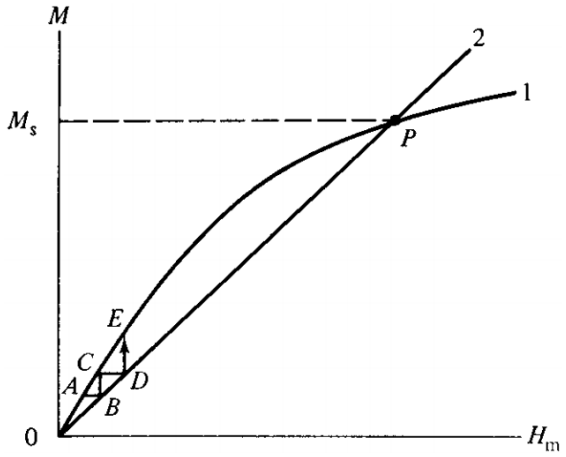

Figure 2.2: Spontaneous magnetization by the molecular field. [1]

field according to eq. 2.17 so we land at point B on figure 2.2. This process will continue until the magnetization reaches the stable state at point p. The value of magnetization at point p is exactly the spontaneous magnetization, $\mathcal{M}_s$. Note that as the temperature increases, the slope of curve 2 on figure 2.2 increase. Therefore, at some temperature, the two curves will no longer intersect at two points and there will not be any spontaneous magnetization. This explains how ferromagnets can turn into paramagnets above a certain temperature (T_c) [1].

Magnetic domains

Mean field theory explains why ferromagnets are self-saturating, but complication arises since one can find demagnetized ferromagnetic material in nature. To answer this objection, Weiss made the assumption that ferromagnets in their demagnetized state are made up of several small regions, called *domains*. Each domain is spontaneously magnetized with $\mathcal{M}_s$, but the directions of these domains are in a way that they result in no net bulk magnetization. Hence, the magnetization process consists of reorienting the domain so that they line up with each other. Figure 2.3 shows this process schematically. In part (a) there is no external magnetic field. The region is

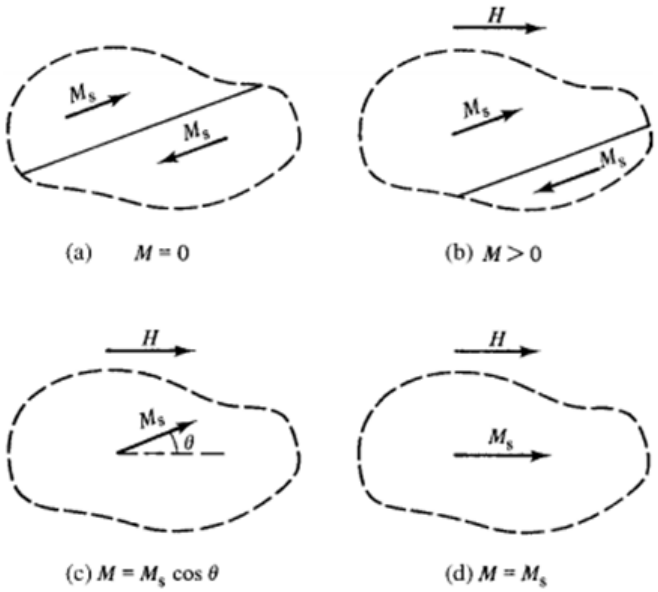

Figure 2.3: Magnetization process in a ferromagnet consisting of two domains. [1]

consisted of two domains each of which has magnetization $\mathcal{M}_s$. They are pointing in opposite direction; hence, yielding a zero net magnetization. In part (b) an external field is applied. In this case, the domain wall moves in such a way that makes the upper domain larger and the lower domain smaller and results in a non-zero net magnetization. In part (c) the external magnetic field keeps increasing until the domain wall moves completely out of the region and the upper domain prevails the whole region. At this moment the net magnetization is equal to the spontaneous magnetization, but the direction is not lined up with the external magnetic field. If we increase the field further, as is the case in part (d), the spontaneous magnetization of the domain will rotate to align itself with the external magnetic field. At this stage, the material is practically saturated.

Magnetic anisotropy

Magnetic anisotropy is one of the most important factors that affect the shape of the hysteresis loop. This means that the magnetic properties are different when

measured in different directions. In this section we investigate two main types of magnetic anisotropy, namely crystal and shape anisotropies.

Crystal anisotropy is intrinsic to the material. When the applied field is not in the direction of the easy axes of the crystal, the magnetization within the domains need to reorient to line up with the external magnetic field as was discussed in section 2.1.3. Since the field must do work against the magnetic anisotropy to rotate the magnetization, there is an energy stored in the crystal. This energy is called the *crystal anisotropy energy*, E. It has been shown that this energy can be expressed as:

$$E = K_0 + K_1\left(\alpha_1^2\alpha_2^2 + \alpha_2^2\alpha_3^2 + \alpha_3^2\alpha_1^2\right) + K_2\left(\alpha_1^2\alpha_2^2\alpha_3^2\right) \tag{2.18}$$

where α values are the *direction cosines* of M_s with respect to the crystal axes and the K values are constants for each material and have units of Jm^{-3}. In most practical cases, we are only concerned with the K_1 terms as higher orders are negligible and K_0 is just a constant and can be neglected when dealing with changes in energy. Also note that the anisotropy energy in eq. 2.18 leads to a torque on the magnetized particle.

Shape anisotropy is another important type of magnetic anisotropy. It can be shown that the magnetostatic energy (the energy of a magnet in its own field) is given by:

$$E_{ms} = -\frac{1}{2}\mathbf{H}_d \cdot \boldsymbol{\mathcal{M}}. \tag{2.19}$$

For a prolate spheroid with semi-major axis c and equal semi-minor axes of length a, which is magnetized to a value M making an angle θ with c, we can further simplify

eq. 2.19 using eq. 2.11.

$$E_{ms} = \frac{1}{2}\mu_0 \mathcal{M}^2 N_c + \frac{1}{2}\mu_0 \left(N_a - N_c\right) \mathcal{M}^2 \sin^2\theta. \tag{2.20}$$

Note that in this equation the first term on the right hand side is not angle-dependent and, therefore, can be neglected when differences in energy states are the matter of concern. If we define the shape-anisotropy constant as $K_s = 1/2\mu_0 \left(N_a - N_c\right) \mathcal{M}^2$, we can rewrite eq. 2.20 as

$$E_{ms} = K_s \sin^2\theta. \tag{2.21}$$

Equation 2.21 describes a uniaxial anisotropy and is similar in form to the anisotropy of hexagonal crystals, which have one easy axis only. This form can be directly derived from eq. 2.18. The anisotropy torque in this case can be found by taking the derivative of eq 2.21 with respect to θ.

2.2 Low-Reynolds-number hydrodynamics

In fluid mechanics, the characteristics of the flow are described using a dimensionless number called Reynolds number. It represents the ratio of the inertial forces to viscous forces in the flow. It is defined as $Re = \rho v L/\mu$ where ρ and μ are density and viscosity of the fluid respectively. v is the swimming velocity and L is the characteristic length of the swimmer. When Reynolds number is much greater than one, the inertial forces are more dominant than viscous force. This occurs for flows caused by large moving objects with high velocities such as airplanes. In the case of miniature swimmers, however, since the characteristic length of the object is of the order of micro- or nano-meters and swimming velocities are relatively low, Reynolds number is significantly smaller than one. A vast range of Reynolds numbers are observed in biological scenarios. On the higher end, for example, a humpback whale

induces Reynolds number of about 10^7, a human swimming in the water would cause a Reynolds number of about 10^5. Reynolds number for smaller animals such as goldfish is about 1 and as we come across smaller creatures such as sperm and *E. Coli*, we observe very small Reynolds numbers, in the order of 10^{-4} to 10^{-5}. This fact establishes a fundamental difference between swimming at micro- or nano-scale from macro-scale. In micro-scale, the viscous forces are the dominating hydrodynamic effect.

The dynamics of an incompressible flow can be described using a set of differential equations, called the Navier-Stokes equations, which expresses the Newton's second law for a fluid element.

$$\begin{aligned} \rho\frac{\mathrm{D}\mathbf{V}}{\mathrm{D}t} &= \rho\mathbf{g} - \nabla p + \mu\nabla^2\mathbf{V} \\ \nabla\cdot\mathbf{V} &= 0 \end{aligned} \tag{2.22}$$

where $\mathbf{V}$ is the velocity, $\mathbf{g}$ is the gravitational accelaration, and p is the absolute pressure.

The microswimmers we conducted research on are about $10\mu m$ in length and they induce Reynolds numbers of about 10^{-5}. For such low Reynolds numbers, inertial effects are negligible relative to viscous effects, so the left side of eq. 2.22 can be neglected. Also, one can use the dynamic pressure to account for gravitational effects. Consequently the above equation will be simplified as:

$$0 = -\nabla p + \mu\nabla^2\mathbf{V} \tag{2.23}$$

Eq. 2.23 is called the Stokes equation and is used extensively in modeling of low Reynolds number situations such as those produced by micro-organisms and microswimmers. Equation 2.23 is linear and reversible, meaning that if the forces

acting on the body are reversed, the velocity at every point in the flow reverses.

Purcell [49] explains that if there is no external force and torque on a swimmer, the motion of the swimmer should be non-reciprocal with time in order to have a net translation. In other words, the motion of the swimmer observed forward in time should look different from its motion observed as played backward in times. This is known as the Scallop theorem, since the opening and closing motion of a scallop at low Reynolds number is time-reciprocal and, therefore, ineffective for swimming.

2.2.1 Method of Regularized Stokeslets

Different computational methods can be used to solve partial differential equations such as Stokes equations. These methods include volume discretization methods (such as finite element, finite difference and finite volume methods) as well as Boundary Element Methods. In problems where the surface/volume ratio is small, BEM methods are usually more efficient in terms of computational resources [50]. BEM methods can be used when the Green's function can be calculated. This usually occurs in problems with linear homogeneous media. In this section, we explain a boundary element method, called the Method of Regularized Stokeslet, to solve the Stokes equation (eq. 2.23) for any geometry.

We start by introducing some fundamental solutions to eq. 2.23. Several fundamental solution to eq. 2.23 are known. One fundamental solution is called the Stokeslet solution and describes the velocity profile at $\mathbf{r}$ due to a point force acting at a specific position $\mathbf{r}_0$.

$$v_i(\mathbf{r}) = S_{ij}(\mathbf{r} - \mathbf{r}_0) f_j \tag{2.24}$$

where:

$$S_{ij}(\mathbf{r}) = \frac{1}{8\pi\mu|\mathbf{r}|}(\delta_{ij} + \frac{r_i r_j}{|\mathbf{r}|^2}) \tag{2.25}$$

and $\boldsymbol{\delta}$ is the Kronecker's delta.

Note that, due to the linearity of eq. 2.23, new solutions can be obtained by adding or subtracting the fundamental solutions. This help us find solutions to numerous situation with more complicated geometries.

To employ the BEM, we use a surface discretization technique to cover up the swimmer with Stokeslets (Fig. 2.4), as explained in the next section. This helps us solve the Stokes equation and find the hydrodynamic characteristics of the flow. In order to do that, we need to take 4 steps. The first step is to write the fluid velocity profile $\mathbf{v}(\mathbf{r})$ in terms of the forces on each Stokeslet $\mathbf{f}^{\alpha}$.

$$\mathbf{v}(\mathbf{r}) = \sum_{\alpha} \mathbf{S}(\mathbf{r} - \mathbf{r}^{\alpha})\mathbf{f}^{\alpha} \tag{2.26}$$

In eq. 2.26, $\mathbf{S}(\mathbf{r} - \mathbf{r}^{\alpha})$ is the Stokeslet matrix that linearly correlates the forces on each surface element to the velocity profile.

The second step is to write the velocities of the surface at Stokeslet positions based on the overall effect of the center of mass translation $\mathbf{V}$, and center of mass rotation $\boldsymbol{\Omega}$. From the equations of rigid-body motion:

$$\mathbf{v}_s^{\alpha} = \mathbf{V} + \boldsymbol{\Omega} \times \mathbf{r}^{\alpha}. \tag{2.27}$$

In eq. 2.27, $\mathbf{v}_s^{\alpha}$ is the velocity of the surface at positions of Stokeslet α, $\mathbf{V}$ is the center of mass translational velocity and $\boldsymbol{\Omega} \times \mathbf{r}^{\alpha}$ accommodates for the velocity of element α due to its rotation relative to the center of mass. Since eq. 2.27 is expressing a linear relation between the surface velocities $\mathbf{v}_s$ and the rigid-body velocities $\mathbf{V}$ and

$\mathbf{\Omega}$, it can be written by means of a linear operator $\mathbf{K}$,

$$(\mathbf{v}_s) = (\mathbf{K}) \begin{pmatrix} \mathbf{V} \\ \mathbf{\Omega} \end{pmatrix}. \tag{2.28}$$

Here $\mathbf{v}_s$ is a $3N \times 1$ matrix corresponding to the x, y, and z components of velocity on all the N Stokeslets and $\mathbf{K}$ is a $3N \times 6$ matrix.

The no-slip boundary condition requires the fluid velocities on the surface of the swimmer, found from the Stokeslets in step one to be equal to the velocities expressed based on the rigid body motion in step 2. Therefore, in step 3, we set these two velocities equal on the solid boundary of the swimmer at locations given by Stokeslet positions. From there, we can solve for the forces on individual Stokeslets by the fluid.

$$(\mathbf{f}_s) = (\mathbf{S})^{-1} (\mathbf{K}) \begin{pmatrix} \mathbf{V} \\ \mathbf{\Omega} \end{pmatrix} \tag{2.29}$$

We introduce a 6×1 matrix $\begin{pmatrix} \mathbf{F}^{ext} \\ \mathbf{T}^{ext} \end{pmatrix}$ to represent the external force and torque on the swimmer. In this work, there are no external forces so there will be only three non-zero elements in matrix $\begin{pmatrix} \mathbf{F}^{ext} \\ \mathbf{T}^{ext} \end{pmatrix}$ which correspond to the x, y, and z components of the external torque due to the external magnetic field.

The total force and torque on the swimmer is expressed as:

$$\begin{aligned} \mathbf{F} &= \sum_{\alpha} \mathbf{f}^{\alpha} \\ \mathbf{T} &= \sum_{\alpha} \mathbf{r}^{\alpha} \times \mathbf{f}^{\alpha}. \end{aligned} \tag{2.30}$$

The linear relation in eqs. 2.30 can be represented by a linear operator $\mathbf{\Lambda}$ such

that:

$$\begin{pmatrix} \mathbf{F} \\ \mathbf{T} \end{pmatrix} = (\mathbf{\Lambda})\,(\mathbf{f}_s) \tag{2.31}$$

As it turns out, the matrix $\mathbf{\Lambda}$ in eq. 2.31 is identical to $(\mathbf{K})^{\mathsf{T}}$.

Finally, since we are working in the low-Reynolds number regime and inertia is negligible, we set the total force and torque equal to zero. These include the hydrodynamic and the external magnetic forces and torques, so:

$$(\mathbf{K})^{\mathsf{T}}\,(\mathbf{f}_s) + \begin{pmatrix} \mathbf{F}^{ext} \\ \mathbf{T}^{ext} \end{pmatrix} = 0. \tag{2.32}$$

Combining this equation with eq. 2.29, we can solve for the center of mass translational and angular velocities, so:

$$\begin{pmatrix} \mathbf{V} \\ \mathbf{\Omega} \end{pmatrix} = \left((\mathbf{K})^{\mathsf{T}}\,(\mathbf{S})^{-1}\,(\mathbf{K})\right)^{-1} \begin{pmatrix} \mathbf{F}^{ext} \\ \mathbf{T}^{ext} \end{pmatrix} \tag{2.33}$$

At each instant in time, the velocities can be calculated and integrated to find the position of the swimmer. Due to the linearity of the problem, the external torque and force acting on the swimmer can be linearly correlated to the center of mass translational and rotational velocities. For rigid geometries, a 6×6 mobility matrix is used to express this linear correlation.

$$\begin{pmatrix} \mathbf{V} \\ \mathbf{\Omega} \end{pmatrix} = \mathscr{M} \begin{pmatrix} \mathbf{F} \\ \mathbf{T} \end{pmatrix} \tag{2.34}$$

where:

$$\mathscr{M} = \left((\mathbf{K})^{\mathsf{T}}\,(\mathbf{S})^{-1}\,(\mathbf{K})\right)^{-1} \tag{2.35}$$

Note since the mobility matrix $\mathscr{M}$ only depends on the fluid properties and swimmer's geometry, for a rigid geometry, eq. 2.34 is constant in the swimmer's frame; therefore, we need to calculate the mobility matrix only once. This will save a lot of computation time and makes our modeling procedure less costly and more efficient.

One caveat about eq. 2.25 is that the function is singular on the surface ($\mathbf{r} = \mathbf{0}$); hence, a modified solution to the Stokes equation has been introduced by Cortez *et al.* [51, 52], which is well-behaved on the boundary. This solution is known as the regularized Stokeslet.

$$S_{ij}^{\epsilon}(\mathbf{r}) = \frac{1}{8\pi\mu}\left(\delta_{ij}\frac{|\mathbf{r}|^2 + 2\epsilon^2}{(|\mathbf{r}|^2 + \epsilon^2)^{3/2}} + \frac{r_i r_j}{(|\mathbf{r}|^2 + \epsilon^2)^{3/2}}\right) \tag{2.36}$$

where ϵ is a diameter cut-off. We use eq. 2.36 instead of eq. 2.25 for a better solution accuracy. Parameter ϵ can be chosen to optimize convergence based on a previous study done by Hyon et al. [53]. This was accomplished by investigating the convergence of swimming velocities by increasing the number of Stokeslets while keeping constant values of $\epsilon/\mathrm{d}s$, where $\mathrm{d}s$ is the distance between each two adjacent Stokeslets. The $\epsilon/\mathrm{d}s$ value that resulted in best convergence was found to be 1 so we can set $\epsilon = \mathrm{d}s$.

2.2.2 Surface discretization

The boundary-element method used to model the hydrodynamics of the swimmer requires the surface of the swimmer to be discretized with a number of surface elements as depicted in Fig. 2.4. To do so, a MATLAB program was developed that would take the number of beads constructing the geometry, the centroid of each bead and their diameters. Then the program would discretize the surface of each sphere individually by making circular cross-sections across the sphere and placing a number of collocation points on each cross-section. Note that we set the distance between each

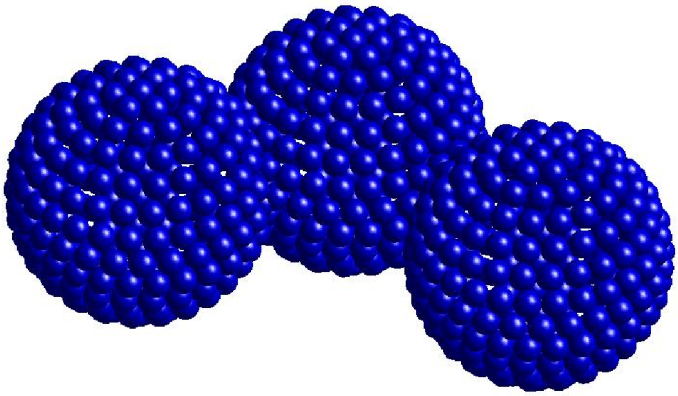

Figure 2.4: Discretized surface of a three-bead swimmer with 717 boundary elements

two circular cross-sections as well as each two adjacent elements on any cross-section to be equal. This parameter (ds) can be adjusted by the user based on the accuracy needed. Cross-sections can be easily defined in a spherical coordinate systems. Angle ϕ can be defined from the z axis. Cross-sections are specified by ϕ changing in $[0,\ \pi]$ with increments defined as $\mathrm{d}\phi = \mathrm{d}s/R$ where R is the radius of the sphere. Therefore, each cross-sectional circle would have a local radius of $r = R\sin(\phi)$. On any given cross-section, angle θ specifies the boundary-element placement. In order to do that, θ needs to vary in $[0,\ 2\pi]$ with increments of $\mathrm{d}\theta = \mathrm{d}s/r$. Fig. 2.5 shows the discretization parameters. Based on this spherical realization, we can formulate the position of each element on the sphere in Cartesian coordinates as:

$$p = [r\cos(\theta), r\sin(\theta), R\cos(\phi)] \tag{2.37}$$

One further step can be taken to maximize the discretization density while keeping a relatively homogeneous distribution. In order to do so, we can rotate the elements on each cross-section by $\mathrm{d}\theta/2$. This staggered configuration puts each element on a cross-section in the mid-way distance between the elements in the neighboring cross-section. After the surface of each sphere is discretized separately, we remove those

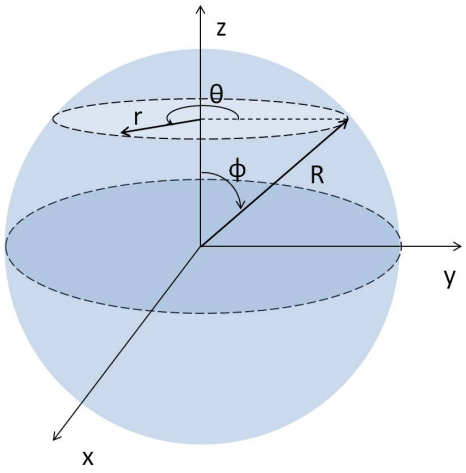

Figure 2.5: Parameters used for discretizing the surface of each sphere

elements of each sphere that would collide with other spheres. This can be achieved by removing all the elements that have shorter distances from other spheres' centroids than the radii corresponding to those spheres.

Chapter 3

Minimal Geometric Requirements for Nano- and Micropropulsion via Magnetic Rotation

3.1 Abstract

Controllable propulsion of micro- and nanoscale devices enhanced with additional functionality would enable the realization of miniaturized robotic swimmers applicable to transport and assembly, actuators, and drug delivery systems. Following biological examples, existing magnetically actuated microswimmers have been designed to use flexibility or chirality, presenting fabrication challenges. Here we show that, contrary to biomimetic expectations, magnetically actuated geometries with neither flexibility nor chirality can produce propulsion, through both experimental demonstration and a theoretical analysis which elucidates the fundamental constraints on micropropulsion via magnetetic rotation. Our results advance existing paradigms of low-Reynolds-number propulsion, possibly enabling simpler fabrication and design of micro- and nanoswimmers.

3.2 Introduction

Nano- and microscale swimming robots have been intensely investigated due to their many possible applications, including micromanipulation and microfabrication [5, 6], drug delivery [7, 8], tissue manipulation [6, 10], and *in situ* sensing [9], such as *in vivo* diagnostics [11–13]. However, difficulties in developing effective propulsion systems have limited their development. Microscale propulsion has been achieved using electrically- and optically-controlled bacteria [14], magnetically steered swimming cells [15], optically-deformed 3-bead systems [54], biflagellate micro-objects [55], and chemically-driven phoretic robots [16–24]. Here we focus on another broad class of robotic microswimmers, those actuated by rotating magnetic fields. Swimming at microscales and below vastly differs from macroscales since viscous damping dominates inertial forces, implying that the hydrodynamics are governed by the zero-Reynolds-number Stokes equation.

Some magnetically actuated micro- and nanoswimmers, such as colloidal walkers [56], rotors [34], nanowires [35], and drillers [57] rely on nearby surfaces for propulsion, which limits their range of applicability. Away from surfaces, in bulk fluids current efforts to make robotic microswimmers have followed biological examples that use either chirality or flexibility to achieve non-reciprocal swimming strokes (*i.e.*, strokes which do not trace the same sequence of configurations forward and backward in time), as required for force- and torque-free biological swimmers by the Scallop theorem [49]. The archetypal chiral strategy is the bacterial flagellum, which is a nearly rigid helix rotating relative to the cell body [58]. The rotating flagellum forms a helical traveling wave so it is not a reciprocal motion. Various artificial helical swimmers [45,59–64] have achieved controlled propulsion under magnetic rotation. The archetypal flexible strategy is the sperm flagellum. Non-reciprocal traveling waves propagate down the flexible flagellum to produce propulsion even for in-plane

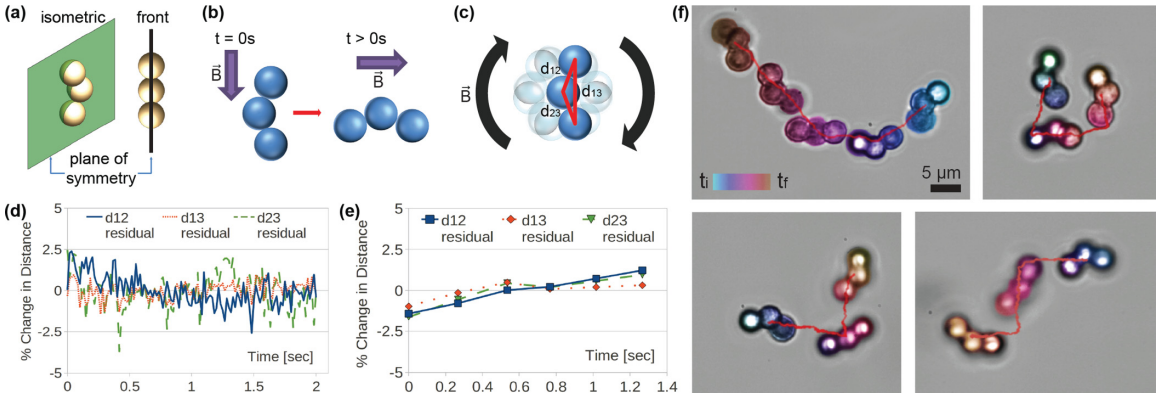

Figure 3.1: Controlled achiral rigid microswimmers. (a) The microswimmers' three-bead structure contains a plane of symmetry making it achiral. (b, c) Schematic of flexibility tests to quantify microswimmers rigidity under (b) impulsive reorientation and (c) steady rotation. The microswimmers structure is measured by the three-dimensional distances between each pair of beads (d_{12}, d_{23}, d_{13}). (d) Percentage change in (d_{12}, d_{23}, d_{13}) during impulsive reorientation. (e) Percentage change in (d_{12}, d_{23}, d_{13}) during swimming with data points captured once per cycle when the swimmer is nearly perpendicular to the line-of-sight. In (d) and (e) distances change less than 5% indicating rigid geometry. f) Trajectories of achiral microswimmers showing swimmers controlled to swim in different patterns and make sharp turns.

(hence achiral) beating patterns [65]. Flexible artificial swimmers include sperm-like swimmers fabricated by DNA linkage [65] and nanowire robots [66, 67]. Based on these biomimetic expectations, challenging fabrication techniques have been required to create chiral or flexible structures.

Here, we show that neither chirality nor flexibility is necessary for propulsion of robotic microswimmers actuated by external rotating magnetic fields away from surfaces. We demonstrate experimentally that an achiral, rigid colloidal microswimmer constructed of three magnetic beads is capable of externally actuated locomotion and is easily maneuvered. We present a theoretical analysis that elucidates the criteria that apply for rigid microswimmers rotated by external torque, establishing fundamental guidelines for designing such micro- and nanoswimmers, which may lead to simpler fabrication of magnetic microswimmers than currently used.

3.3 Methods

3.3.1 Fabrication of achiral microswimmers

We fabricated achiral microswimmers using three ferromagnetic micro-particles (4.40 μm in diameter) linked together, forming the simplest structure for a microswimmer. Naturally, dipole interactions tend to self-assemble the magnetic particles linearly, but we need to make a bent geometry. Chemical streptavidin-biotin binding was used to overcome the linearity of the magnetic self-assembly to form the curved structures necessary for swimming.

The swimmers contain two types of particles. Both of those particles possess the same magnetic properties and are of the same size (4.40 μm). The difference between the two types of beads is the surface coating: one with streptavidin, and the other with biotin. The two are diluted using 30 mg/mL NaCl solution to 0.1 mg/mL and then combined in a reaction mix to make the three-bead microswimmers. The dilution was used to avoid aggregation and increase the probability to create three-bead swimmers. This mixing method introduces randomness to the fabrication process; nonetheless, 3-bead structures can be obtained in this process. Another concern is the rigidity of the swimmers. Some 3-bead structures are prone to deformation while under a magnetic field, while others are relatively rigid. As detailed in Section 3.4.1, only swimmers that have a rigid structure were used for experiments. The binding affiliation between streptavidin and biotin is the strongest among naturally found noncovalent bonds [68, 69], so the swimmers will be relatively unbreakable and rigid [70] while under strong magnetic forces during experiments.

3.3.2 Magnetic control of swimmers far from surfaces

To generate the rotating magnetic field which actuates the achiral microswimmers, we used a control system consisting of three pairs of electromagnetic coils arranged in an approximate Helmholtz configuration (see Appendix), three Kepco power supplies (BOP 20-5M), a National Instruments data acquisition (DAQ) system, a computer, an inverted microscope (Leica DM IRB), and a high speed camera (FASTCAM SA3). Through the use of a DAQ system, the power supplies generate sinusoidal outputs to the coils to create a rotating magnetic field. The high speed camera provides visual feedback and records videos at high frame rates (60-100 fps). The computer is used as interface for the camera and the DAQ system. The three pairs of coils are designed to exert torque on the swimmer without introducing translational force by creating a spatially uniform magnetic field with any specified time-dependent magnitude and direction in a 2 mm $\times$ 2 mm $\times$ 2 mm region. Experiments take place with swimmers immersed in 0.3 g/mL NaCl solution (viscosity of 1 mPa s) in a 3 mm $\times$ 3 mm $\times$ 2 mm ($L \times W \times H$) polydimethylsiloxane (PDMS) chamber, sealed to minimize fluid flow and evaporation, and placed at the center of the Helmholtz coil system mounted on the microscope. The concentration of the NaCl solution was chosen to minimize vertical drift from sedimentation or buoyancy, indicating that the swimmers have density less than 1.2 g/mL. A video is provided showing a swimmer located far from a boundary[1]. At this and higher concentrations, we observed some beads rising due to buoyancy. Out of many imaged videos, we analyzed those where the vertical drift from sedimentation or buoyancy was smallest, so that the swimmer could be kept in the plane of focus. The focal plane was always at least 20 μm from the chamber surfaces. As described later, we also insured that boundary effects were negligible by observing the direction of swimming motion relative to the magnetic

[1]See Supplemental Material at http://link.aps.org/supplemental/10.1103/PhysRevE.90.03300 for video.

field rotation axis: boundary effects make swimmers "roll" along the surface in a direction perpendicular to the rotation axis, while bulk swimmers move in a direction along the rotation axis [38].

3.3.3 Three dimensional image processing and analysis

Changes in structure, swimmer rotation, and swimmer translation are quantified using a three-dimensional tracking algorithm written in MATLAB. Since the structure of the swimmer consists of three spherical beads, the algorithm tracks the three Cartesian positions (x, y, z) of each bead. Planar positions (x, y) are obtained from the centroid of the bead images. Vertical positions (z) are obtained from a standard-deviation-based algorithm that detects the changes in intensity of the beads which correspond to changes in the distance from the focal plane (see autofocusing algorithms reviewed by Sun et al [71]).

3.4 Controlled achiral rigid microswimmers

We fabricated an achiral microswimmer consisting of three ferromagnetic spherical beads (4.40 μm average diameter) linked together, which forms a simple structure for a swimmer (Fig. 3.1a). Dipole interactions tend to lead to linear self-assembly of the magnetic particles, so streptavidin-biotin binding [68, 69] was used to stabilize randomly formed bent nonlinear structures necessary for swimming. Since the centers of the three beads define a plane of mirror symmetry (even for beads of different diameters), the structure is achiral. After assembly, the swimmer has a magnetic dipole, which allows us to manipulate its orientation by applying a spatially uniform, time-dependent magnetic field. The swimmers are large enough that Brownian motion is negligible compared to observed swimming velocities [72].

3.4.1 Rigidity of swimmers

Due to the randomness in the fabrication process, not all microswimmers were rigid. The results reported are for those which do not deform by visual inspection. We further quantified the rigidity of these swimmers by observing their response to time-dependent magnetic fields (Fig. 3.1b and 3.1c and supplemental video[2]). First, to determine whether the swimmer elastically deforms in response to torque, its geometry was observed while it reoriented in response to a time-dependent magnetic field. Swimmers were first allowed to come to equilibrium in a static field, with dipole moment aligned with the field. Then the static field was changed instantaneously to a direction perpendicular to the original direction while maintaining the same magnitude (Fig. 3.1b). This sequence imposes a sudden torque on the swimmer which relaxes as the swimmer reorients to align its moment with the field. During the reorientation, we tracked the distances between the three beads (d_{12}, d_{23}, d_{13}, Fig. 3.1b and 3.1c) in three dimensions. Second, to determine whether the swimmer irreversibly deforms under the torques exerted by rotating fields, we investigated the change in swimmer geometry while it was rotated continuously (as might occur during swimming) about the x-axis (Fig. 3.1c). In this and our swimming experiments, the magnetic field is perpendicular to its rotation axis. We tracked the distance between beads over 6 periods of rotation (1.5 seconds), a time comparable to those used to measure swimming velocities. To minimize error in the z-displacements, we measure the distances once per rotation, when the swimmer-plane is oriented nearly perpendicularly to the line-of-sight. Representative results from the rigidity tests for a visually rigid swimmer are shown in Fig. 3.1d and 3.1e. The lengths d_{12}, d_{23}, and d_{13} change by less than 5%.

The observed $< 5\%$ deformations are not responsible for the propulsion, since as

[2]See Supplemental Material at http://link.aps.org/supplemental/10.1103/PhysRevE.90.03300 for video of flexibility tests.

detailed in Section 3.5 our theoretical model shows that rigid swimmers of similar geometries are capable of propulsion, and the model estimates swimming speeds of the same order of magnitude as those observed.

3.4.2 Swimming and motion control

We observe that the direction of the average velocity is along the rotation axis of the field. The swimmer rotates along a body-fixed axis as it swims. Altering either the angular velocity or magnitude of the applied rotating magnetic field alters the body-fixed rotation axis and the velocity of the swimmer. In contrast, swimmers relying on boundary effects roll in a direction perpendicular to the rotation axis of the field [38], and we use this fact to ensure that the swimmers we observe are not affected by a boundary.

To validate swimming capability and controllability of the achiral swimmer, we changed the strength, direction, and frequency of the rotating magnetic field. The swimming direction can be controlled by manipulating the direction of the magnetic fields rotational axis. To control motion in the xy plane we use a 3D electromagnetic coil system to apply a time-dependent magnetic field $\mathbf{B} = B_i[\sin\theta\sin(\omega t + \phi)\hat{\mathbf{i}} + \cos\theta\sin(\omega t + \phi)\hat{\mathbf{j}} + \sin\omega t\hat{\mathbf{k}}]$ that rotates with angular velocity $\boldsymbol{\omega} = \omega(-\cos\theta\hat{\mathbf{i}} + \sin\theta\hat{\mathbf{j}})$ (which is the average swimming direction). The phase ϕ is either $-90°$ or $90°$. By changing θ the achiral swimmer could make sharp turns at any angle (see SM video). Fig. 3.1f and the supplemental video[3] show several swimming trajectories illustrating directional control. For these trajectories, the rotational frequency and field strength were kept constant, maintaining constant swimming speed. In addition, turning the field on and off or reversing the rotation resulted in starting and stopping motion or direction reversal, respectively.

[3]See Supplemental Material at http://link.aps.org/supplemental/10.1103/PhysRevE.90.03300 for video of controlled trajectory.

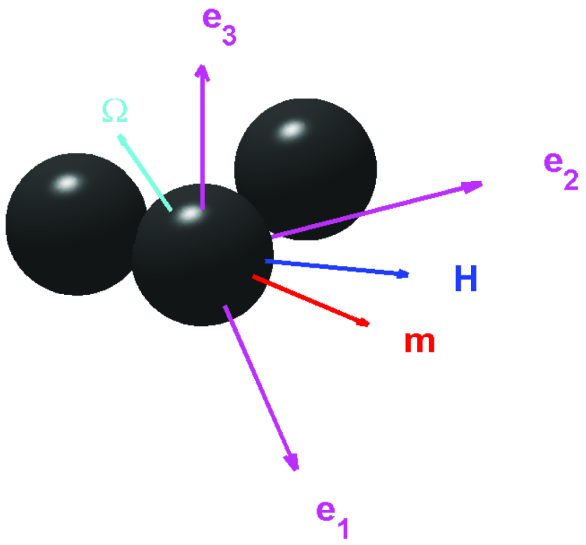

Figure 3.2: Schematic for analyzing swimmer dynamics in body-fixed frame. $\mathbf{e}_1$, $\mathbf{e}_2$, and $\mathbf{e}_3$ are the principal axes of $\mathbf{M}$; $\mathbf{e}_2$ and $\mathbf{e}_3$ are perpendicular to the symmetry planes of the swimmer. For steady rotation, the swimmer angular velocity $\mathbf{\Omega}$ coincides with the magnetic field rotation, and the magnetic field $\mathbf{H}$ and its angular velocity are constant in the body-fixed frame. The magnetic field is perpendicular to its angular velocity.

3.5 Geometrical requirements for swimming

The swimmer described above demonstrates the ability to convert external rotational torque to translational motion without a chiral or flexible geometry. Here we analyze the coupled rotational and translational motion of the achiral swimmer working in a frame fixed relative to the body of the swimmer (principal axes of rotation $\mathbf{e}_1$, $\mathbf{e}_2$, $\mathbf{e}_3$ in Fig. 3.2; $\mathbf{e}_2$ and $\mathbf{e}_3$ are perpendicular to the symmetry planes of the swimmer), and show that such motion is consistent with the principles of low-Reynolds number hydrodynamics.

In the Stokes regime, the translational velocity $\mathbf{v}$ and angular velocity $\mathbf{\Omega}$ are

related to the force $\mathbf{F}$ and torque $\mathbf{N}$ on the swimmer by the 6×6 mobility matrix [73]:

$$\begin{pmatrix} \mathbf{v} \\ \boldsymbol{\Omega} \end{pmatrix} = \begin{pmatrix} \mathbf{K} & \mathbf{C} \\ \mathbf{C}^{\mathsf{T}} & \mathbf{M} \end{pmatrix} \begin{pmatrix} \mathbf{F} \\ \mathbf{N} \end{pmatrix} \tag{3.1}$$

where the 3×3 submatrices $\mathbf{K}$, $\mathbf{M}$, and $\mathbf{C}$ relate the translational velocity and force, rotational velocity and torque, and translational velocity and torque, respectively.

For a swimmer with permanent magnetic dipole $\mathbf{m}$, the torque $\mathbf{N}$ on the swimmer due to the external field is $\mathbf{N} = \mathbf{m} \times \mathbf{H}$, where $\mathbf{H}$ is the magnetic field, and for the uniform fields in the experiment there is no net external force. Therefore the instantaneous angular velocity is

$$\boldsymbol{\Omega} = \mathbf{M}(\mathbf{m} \times \mathbf{H}) \tag{3.2}$$

In general, as the swimmer and the external field rotate independently, the orientation of $\mathbf{H}$ changes relative to the body-fixed frame. However, a steady-state solution arises if the swimmer angular velocity $\boldsymbol{\Omega}$ is equal (in magnitude and direction) to the magnetic field rotation $\boldsymbol{\omega}$.

Now assume that rotational dynamics are in steady-state, as is the case when the swimmers are observed to rotate with the field. Then the translational velocity produced by the external torque is

$$\mathbf{v} = \mathbf{C}(\mathbf{m} \times \mathbf{H}) \tag{3.3}$$

which like the angular velocity is time-independent in the body-fixed frame. Generically, an object with constant body-fixed $\mathbf{v}$ and $\boldsymbol{\Omega}$ moves in circular or helical trajectories [53]. A net translational swimming velocity requires a helical trajectory, for which $\mathbf{v} \cdot \boldsymbol{\Omega} \neq 0$. *Thus, the minimal criteria for swimming are that the swimmer*

rotation $\mathbf{\Omega}$ *(eq 3.2) is equal to the field rotation* $\boldsymbol{\omega}$*, and* $\mathbf{\Omega} \cdot (\mathbf{C}(\mathbf{m} \times \mathbf{H})) \neq 0$.

A necessary condition for swimming is that $\mathbf{C}$ is nonzero. Based on standard symmetry analyses [73], geometries with axisymmetry or three perpendicular mirror planes of symmetry have $\mathbf{C} = 0$ and no swimming, but geometries with up to two perpendicular mirror planes of symmetry can have nonzero $\mathbf{C}$ and produce swimming. In particular, swimming is possible for rigid, achiral geometries. To be concrete, consider a swimmer composed of three equally-sized beads such as those fabricated for our experiments (Fig. 3.1a). For this geometry, symmetry analysis reveals that $\mathbf{M}$ and $\mathbf{C}$ take the form [73]

$$\mathbf{M} = \begin{pmatrix} M_1 & 0 & 0 \\ 0 & M_2 & 0 \\ 0 & 0 & M_3 \end{pmatrix}; \qquad \mathbf{C} = \begin{pmatrix} 0 & 0 & 0 \\ 0 & 0 & C_{23} \\ 0 & C_{32} & 0 \end{pmatrix} \tag{3.4}$$

referred to the body fixed axes labeled $\mathbf{e}_1$, $\mathbf{e}_2$, $\mathbf{e}_3$ in Fig. 3.2[4]. We also verified the form of the mobility matrix by explicit calculation for rigid bodies composed of beads of diameter 4.40 μm using the method of regularized Stokeslets [51–53] (see Appendix for details).

Substituting these mobility matrices into eqs 3.2 and 3.3 shows that for this achiral swimmer, the torque must have both 2- and 3-components in order for swimming to be possible. This implies that $\mathbf{m}$ cannot lie along either the 2 or 3 directions, which are the directions perpendicular to the symmetry planes of the swimmer. Solving eqs 3.2 and 3.3 explicitly for a geometry corresponding to our achiral 3-bead swimmers confirms that under external rotating torques, such geometries swim with the order 1 μm/s speeds observed in our experiments (see Appendix for details).

[4]Note that this form of nonzero $\mathbf{C}$ is also consistent with the example of the achiral impeller given by Happel and Brenner.

Note that the propulsion of our swimmers is consistent with the Scallop theorem and kinematic reversibility of the Stokes equations: as a rigid body, our swimmers do not undergo swimming deformations and instead are actuated by a nonreciprocal external torque. Here we point out that the chirality employed in previous examples of rigid magnetically rotated swimmers is not necessary to have nonzero $\mathbf{C}$ and hence swimming.

If a steady solution to eq 3.2 exists ($\boldsymbol{\Omega} = \boldsymbol{\omega}$), it depends on both the frequency of rotation and the strength of the magnetic field. An important timescale of the rotational dynamics is the typical timescale for rotation of the swimmer due to an external field of magnitude $|\mathbf{H}|$, which is determined by balancing viscous rotational drag against the external torque. From eq 3.2, the timescale is given by $T_{viscous} = (||\mathbf{M}|||\mathbf{m}||\mathbf{H}|)^{-1}$, where $||\mathbf{M}||$ is the typical magnitude of rotational mobility of the particle. If $T_{viscous}$ is short compared to the timescale of variation of the magnetic field ($T_B = 2\pi/\omega$), then the swimmer is in a quasistatic regime, with its magnetic dipole always nearly aligned with the external field. If $T_{viscous}$ is much longer than T_B, then the swimmer cannot rotate quickly enough to follow the magnetic field, and the swimmer will not rotate steadily. For steady-state solutions in the intermediate regime the dipole is not aligned with the external field, producing enhanced torques, hence the rotation axis of the swimmer varies.

3.6 Qualitative predictions and experiments

To satisfy eq 3.2 for a given ω, the magnetic field $\mathbf{H}$ and its rotation vector $\boldsymbol{\omega}$ must take specific orientations relative to the swimmer, which varies as ω varies. Since $\boldsymbol{\Omega} = \boldsymbol{\omega}$, the direction of $\boldsymbol{\omega}$ also sets the swimmers rotation axis as well as the direction of average swimming translation. Frequency dependent rotational axes have also been observed and modeled for magnetically actuated swimmers and gyroscopes both in

Table 3.1: Linear regression values for the 7 microswimmers in Fig. 3.3(b)

	swimmer						
	1	2	3	4	5	6	7
Slope	0.4454	0.3770	0.3435	0.2972	0.6614	0.4567	0.3492
R^2	0.9309	0.9799	0.8567	0.9745	0.9989	0.9662	0.9729

bulk fluids and near surfaces [2, 37, 38, 41, 57]. Together, these considerations make qualitative predictions that can be checked experimentally.

First, no swimming results if the torque is perpendicular to one of the planes of mirror symmetry (i.e., along $\mathbf{e}_2$ and $\mathbf{e}_3$) or along $\mathbf{e}_1$, in which case the rotational axis is also along $\mathbf{e}_1$, $\mathbf{e}_2$, or $\mathbf{e}_3$. In our experiments we indeed observe that the swimmers' rotation axes change as we change the rotation frequency (representative result in Fig. 3.3a) and that the swimmers only swim when they rotate around an axis which is not $\mathbf{e}_1$, $\mathbf{e}_2$, or $\mathbf{e}_3$.

Second, examination of eq 3.2 shows that constant rotation and field directions satisfy eq 3.2 if the rotation frequency and magnetic field strength are increased proportionally. In that case, eq 3.3 implies the swimming speed increases linearly with the frequency. This linear relationship was observed experimentally (Fig. 3.3b). We tracked seven different swimmers while the frequency and magnetic field strength were increased proportionally (Fig. 3.3b). During the experiments, the swimmers were all controlled to swim in the positive x direction. For swimmers 1-7, the velocity-frequency data had linear fits through the origin with R^2 ranging from 0.8567 to 0.99894 (Table 3.1). The linear relation was confirmed for a variety of frequency-to-magnetic field strength ratios (Table 3.1). Since our fabrication process results in random geometries, each swimmer has a different geometry and hence a different swimming speed. Nonetheless, all demonstrate the linear relationship predicted by our theory.

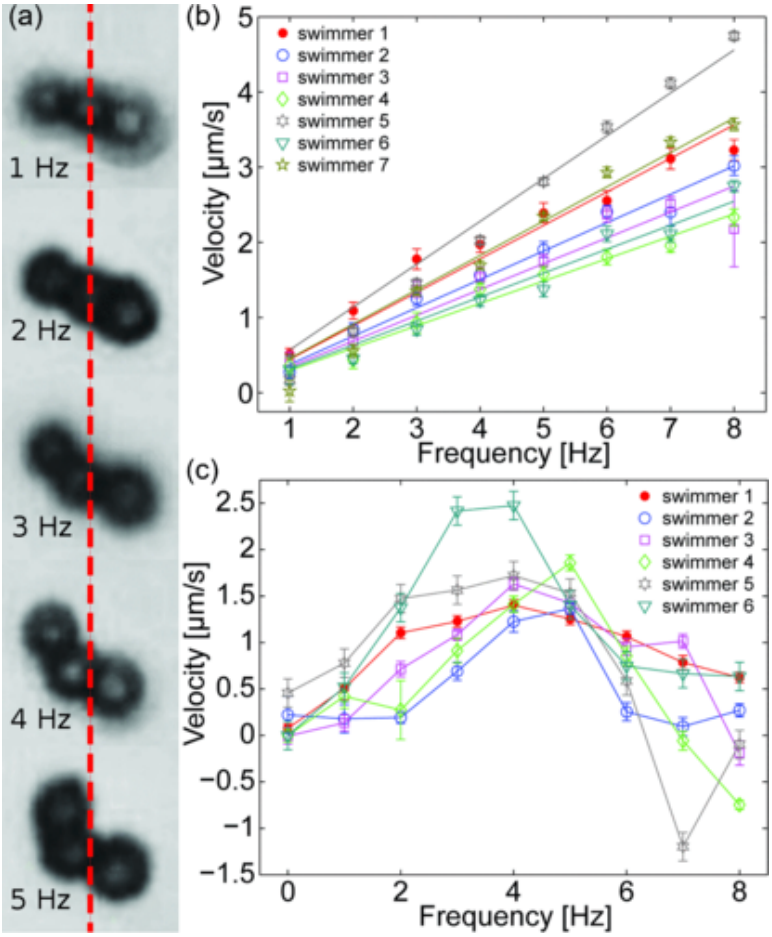

Figure 3.3: Response of swimmer to rotation frequency. (a) The rotational axis (demarcated by red dashed line) changes relative to swimmer's orientation as rotation frequency changes with constant field strength. The swimmers rotation transitions from a symmetrical axis (low frequencies) to a non-symmetrical axis (high frequencies). (b) Swimming speed of seven different achiral microswimmers as frequency and field strength are varied with their ratio held constant. Equation 3.2 predicts a linear relation; linear fit data and ratio of frequency to field strength are reported in Table 3.1. Due to the random fabrication process, each swimmer has a different geometry hence different swimming speed. (c) Swimming speed of the six different microswimmers as frequency is varied for constant field strength, including the microswimmer in (a) shown as swimmer 6. Error bars in (b) and (c) denote standard errors estimated from position uncertainty in image analysis and observation time used to measure velocity.

Third, if the frequency is increased while the magnetic field strength is held constant, the swimmer body-fixed rotation axis changes, leading to a complicated nonlinear dependence of swimming speed on frequency. A supplemental video shows this behavior for one swimmer[5]. In Fig. 3.3c, we show the swimming speed for 6 microswimmers as a function of frequency while magnetic field strength is held constant. In contrast to Fig. 3.3b, the relationship between swimming speed and frequency is nonlinear and markedly non-monotonic. Note that our analysis assumed a permanent dipole, which approximates the magnetic moment of a soft ferromagnet under saturating fields when the direction of the magnetic field is fixed relative to the swimmer body. In the experimental case, the direction of the field changes as the rotation axis changes. Therefore some of the nonlinearity in Fig. 3.3b results from changes in the moment as the rotation axis changes under frequency. However, the changes in rotation axis play a key role in driving the nonlinearity in the context of our analysis, as can be seen from the behavior of the swimmer shown in Fig. 3.3a (corresponding to swimmer 6 in Fig. 3.3c). For frequencies less than or equal to 2 Hz, the swimmer rotates near axis $\mathbf{e}_1$, and accordingly the swimming velocities are small. Between 3 Hz and 5 Hz, the swimmer rotates around non-principal axes, and there is appreciable propulsion. At 6 Hz, the swimmer rotates near axis $\mathbf{e}_2$, and the swimming velocity is small again. Above 7 Hz, the swimmer does not rotate steadily in synchrony with the magnetic field, hence 7 Hz is the step-out frequency.

3.7 Discussion

Previous work on robotic microswimmers focused on flexible or chiral structures to generate propulsion; here, our achiral microswimmers have shown that neither is nec-

[5]See Supplemental Material at http://link.aps.org/supplemental/10.1103/PhysRevE.90.03300 for video of changing rotation axis.

essary. Our analysis of the achiral microswimmer provides a framework to describe the coupled rotational and translational motion of magnetically rotated microswimmers of arbitrary geometries, as well as the minimal criteria for propulsion of rigid bodies under external torque. Applying this framework to design artificial microswimmers without chirality may lead to simpler fabrication methods than currently used for helical or flexible micro- and nanoswimmers, advancing their development for numerous applications. Although the particular swimmers demonstrated here are not faster than previously fabricated microrobots, our work expands the space of geometries to be considered for optimization of swimming performance, thus opening possibilities for more effective propulsion as well.

3.8 Acknowledgments

We thank Hoyeon Kim for help in system setup. This work was funded by National Science Foundation (CMMI 1000255) and Army Research Office (W911NF-11-1-0490) awards to M. Kim, by National Science Foundation awards (CBET-1067798 and CBET-0967510) to H. Fu, and by a National Science Foundation Graduate Research Fellowship (NSF-GRF) awarded to U Cheang.

3.9 Appendix A: Magnetic field produced by approximate Helmholtz coils

The Helmholtz coils in this study are arranged in a slightly different configuration than that of a normal Helmholtz coil. Conventionally, the distance between two coils of the same size is the radius of the coils, which creates a near-constant magnetic field in the central region between the coils. In this study, the distance between each pair of coils is equal to the outer diameter of the coils plus the thickness for the coil, which

allows a cube-like configuration for the 3D coil system and fits within the geometrical constraints of the microscope while maintaining the desired characteristics of the Helmholtz configuration. In order to validate the magnetic field strength as well as the field profile, a finite element method was used to model the coil system in COMSOL Multiphysics. The finite element model simulated the magnetic field using two pairs of coils producing a magnetic field with x- and y- components, generating a static magnetic field in the xy plane. The approximate Helmholtz coil system produces a near-constant magnetic field at the center region of the coil system within which the magnetic flux has less than 2% variation; this region is indicated in Fig. 3.4 by the red box marking an area approximately 2 mm by 2 mm. The magnetic field strength (mT), rotational direction of the magnetic field, and rotational frequency (Hz) of the field generated by the coils are controlled through LabVIEW. The simulation indicates a field strength of 5.06 mT when a current of 1 A passes through the coils, which matches the experimentally measured value of approximately 5 mT. According to the Biot-Savart law, the field strength scales linearly with the applied current; this is also validated with the simulated model and experimental measurements.

3.10 Appendix B: Explicit calculation of mobility matrix

To verify the results for the symmetry analysis of the submatrix $\mathbf{C}$ of the mobility matrix, we numerically calculate the mobility matrix for rigid bodies composed of three beads by using the method of regularized Stokeslets [51–53]. The surface discretization used 717 regularized Stokeslets (Fig. 3.5a). To find the mobility matrix, we calculate the force and torque on the swimmer for prescribed rigid-body translations in each of the cartesian directions and for prescribed rigid-body rotations along

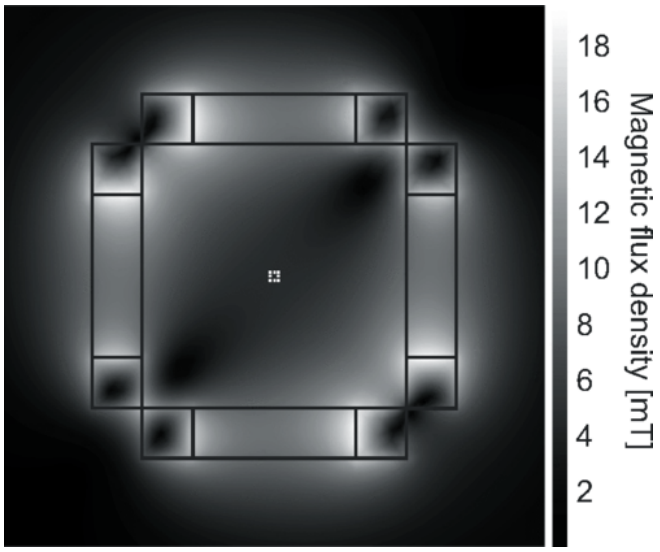

Figure 3.4: Modeled magnetic field. Density plot of magnetic field in xy plane created by the coil system modeled using COMSOL Multiphysics. The small box at the center shows the area where the magnetic field is near-uniform ($< 2\%$ variation).

each of the cartesian directions. This yields the resistance matrix, which is the inverse of the mobility matrix.

We calculate $\mathbf{C}$ for two cases. First, we consider the fully symmetric case with three beads of radius 4.40 μm, with centroids of the beads located 8.80 μm apart, which has two perpendicular planes of mirror symmetry. We verified that when the origin is taken to be the center of reaction, the form agrees with that of the symmetry analysis (Eq. 3.4) up to machine precision.

Second, because irregularities during fabrication can produce less symmetric three bead swimmers, we also calculate $\mathbf{C}$ for three beads of different sizes or with different lengths between their centroids, which produces structures with only a single plane of mirror symmetry, the plane containing the centroid of the three beads. In that case,

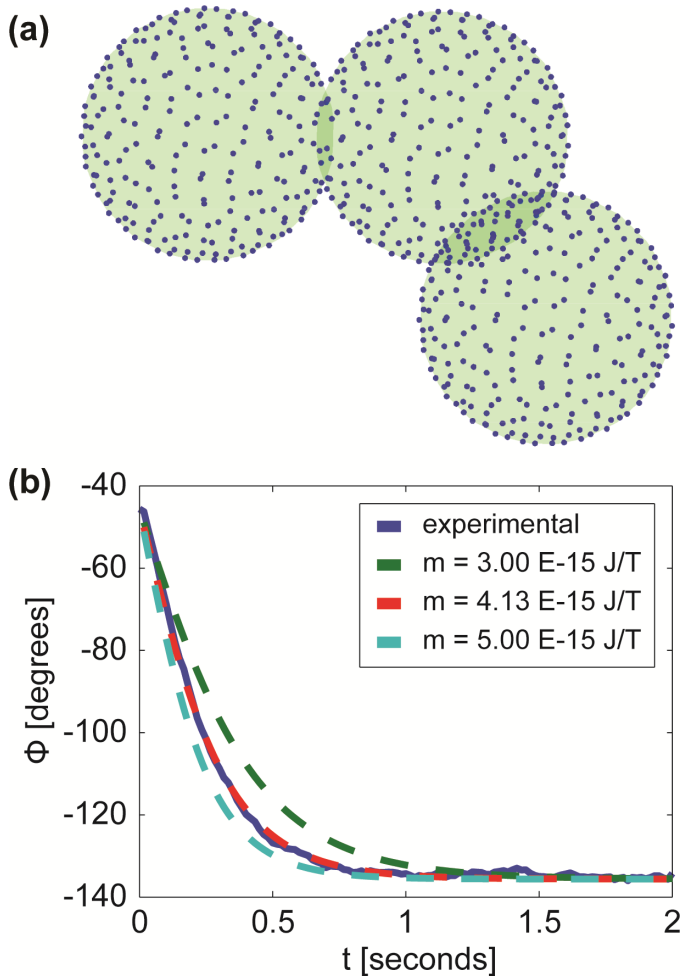

Figure 3.5: (a) Schematic of discretized surface of the swimmer. Each of the 717 points represents a regularized Stokeslet on the surface of the swimmer. (b) Angular reorientation of the swimmer during the reorientation test (solid blue line), along with simulated angular reorientation for different magnitudes of the magnetic dipole (green dotted, red dashed, turquoise dash-dotted lines). The best fit corresponds to a moment of 4.05×10^{-15} J/T.

the symmetry analysis of Happel and Brenner [73] implies that $\mathbf{C}$ takes the form

$$\mathbf{C} = \begin{pmatrix} 0 & 0 & C_{13} \\ 0 & 0 & C_{23} \\ C_{31} & C_{32} & 0 \end{pmatrix}. \tag{3.5}$$

Again, the numerically calculated mobility matrices for these less symmetric geometries, including geometries deduced from experimental image analysis, have the form predicted by symmetry analysis.

3.11 Appendix C: Calculated swimming speeds

We used the mobility matrices to calculate the swimming speed for a 10.12 mT magnetic field rotating at 4 Hz by solving Eqs. 3.2 and 3.3 numerically. The calculation requires a measurement of the magnetic dipole. The random fabrication process means that each swimmer has a different dipole magnitude and direction, but to obtain an estimate of swimming speeds, we estimated the moment via the response of a single swimmer to the reorientation experiment used to test rigidity (Fig. 3.1b). The magnetic field strength in this experiment was 2.53 mT. The direction of the magnetic moment was determined from the initial and final orientations of the swimmer. The magnitude of the moment was obtained by modeling the rotation dynamics using eq 3.2 and the mobility matrix calculated above. We found that a moment of 4.05×10^{-15} J/T provided the best fit to the reorientation dynamics, as measured by the sum of squared residuals (Fig. 3.5b). For this magnitude of dipole moment in a variety of directions, and a variety of three-bead swimmer geometries, we found that swimming speeds had typical orders of magnitude of $1\ \mu$m/s.

Chapter 4

Modeling Rigid Magnetically Rotated Microswimmers: Rotation Axes, Bistability, and Controllability

4.1 Abstract

Magnetically actuated microswimmers have recently attracted attention due to many possible biomedical applications. In this study we investigate the dynamics of rigid magnetically rotated microswimmers with permanent magnetic dipole. Our approach uses a boundary element method to calculate a mobility matrix, accurate for arbitrary geometries, which is then used to identify the steady periodically rotating orbits in a co-rotating body-fixed frame. We evaluate the stability of each of these orbits. We map the magnetoviscous behavior as a function of dimensionless Mason number and as a function of the angle that the magnetic field makes with its rotation axis. We investigate the wobbling motion of these swimmers by investigating how the rotation

axis changes as a function of experimental parameters. We show that for a given magnetic field strength and rotation frequency swimmers can have more than one stable periodic orbit with different rotation axes. Finally, we show that one can improve the controllability of these types of microswimmers by adjusting the relative angle between the magnetic field and its axis of rotation.

4.2 Introduction

Swimming microrobots have been extensively studied during the past decade. These micro- and nano-swimmers have numerous biomedical applications such as drug delivery [7, 8], micro-manipulation [5, 6], *in situ* sensing [9], *in vivo* diagnostics [11–13], and tissue manipulation [6, 10]. Recent studies have focused on various methods of powering and controlling micro- and nano-swimmers. One group of microswimmers are those that are powered using external fuels to cause a phoretic propulsive motion by a chemical reaction [16–24]. Another category are those that use electrically and optically controlled bacteria [14]. In this paper we concentrate on yet another class, those swimmers that are actuated and controlled using external magnetic fields.

Among those swimmers that use external magnetic fields to generate propulsion, we focus on those that are rotated or oscillated by magnetic torques, rather than pushed by magnetic field gradient forces (e.g., [11]), since the former is a more effective strategy at the microscale and below [36]. Some magnetically rotated swimmers have been designed to work near solid surfaces [34, 35, 56, 57], rolling along the surface for propulsion. Our focus, however, is on more versatile micro-swimmers that can swim in the bulk fluid and do not require the presence of a nearby surface. Some previous realizations of these types of magnetically actuated swimmers have emulated the flexible flagella of sperm [65–67]. These swimmers are propelled through the fluid by traveling waves caused by the waving motion of their flexible flagella. Other

realizations have emulated the rigid helical flagella of bacteria. These magnetized helical swimmers are actuated by externally rotating magnetic fields and exhibit a corkscrew type of motion [45, 59–64]. Recently, we have also shown [46] that a broad class of nonhelical geometries, including achiral geometries, are capable of propulsion when rotated by an external magnetic field. Thus, it is of interest to have modeling methods which can treat arbitrary geometries.

In this study we present a modeling method for rigid magnetically actuated swimmers that allows accurate consideration of any geometry. In this paper, we employ our approach to address two important issues in the dynamics of these swimmers: 1) wobbling, or the change in rotation axis of swimmers as the driving magnetic field amplitude or frequency changes, and 2) bistability, the existence of more than one stable rotation axis for a given magnetic field amplitude or frequency.

Some previous studies on helical artificial swimmer have reported wobbling and tumbling motion, in which the helix rotates about an axis different from its longitudinal helical axis. Peyer *et al.* [38] reported wobbling at lower frequencies, with a frequency-dependent precession angle. They also found that this wobbling motion enhances the undesirable sideways drift due to wall effects. Ghosh *et al.* [2] also observed tumbling (rotation about an axis perpendicular to the helical axis) and wobbling in helices magnetized to have magnetic moments which were not perpendicular to the helical axis. In theoretical work Man and Lauga [41] investigated the transtion from tumbling to wobbling behavior as a function of the dimensionless Mason number, and showed that the precession angle is proportional to the magnetic field, and inversely proportional to frequency and length for a nearly straight helix. Peters *et al.* [3] attributed wobbling motion to the non-perpendicularity of the easy axis of magnetic dipole moment to the long axis of the helix. They experimentally illustrated that aligning the easy axis perpendicular to the helical axis results in a wobbling-free swimming and significant increase in performance of the swimmer.

In their study, Ghosh *et al.* [2] also observed bistability for helices. Experimentally, they observed dynamical switching between two different rotation axes at rotation frequencies near the step-out frequency. In simulations, they observed that depending on initial conditions, more than one steady-state rotation axis could be observed at long times in numerical evolution of the magnetoviscous rotational dynamics.

Previous theoretical studies aiming to address wobbling and dynamic (bi)stability of magnetized swimmers have been restricted to simplified geometries or involved simplifying assumptions. For example, Dhar *et al.* [37] studied the behavior of magnetic nano-rods sedimenting on top of a surface. They analytically investigated the configuration of the nano-rod and analyzed the stability of different configurations for different magnetic field strengths and rotation frequencies. However, both Dhar *et al.* [37] and Ghosh *et al.* [2] model the geometry as an ellipsoid or rod for simplicity. In a follow-on theoretical study, Ghosh *et al.* [44] also modeled a helix as a rod to show that there can be more than one steady state solution. Man and Lauga [41] use resistive force theory to obtain the full mobility matrix for a helix, but their analytic results are limited to the asymptotic regime of nearly straight helices. To identify stable orbits, Ghosh *et al.* [2,44] and Man and Lauga [41] both used direct numerical integration of the magnetoviscous dynamics, which identifies stable orbits as the solutions which evolve at long times. Since the evolution depends on initial conditions, it can be difficult to ensure that all possible stable steady solutions have been found numerically.

Our approach uses a boundary element method to find the low-Reynolds-number mobility matrix relating velocities and forces/torques for a rigid object, and then uses a co-rotating body-fixed frame to identify the steady periodically rotating orbits for any frequency and field strength. We also evaluate the stability of each of these orbits. Neither identification of the orbits nor evaluation of their stability requires

numerical integration of the dynamical evolution. We show that swimmers can have more than one stable periodic orbit. We map the magnetoviscous behavior as a function of dimensionless Mason number and as a function of the angle that the magnetic field makes with its rotation axis. We show that for a given magnetic field strength and rotation frequency swimmers can have more than one stable periodic orbit with different rotation axes, and that one can improve the controllability of these types of microswimmers by adjusting the relative angle between the magnetic field and its axis of rotation.

4.3 Models

Although most attempts to develop magnetically rotated microswimmers in bulk fluid have been focused on using chiral geometries such as helices, in a previous study we showed that a much broader class of rigid achiral geometries are capable of propulsion [46]. Here, in order to represent this broad class of geometries, we continue to use the achiral geometry introduced in that previous work, a three-bead geometry with two planes of symmetry as depicted in Fig. 4.1. The basis vectors $\mathbf{e}_2$ and $\mathbf{e}_3$ in Fig. 4.1 are perpendicular to the symmetry planes of the swimmer. We analyze the three-bead swimmer since it is one of the simplest geometries that satisfies the minimum swimming criteria. However, the presented method is applicable to any rigid geometry, such as helices [43].

In experiments, these swimmers have swimming velocities of about $1\mu m/$s, and length of about 10μm, leading to a Reynolds number of the order of 10^{-5}. In low Reynolds number regimes, the linear and angular velocities of moving rigid objects are linearly dependent on the applied torque and force. This can be formulated using

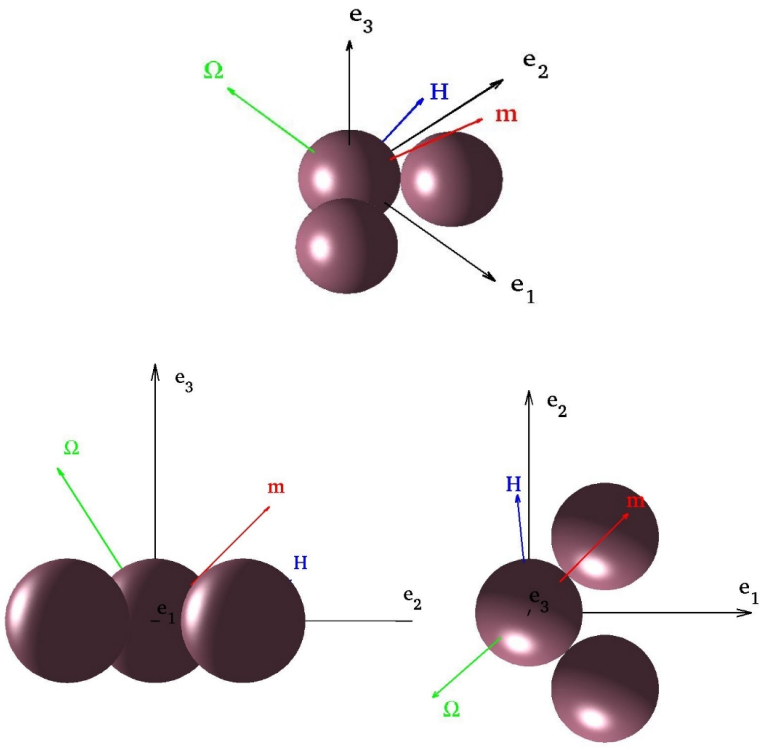

Figure 4.1: Three views of the body-fixed frame for analyzing swimmer dynamics. Top: three-dimensional view; lower left: $\mathbf{e}_1$ pointing out of page; lower right: $\mathbf{e}_3$ pointing out of page. We work in the principal axes of the mobility submatrix $\mathbf{M}$, $\mathbf{e}_1$, $\mathbf{e}_2$, and $\mathbf{e}_3$; $\mathbf{e}_2$ and $\mathbf{e}_3$ are perpendicular to the symmetry planes of the swimmer. The magnetic moment $\mathbf{m}$, angular velocity $\mathbf{\Omega}$, and magnetic field $\mathbf{H}$ are also shown.

a linear operator, the mobility matrix:

$$\begin{pmatrix} \mathbf{v} \\ \mathbf{\Omega} \end{pmatrix} = \begin{pmatrix} \mathbf{K} & \mathbf{C} \\ \mathbf{C}^{\mathsf{T}} & \mathbf{M} \end{pmatrix} \begin{pmatrix} \mathbf{F} \\ \mathbf{N} \end{pmatrix}, \tag{4.1}$$

where the submatrices $\mathbf{K}$, $\mathbf{C}$, and $\mathbf{M}$ that make up the mobility matrix in Eq. 4.1 are each 3×3 matrices, coupling force and translation, torque and translation (or force and rotation), and torque and rotation, respectively.

For the purpose of finding the mobility matrix, we use a boundary element method, the method of regularized Stokeslets [41, 51]. This method allows us to accurately calculate low-Reynolds numbers flow properties of complex geometries. In previous work, we validated and used the method of regularized Stokeslet to find swimming velocities of biological swimmers with asymmetric flagellar configurations [53]. By calculating the force and torque resulting from translations and rotations along the cartesian directions, it is straightforward to obtain the resistance matrix, which is the inverse of the mobility matrix.

In the case of permanently magnetized microswimmers, the external force and torque is caused by the interaction of the magnetic field ($\mathbf{H}$) and magnetic moment dipole of the swimmer ($\mathbf{m}$). We assume that the dipole is permanent and measured by experiment. In the most common case of uniform magnetic field there is no external force on the swimmer. The external torque is

$$\mathbf{N} = (\mathbf{m} \times \mathbf{H}). \tag{4.2}$$

Combining Eqs. 4.1 and 4.2, we arrive at the equation for the angular velocity of the swimmer:

$$\mathbf{\Omega} = \mathbf{M}(\mathbf{m} \times \mathbf{H}). \tag{4.3}$$

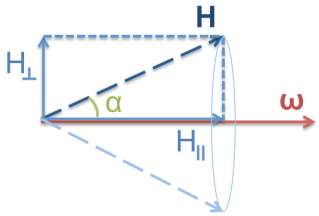

Figure 4.2: Rotation of magnetic field ($\mathbf{H}$) at configuration angle α with rotation vector $\boldsymbol{\omega}$. $\mathbf{H}_{\parallel}$ is the component of $\mathbf{H}$ in the direction of $\boldsymbol{\omega}$. $\mathbf{H}_{\perp}$ is the component of $\mathbf{H}$ perpendicular to $\boldsymbol{\omega}$.

Below we explain how Eq. 4.3 can be solved to find the periodic rotation orbits, evaluate the orbits for stability, and find the corresponding swimming velocities.

4.3.1 General case

The actuating magnetic field can be rotated about an axis making any angle with the field. As illustrated in Fig. 4.2, we call this relative angle the configuration angle α. The magnetic field vector can be decomposed into components parallel and normal to the rotation axis, $\mathbf{H}_{\parallel}$ and $\mathbf{H}_{\perp}$.

One way to solve Eq. 4.3 is to calculate the angular velocity $\boldsymbol{\Omega}$ at the instantaneous configuration of the swimmer and numerically integrate the angular velocity to find the time-dependent orientation, as in previous studies [2,41,44]. In this work, we use a more economical approach which is applicable if one is only interested in steadily rotating solutions. For a steady solution the swimmer follows the rotation of the magnetic field. Therefore, the angular velocity of the swimmer $\boldsymbol{\Omega}$ is equal to the angular velocity of the field $\boldsymbol{\omega}$. Note that this is a similar approach to that employed in [44], but here our definition of a steady solution does not include solutions where the rotation axis is constant but the rotation rate of the field and swimmer are not equal, and hence the rotation rate is time-dependent. Under our definition, in a co-rotating body-fixed frame of the swimmer, the magnetic field and angular

velocities will be constant in time. Using the decomposition of the magnetic field, this is expressed as

$$\mathbf{\Omega} = \omega \hat{\mathbf{H}}_{\parallel} = \mathbf{M}(\mathbf{m} \times \mathbf{H}) \tag{4.4}$$

which should be interpreted in the body-fixed frame of the swimmer. In Eq. 4.4 the strength of the field and its parallel component are specified by the experiment through the configuration angle α. We work in the body-fixed frame corresponding to the principle axes (eigendirections $\mathbf{e}_1$, $\mathbf{e}_2$, and $\mathbf{e}_3$) of sub-matrix $\mathbf{M}$ as shown in Fig. 4.1. Working in the principal axes of sub-matrix $\mathbf{M}$ simplifies the problem by reducing the sub-matrix $\mathbf{M}$ to a diagonalized matrix (with eigenvalues M_{11}, M_{22}, and M_{33}) and therefore reducing the number of parameters. Although the angular velocity of the swimmer ($\boldsymbol{\omega} = \mathbf{\Omega}$) and magnetic field ($\mathbf{H}$) are constant vectors with known magnitude and relative angle α, their precise directions $\hat{\mathbf{\Omega}}$ and $\hat{\mathbf{H}}$ are unknown and need to be solved for.

Taking the dot product of both sides of Eq. 4.4 with $\mathbf{H}$ and dividing by H^2 yields

$$\frac{\omega}{H}\frac{H_{\parallel}}{H} = \hat{\mathbf{H}}^{\mathsf{T}}\mathbf{M}(\mathbf{m} \times \hat{\mathbf{H}}). \tag{4.5}$$

Note that the left-hand-side of Eq. 4.5 will be zero if $H_{\parallel}$ is zero. This corresponds to a special case in which $\mathbf{H}$ and $\boldsymbol{\omega}$ are perpendicular and will be discussed in section 4.3.2. Any steady solution must satisfy the constraint Eq. 4.5, hence Eq. 4.5 specifies a 1-D locus of directions of $\hat{\mathbf{H}}$ on the unit sphere possibly corresponding to steady solutions. We can express the components of $\hat{\mathbf{H}}$ using the two spherical coordinate angles ϕ and θ shown in Fig. 4.3.

$$\hat{\mathbf{H}} = (\sin\theta\cos\phi, \sin\theta\sin\phi, \cos\theta) \tag{4.6}$$

Substituting Eq. 4.6 into Eq. 4.5, we can solve for θ in term of the azimuthal angle ϕ

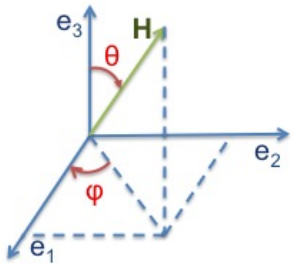

Figure 4.3: Angles ϕ and θ used for expressing the magnetic field direction $\hat{\mathbf{H}}$ in spherical coordinates.

$$\begin{aligned} \theta &= \arctan\left(\frac{-B \pm \sqrt{B^2 + 4(A-C)C}}{2(A-C)}\right), \\ A &= (M_{22} - M_{11}) m_3 \sin\phi\cos\phi, \\ B &= (M_{33} - M_{22}) m_1 \sin\phi + (M_{11} - M_{33}) m_2 \cos\phi, \\ C &= \frac{\omega}{H}\frac{H_\parallel}{H}. \end{aligned} \tag{4.7}$$

To satisfy Eq. 4.4, a field direction specified by θ and ϕ must satisfy Eq. 4.5 and hence Eq. 4.7, but not all directions specified by Eq. 4.7 satisfy Eq. 4.4. To satisfy Eq. 4.4, the directions in Eq. 4.7 must also satisfy the geometric constraint

$$\frac{\mathbf{\Omega}}{\Omega} \cdot \mathbf{H} = H_\parallel, \tag{4.8}$$

which specifies that the component of the magnetic field in the rotation direction has the correct magnitude. Substituting for $\mathbf{\Omega}$ from Eq. 4.4 and dividing both sides by H, this second constraint becomes

$$\frac{\mathbf{M}(\mathbf{m} \times \hat{\mathbf{H}})}{|\mathbf{M}(\mathbf{m} \times \hat{\mathbf{H}})|} \cdot \hat{\mathbf{H}} = \frac{H_\parallel}{H} = \cos\alpha. \tag{4.9}$$

To find all magnetic field directions satisfying Eq. 4.4 specified by the angles θ and

ϕ, we check all the directions specified by Eq. 4.7 to see if they also satisfy Eq. 4.9. Substitution of an $\hat{\mathbf{H}}(\theta, \phi)$ satisfying both equations into Eq. 4.4 yields the direction and magnitude of the corresponding rotation axis in the swimmer's frame.

4.3.2 Perpendicular case

A special case arises when the magnetic field is perpendicular to its rotation. Then $\mathbf{H} = \mathbf{H}_{\perp}$, and since the swimmer's angular velocity is equal to the angular velocity of the field

$$\mathbf{\Omega} = \boldsymbol{\omega} = \mathbf{M}(\mathbf{m} \times \mathbf{H}). \tag{4.10}$$

As before, it is convenient to work in a body-fixed frame of the swimmer such as that specified by the principal axes of the sub-matrix $\mathbf{M}$ (Fig. 4.1). In Eq. 4.10, the field strength and the rotation frequency of the field are known from the experiment. Since the field is perpendicular to its rotation vector, if we take the dot product of $\hat{\mathbf{H}}$ with both sides of Eq. 4.10,

$$0 = \hat{\mathbf{H}}^{\mathsf{T}}\mathbf{M}(\mathbf{m} \times \hat{\mathbf{H}}). \tag{4.11}$$

This imposes a constraint which results in a 1-D locus of allowable directions of $\hat{\mathbf{H}}$. Substituting Eq. 4.6 into Eq. 4.11, $\hat{\mathbf{H}}$ and solving for θ (or substituting $C = 0$ in Eq. 4.5) yields:

$$\theta = -\arctan\left(\frac{(M_{33}-M_{22})m_1 \sin\phi + (M_{11}-M_{33})m_2 \cos\phi}{(M_{22}-M_{11})m_3 \sin\phi \cos\phi}\right). \tag{4.12}$$

Equation 4.12 specifices a set of magnetic field directions $\hat{\mathbf{H}}$ via the spherical coordinate angles (θ, ϕ). In the perpendicular case, each direction specified by Eq. 4.12 also satisfies Eq. 4.4, since Eq. 4.9 becomes equivalent to Eq. 4.11. However, each direction corresponds to a different value of the rotation frequency ω, which can be determined by substituting an $\mathbf{H}(\theta, \phi)$ specified by Eq. 4.12 into Eq. 4.4.

In addition to the solutions satisfying Eq. 4.12, there are also two solutions at the magnetic field directions specified by $\theta = 0$ and $\theta = \pi$ (along the $\hat{\mathbf{e}}_3$ axis). Substitution into Eq. 4.10 implies that these are isolated solutions, each at a single frequency. Since it would be nearly impossible to tune the frequency to this single value (a set of measure zero in frequency space) for a given experimental realization, we ignore these solutions in the rest of the manuscript.

4.3.3 Swimming speeds

Once the steady state direction of rotation and field are found, one can find the swimming velocity of the swimmer. The instantaneous velocity of the swimmer based on Eq. 4.1 is

$$\mathbf{v} = \mathbf{CN} = \mathbf{C}(\mathbf{m} \times \mathbf{H}). \tag{4.13}$$

If this velocity is not along the direction of rotation $\mathbf{\Omega}$, the swimmer makes a helical trajectory along the axis of rotation and the time-averaged swimming velocity is the component of the instantaneous velocity along the axis of rotation [53] (Fig. 4.4):

$$\mathbf{V}_s = \mathbf{v} \cdot \mathbf{\Omega}. \tag{4.14}$$

Note that although the mobility matrices and instantaneous velocity depend on the choice of origin of the body frame for the rigid swimmer, the average velocity in Eq. 4.14 does not. As shown in Fig. 4.4, in one rotation period, the swimmer moves by one pitch of the helical trajectory and returns to the same orientation. Since after one rotation the net motion is simple translation, while different origins or points of the swimmer body have helical trajectories with different radii, all the helical trajectories have the same pitch. The average velocity in Eq. 4.14 is equivalent to the pitch divided by the rotation period, so is independent of the choice of origin.

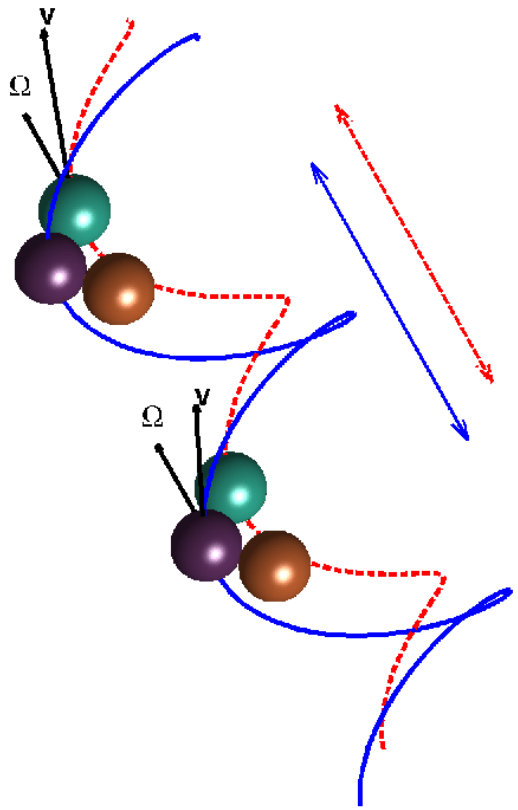

Figure 4.4: Helical trajectory taken by swimmer. The two curves (solid blue and dashed red) are the trajectories of the centroids of the middle and upper beads, which represent two possible choices of origins for the body-fixed frame. In the body frame the rotation around the origin ($\mathbf{\Omega}$) and instantaneous velocity ($\mathbf{v}$) are constant. The instantaneous velocity depends on the choice of origin, but the rotation does not. The swimmer is depicted at two times separated by the rotation period $2\pi/\Omega$, during which it translates by one helical pitch (shown by dimension arrows at left) and rotates back to the same orientation. The average swimming velocity is the pitch divided by the rotation period and is the same for either choice of origin.

One can also show that V_s is independent of the choice of origin even though the mobility matrices depend on the choice of origin by considering how the mobility matrices transform under a shift of origin by a displacement $\mathbf{r}$. Let the position, instantaneous velocity of the original origin and angular velocity, total force, and total torque referenced to the original origin be $\mathbf{x}$, $\mathbf{v}$, $\boldsymbol{\Omega}$, $\mathbf{F}$, and $\mathbf{N}$, respectively, while the position, instantaneous velocity of the shifted origin and angular velocity, total force, and total torque referenced to the shited origin be $\mathbf{x}'$, $\mathbf{v}'$, $\boldsymbol{\Omega}'$, $\mathbf{F}'$, and $\mathbf{N}'$.

The original and primed quantities are related by

$$\mathbf{x}' = \mathbf{x} - \mathbf{r} \tag{4.15}$$

$$\boldsymbol{\Omega}' = \boldsymbol{\Omega} \tag{4.16}$$

$$\mathbf{v}' = \mathbf{v} + \boldsymbol{\Omega} \times \mathbf{r} \tag{4.17}$$

$$\mathbf{F}' = \mathbf{F} \tag{4.18}$$

$$\mathbf{N}' = \mathbf{N} - \mathbf{r} \times \mathbf{F}. \tag{4.19}$$

From these, one can explicitly show how the mobility matrices depend on the origin, and the resulting invariance of V_s', by writing

$$\begin{pmatrix} \mathbf{v}' \\ \boldsymbol{\Omega}' \end{pmatrix} = \begin{pmatrix} \mathbf{v} + \boldsymbol{\Omega} \times \mathbf{r} \\ \boldsymbol{\Omega} \end{pmatrix} \tag{4.20}$$

$$= \begin{pmatrix} (\mathbf{KF} + \mathbf{CN}) + (\mathbf{C}^{\mathsf{T}}\mathbf{F} + \mathbf{MN}) \times \mathbf{r} \\ \mathbf{C}^{\mathsf{T}}\mathbf{F} + \mathbf{MN} \end{pmatrix}. \tag{4.21}$$

Finally, by rewriting $\mathbf{F}$ and $\mathbf{N}$ in terms of $\mathbf{F}'$ and $\mathbf{N}'$, one can identify the submatrices

in

$$\begin{pmatrix} \mathbf{v}' \\ \mathbf{\Omega}' \end{pmatrix} = \begin{pmatrix} \mathbf{K}' & \mathbf{C}' \\ (\mathbf{C}')^{\mathsf{T}} & \mathbf{M}' \end{pmatrix} \begin{pmatrix} \mathbf{F}' \\ \mathbf{N}' \end{pmatrix}, \tag{4.22}$$

as

$$\mathbf{K}' = \mathbf{K} + \mathbf{C} \times \mathbf{r} - \mathbf{r} \times \mathbf{C}^{\mathsf{T}} - \mathbf{r} \times \mathbf{M} \times \mathbf{r} \tag{4.23}$$

$$\mathbf{C}' = \mathbf{C} - \mathbf{r} \times \mathbf{M} \tag{4.24}$$

$$\mathbf{M}' = \mathbf{M}, \tag{4.25}$$

where $(\mathbf{r} \times \mathbf{M})_{ad} = \epsilon_{abc} r_b M_{cd}$ and $(\mathbf{M} \times \mathbf{r})_{ad} = M_{ab} \epsilon_{bcd} r_c$, etc. These transformations of the mobility matrix are analogous to those provided by Happel and Brenner [73] for transformations of the resistance matrix. Using these,

$$V_s' = \mathbf{v}' \cdot \mathbf{\Omega}' / |\mathbf{\Omega}'| \tag{4.26}$$

$$= [(\mathbf{C} - \mathbf{r} \times \mathbf{M})\mathbf{N}] \cdot [\mathbf{MN}] / |\mathbf{MN}| \tag{4.27}$$

$$= [\mathbf{CN}] \cdot [\mathbf{MN}] / |\mathbf{MN}| \tag{4.28}$$

$$= \mathbf{v} \cdot \mathbf{\Omega} / |\mathbf{\Omega}| \tag{4.29}$$

$$= V_s. \tag{4.30}$$

Therefore, V_s is independent of the choice of origin even though the mobility matrices depend on the origin.

4.3.4 Stability

We examine the steady solutions found in the previous sections for dynamic stability. Consider a steady state solution that rotates with rate $\mathbf{\Omega}$ in the lab frame. At time $t = 0$, perturb the solution by rotating the swimmer by an infinitesimal rotation

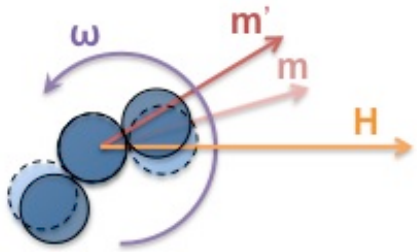

Figure 4.5: Schematic of the geometry of the swimmer corresponding to the stable solution (transparent geometry) and perturbed solutions (opaque geometry). Note that the magnetic field and its angular velocity stay unchanged in the lab frame after perturbation.

vector $\boldsymbol{\sigma}(t=0)$ (Fig. 4.5) and allow it to rotate due to the magnetic torque. Let $\mathbf{R}(t)$ be the rotation matrix which rotates the steady state solution at time t to the orientation of the perturbed swimmer at time t, and $\boldsymbol{\sigma}(t)$ be the rotation vector corresponding to $\mathbf{R}(t)$. Then at time $t=0$, since $\boldsymbol{\sigma}$ is infinitesimal,

$$R_{ij}(t=0) = (\delta_{ij} + \epsilon_{ikj}\sigma_k(t=0)). \tag{4.31}$$

At time $t=0$, the perturbed swimmer rotates with angular velocity $\boldsymbol{\Omega}'$, which can be obtained from Eq. 4.4 by rotating the swimmer properties such as the sub-matrix $\mathbf{M}$ and the magnetic dipole moment $\mathbf{m}$ to the perturbed orientation (denoted by a prime) in the lab frame:

$$\begin{aligned} \boldsymbol{\Omega}' &= \mathbf{M}'(\mathbf{m}' \times \mathbf{H}), \\ \mathbf{M}' &= \mathbf{R}\mathbf{M}\mathbf{R}^{\mathsf{T}}, \\ \mathbf{m}' &= \mathbf{R}\mathbf{m}. \end{aligned} \tag{4.32}$$

At time $\mathrm{d}t$, the steady state solution will have rotated by $\boldsymbol{\Omega}\mathrm{d}t$, while the perturbed swimmer will have rotated by $\boldsymbol{\Omega}'\mathrm{d}t$. Thus at $t=0$, $\mathbf{R}(t)$ evolves by the rotation

$(\boldsymbol{\Omega}' - \boldsymbol{\Omega})\mathrm{d}t$:

$$\frac{\mathrm{d}R_{ij}}{\mathrm{d}t} = \lim_{\mathrm{d}t\to 0} \frac{(\delta_{il} + \epsilon_{ikl}(\Omega'_k - \Omega_k)\mathrm{d}t)R_{lj} - R_{ij}}{\mathrm{d}t}. \tag{4.33}$$

The linearized rated of change of $\mathbf{R}$ with time can alternatively be found in terms of $\boldsymbol{\sigma}$ by differentiating Eq. 4.31,

$$\frac{\mathrm{d}R_{ij}}{\mathrm{d}t} = \epsilon_{ikj}\frac{\mathrm{d}\sigma_k}{\mathrm{d}t}. \tag{4.34}$$

By equating Eqs. 4.33 and 4.34, we can obtain the rate of change of $\boldsymbol{\sigma}$ with time.

$$\begin{aligned} \frac{\mathrm{d}\sigma_i}{\mathrm{d}t} &= \left(M_{ij}\epsilon_{jkl}m_k\epsilon_{lmn}H_m - \epsilon_{ijn}M_{jl}\epsilon_{lmo}m_m H_o\right)\sigma_n \\ &\equiv Q_{in}\sigma_n, \end{aligned} \tag{4.35}$$

where the last equality defines $\mathbf{Q}$. The corresponding solution is stable if all the real parts of eigenvalues of $\mathbf{Q}$ are negative. Application of this criteron allows determination of stability without needing numerical integration to observe the long-time dynamics of the governing equation.

4.4 Results

In order to demonstrate the features of solutions to both the general and perpendicular paramagnetic case, we perform calculations for a specific three-bead swimmer with beads of diameter 4.35μm attached in a bent configuration, forming a 90° angle. This geometry is similar to structures fabricated using carboxyl beads and demonstrated to swim by magnetic rotation [46]. We chose an arbitrary direction for the magnetic moment dipole pointing in the $(1, 1, 1)$ direction in the frame of the principle axis of the swimmers sub-matrix $\mathbf{M}$.

To apply the method of regularized stokeslets, we discretized the surface of the

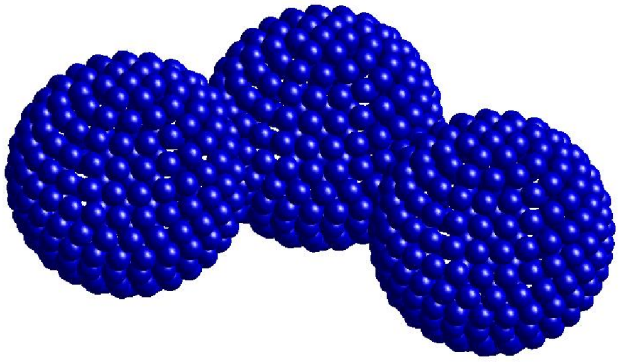

Figure 4.6: Discretized surface of a three-bead swimmer. Each of the 717 spheres on the surface represents one regularized stokeslet.

swimmer with 717 elements as shown in Fig. 4.6. In Fig. 4.6, each ball represents the position of a regularized stokeslet. We calculated the sub-matrices of mobility matrix to be

$$\mathbf{K} = \begin{pmatrix} 1.38 & 0 & 0 \\ 0 & 1.73 & 0 \\ 0 & 0 & 1.72 \end{pmatrix} \times 10^{7}\,\mathrm{m\,N^{-1}\,s^{-1}} \tag{4.36}$$

$$\mathbf{C} = \begin{pmatrix} 0 & 0 & 0 \\ 0 & 0 & -1.16 \\ 0 & 1.94 & 0 \end{pmatrix} \times 10^{12}\,\mathrm{N^{-1}\,s^{-1}} \tag{4.37}$$

$$\mathbf{M} = \begin{pmatrix} 1.58 & 0 & 0 \\ 0 & 8.96 & 0 \\ 0 & 0 & 5.11 \end{pmatrix} \times 10^{17}\,\mathrm{rad\,N^{-1}\,s^{-1}m^{-1}} \tag{4.38}$$

We can investigate the effect of each of the physical parameters by nondimensionalizing Eq. 4.4 using the viscosity μ, magnetic dipole strength m, field strength H, and L_c, a characteristic length of the swimmer, which we choose to be the distance

between the centroids of its non-central spheres. The dimensions of $\mathbf{M}$ are $[\mu]^{-1}[L_c]^{-3}$, so in nondimensional form Eq. 4.4 becomes

$$\mathrm{Ma}\,\hat{\mathbf{H}}_{\|} = \tilde{\mathbf{M}}(\tilde{\mathbf{m}} \times \tilde{\mathbf{H}}), \tag{4.39}$$

where $\mathrm{Ma} = \mu L_c^3 \omega/(mH)$ is the Mason number and tildes indicate nondimensional quantities. Physically, the Mason number is the ratio between viscous rotational torque and the maximum torque exerted by the magnetic field. Thus, the solutions depend on all the experimental parameters through only two dimensionless quantities, Ma and α [the configuration angle between the field direction and rotation direction (Fig. 4.2)]. In the following we explore the results across a range of different configuration angles (α) and Mason numbers.

4.4.1 Swimmer orientations in steady periodic rotational orbits

A steady periodic rotational orbit corresponds to specific (constant) directions of magnetic field and rotation axis in the swimmer frame. Figures 4.7, 4.8, and 4.9 depict directions of the magnetic field and directions of rotation in the body-fixed frame of the swimmer that lead to steady rotational orbits for $\alpha = 80°$, $90°$, and $100°$, respectively. In the center of each plot we show the swimmer in its body fixed frame composed of the eigenvectors of the sub-matrix $\mathbf{M}$ ($\mathbf{e}_1$,$\mathbf{e}_2$, and $\mathbf{e}_3$) and the direction of the magnetic dipole moment. The colored points on the unit sphere of panel (a) in each figure demonstrate the allowed directions of the field. The color of these points corresponds to the values of the azimuthal angle ϕ, varying from 0 to 2π as shown in the color bar. The purple surface shows directions of the magnetic field which are stable according to Eq. 4.35. Therefore, the stable solutions correspond to the portion

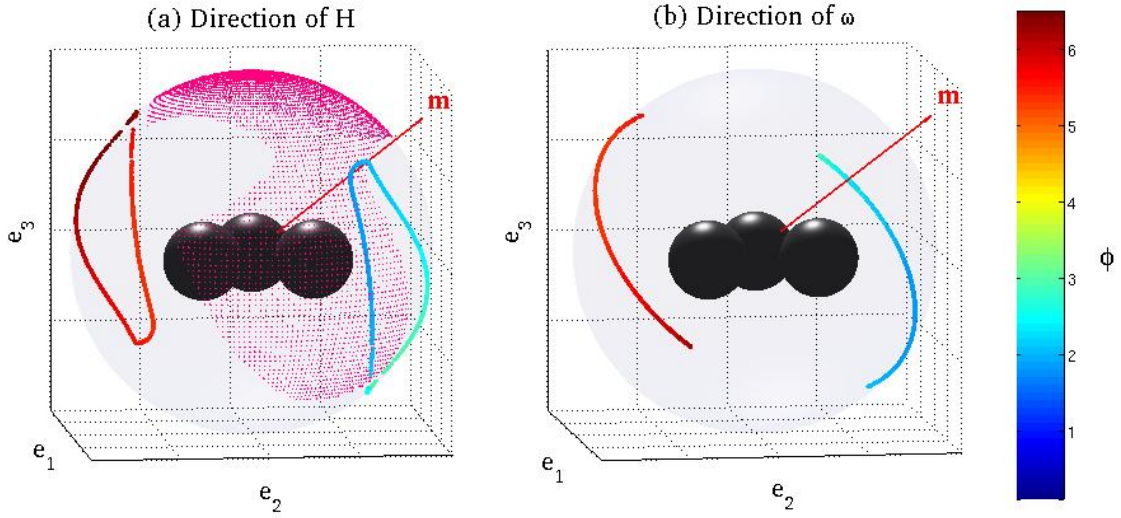

Figure 4.7: 1-D locus of allowable directions of the a) magnetic field and b) rotation axis in the body-fixed frame for $\alpha = 80°$. The purple area on the surface of the sphere in panel (a) shows direction of **H** which are stable according to Eq. 4.35.

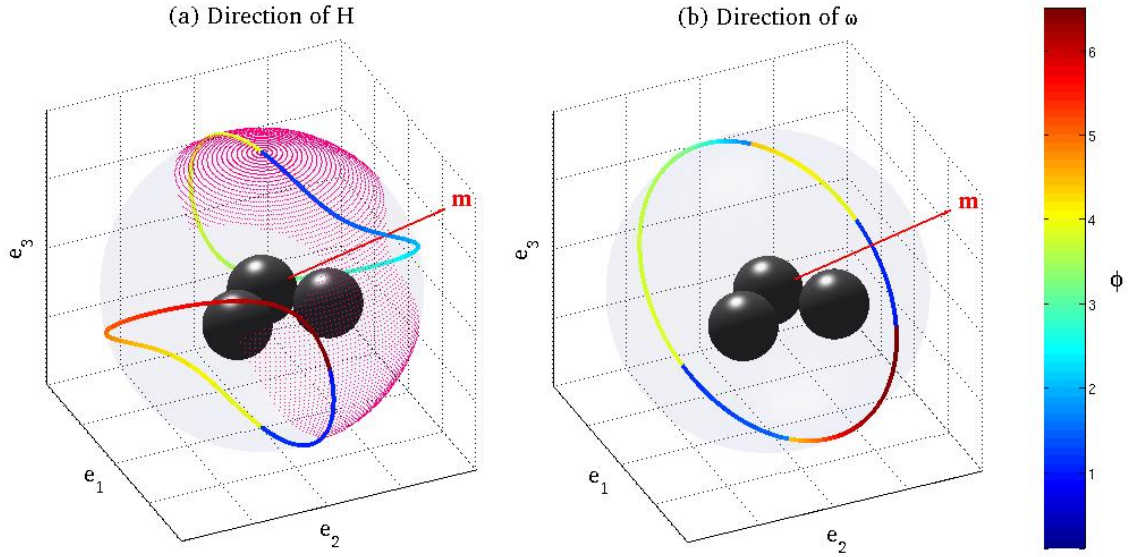

Figure 4.8: 1-D locus of allowable directions of the a) magnetic field and b) rotation axis in the body-fixed frame for $\alpha = 90°$. The purple area on the surface of the sphere in panel (a) shows direction of **H** which are stable according to Eq. 4.35.

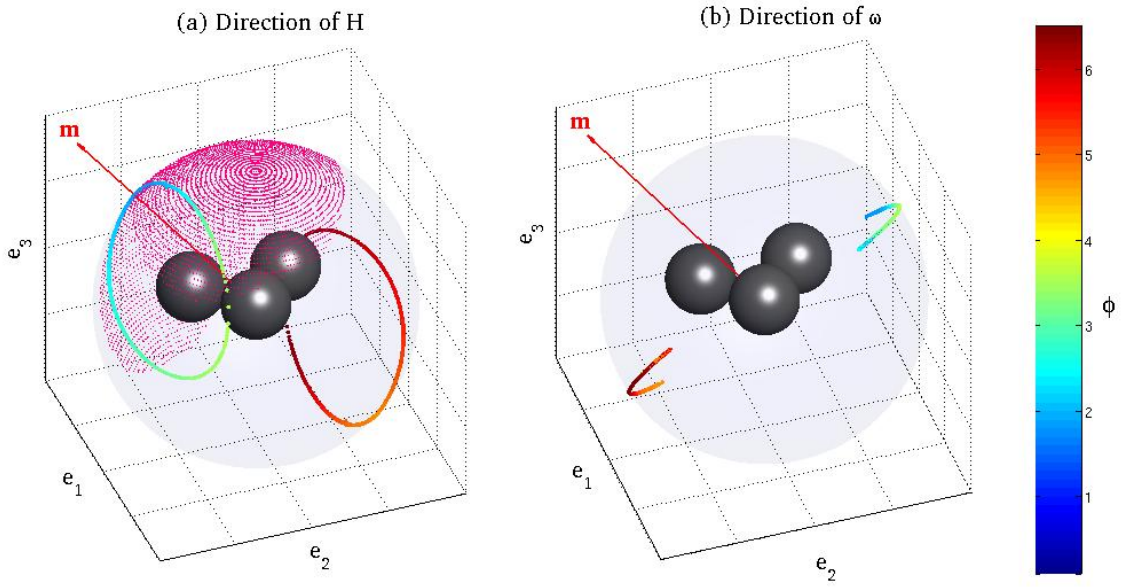

Figure 4.9: 1-D locus of allowable directions of the a) magnetic field and b) rotation axis in the body-fixed frame for $\alpha = 100°$. The purple area on the surface of the sphere in panel (b) shows direction of $\mathbf{H}$ which are stable according to Eq. 4.35.

of the curve that passes through the purple area. The colored points in panel (b) of Figs. 4.7-4.9 show the directions of the steady rotations in the swimmer's frame. In these panels, the color of the point is the same as the color of the corresponding field direction in panel (a).

Each pair of $\hat{\mathbf{H}}$ and $\hat{\boldsymbol{\omega}}$ on the curves corresponds to an experimental realization which can be specified by the strength of the magnetic field H, magnitude of the angular velocity ω, and magnitude of the magnetic dipole moment m through the Mason number. Thus, tracing along the curves yields a Mason number for each point. For example, in Fig. 4.8, the Mason number for each point can be expressed as $\mathrm{Ma}(\phi)$, which is plotted in Fig. 4.10. In this graph, the color of each point is the same as the corresponding point in Fig. 4.8a. Then, for a given Ma, the experimentally realized directions of the magnetic field and rotation can be obtained by finding the value of ϕ for which $\mathrm{Ma}(\phi)$ is equal to the Mason number, shown graphically in Fig. 4.10. In this

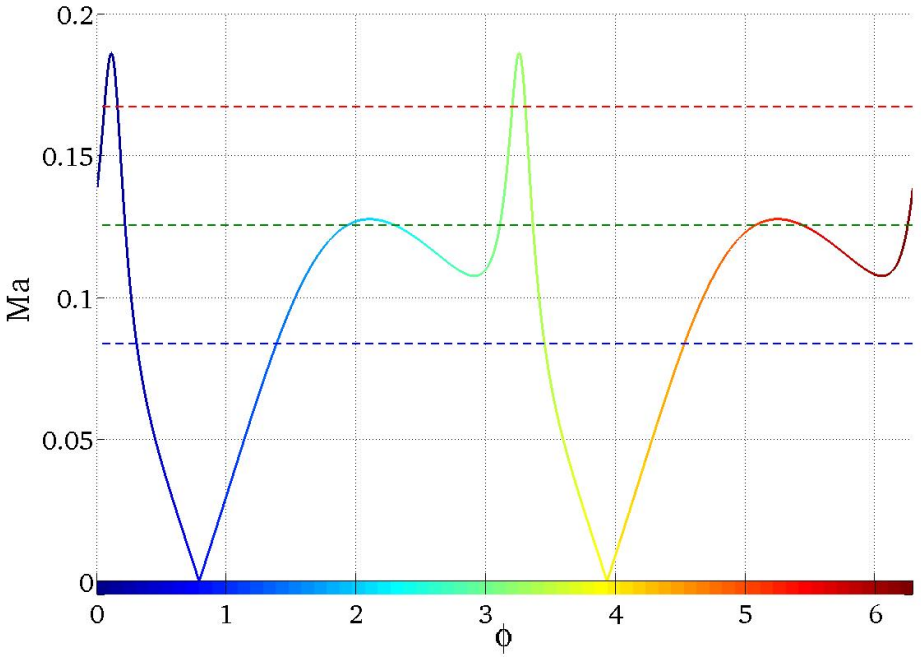

Figure 4.10: Mason number as a function of the azimuthal angle ϕ for $\alpha = 90°$. Color spectrum represents the values of the azimuthal angle ϕ and is identical to the color coding used in Fig. 4.8. Intersections with the horizontal lines, at different Mason numbers, specify solutions for different experimental realizations. Here, the horizontal lines at Mason numbers of 0.08, 0.12, and 0.17 correspond to frequencies of 10, 15, and 20 Hz at $m = \sqrt{3} \times 10^{-14}$J/T, and $H = 10.11$mT.

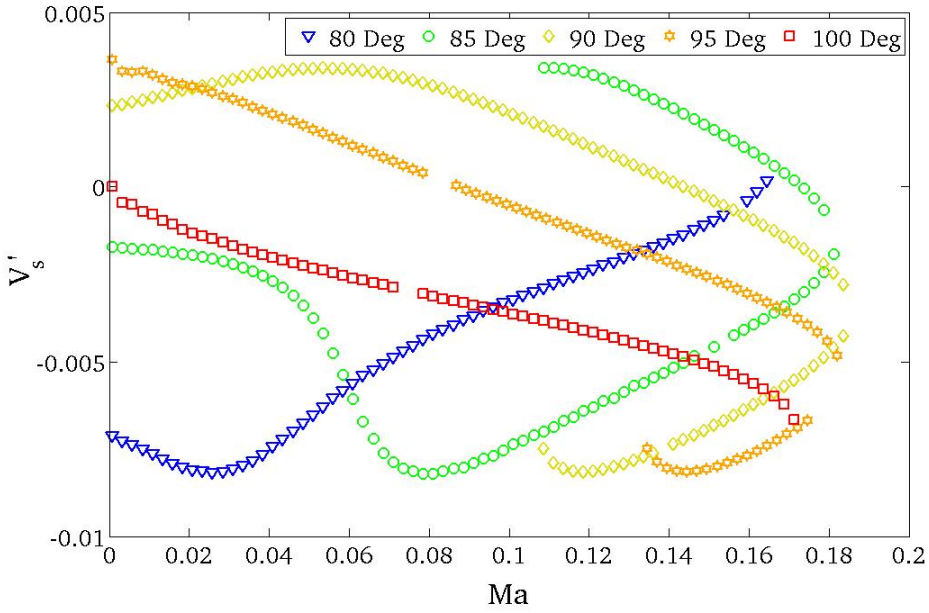

Figure 4.11: Dimensionless swimming velocity vs Mason number for different values of α.

plot, solutions correspond to the intersection of the curve representing Ma(ϕ) and the horizontal lines belonging to the specific experimental conditions. Once the angle ϕ is found, we can go back to Fig. 4.8 to obtain the corresponding angle θ which specifies the direction of $\mathbf{H}$, and from which the rotation axis $\mathbf{\Omega}$ can be calculated through Eq. 4.3. As illustrated by Fig. 4.10, there might be multiple possible solutions for each frequency. Some of these solutions may be unstable if they are not in the purple region in Fig. 4.8.

For the cases of non-perpendicular configurations of the magnetic field (Figures 4.7 and 4.9), the existence of a solution is not guaranteed for all the values of ϕ, but different points on the curves in Figs. 4.7 and 4.9 still correspond to different Ma.

4.4.2 Swimming speeds

The swimming speed can be nondimensionalized using units of $L_c\omega$,

$$V_s' = \frac{V_s}{L_c\omega} \tag{4.40}$$

The nondimensional swimming speed V_s' is a function of Ma and α. Figure 4.11 shows the non-monotonic behavior of the non-dimensional swimming velocity for our example swimmer as a function of Mason number for a variety of fixed values of α. For each value of α, the velocity as a function of Mason number is continuous; the obvious gaps in the curves of Fig. 4.11 are a result of errors due to numerical precision in the root-finding algorithms used to solve Eqs. 4.7, 4.9, and 4.10. For each angle α, steady solutions are available only up to a certain frequency, the well-known step-out frequency [36]. Above the step-out frequency the swimmer cannot follow the magnetic field fast enough to maintain a steady rotation. As we discuss below in Section 4.4.4, for our geometry, the shape of the velocity-frequency curve for our geometry is quite different from that for helices.

For certain angles of the magnetic field relative to its axis of rotation there is a range of bistability (for $\alpha = 85°$, $0.104 < \text{Ma} < 0.180$; for $\alpha = 90°$, $0.108 < \text{Ma} < 0.185$, and for $\alpha = 95°$, $0.134 < \text{Ma} < 0.175$), where there are 2 stable solution with different values of V_s'. Note that in these bistabilities the two solutions can even have opposite directions of swimming at the same rotation rates.

To further investigate the swimming velocities, we studied the dependence of dimensionless swimming velocities on the configuration angle α for a number of different constant Mason numbers. Figure 4.12 plots dimensionless swimming velocity versus magnetic field configuration angles (α) for Ma = 0.058. This plot can be broken down to three regions. In region I, at the smallest and largest configuration angles,

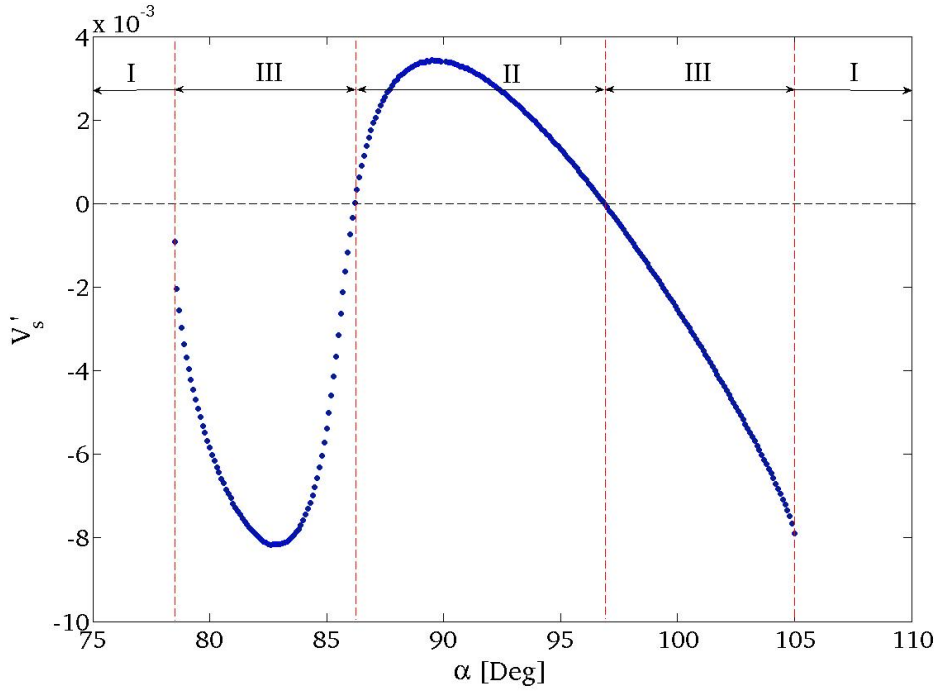

Figure 4.12: Dimensionless swimming velocity versus magnetic field's configuration angle (α) at Ma = 0.058. In region I, no swimming motion is expected; region II and III have one positive and negative solutions respectively, corresponding to swimming in the same and opposite direction of the rotation vector.

no steady solutions are available. In region II, the swimming velocity is positive, *i.e.*, in the same direction as the rotation vector. In region III, the swimming velocity is negative, in the opposite direction as the rotation vector.

Figures 4.13 and 4.14 illustrate the same velocity-angle dependence for Mason numbers of 0.125 and 0.167 respectively. In these plots, regions I, II, and III correspond to no solution, single positive solution, and single negative solution as before, but there are two more regions marked as IV and V. In region IV there are two stable solutions with swimming velocities of opposite directions. In region V, there are two stable solutions but with swimming velocities in the same direction. As in Fig. 4.11, the curves as a function of α are continuous, and gaps arise from errors due to numerical precision in root finding algorithms, except for at $\alpha = 90°$, where gaps result

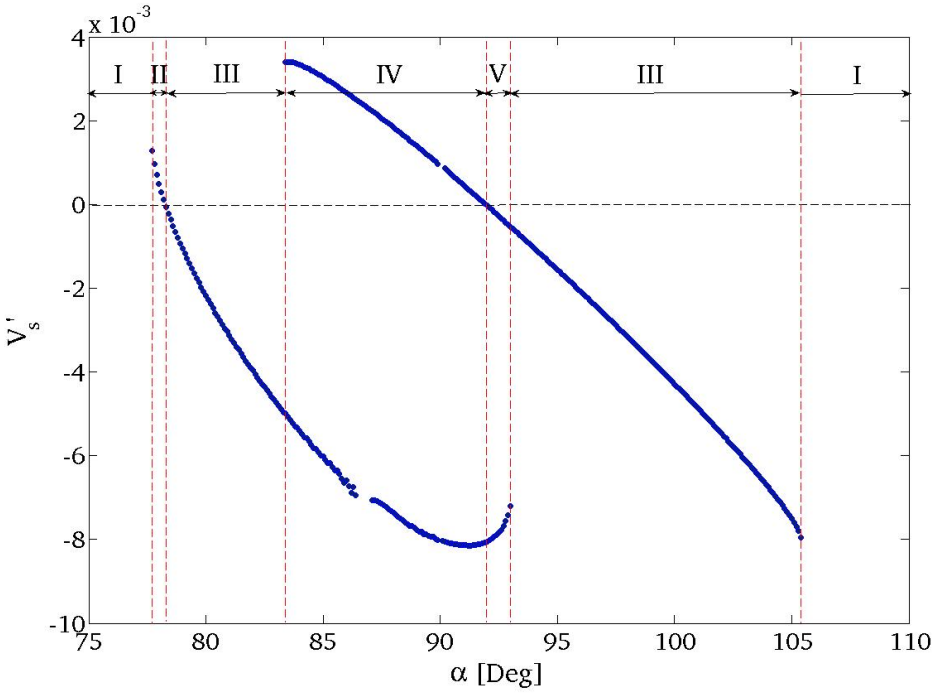

Figure 4.13: Dimensionless swimming velocity versus magnetic field's configuration angle (α) at Ma = 0.125. Regions I to III are defined as in Fig. 4.12. In region IV there are two possible swimming velocities with opposite directions. In region V, there are two possible swimming velocities, but in the same direction.

from the need to consider the perpendicular case separately.

4.4.3 Implications for control

Identifying regions with bistability and monostability may be important for the control of the swimmers, since α, H, ω, and $\hat{\boldsymbol{\omega}}$ are the quantities amenable to experimental control. The rotation axis $\hat{\boldsymbol{\omega}} = \hat{\boldsymbol{\Omega}}$ determines the direction of the swimming movement. The magnitudes ω and H both enter through the Mason number, which has been used in the past as the main control parameter, for instance by varying frequency to alter the speed of swimmers. Identification of the regions in Figures 4.12 to 4.14 allows control of the swimming velocity of the swimmer by adjusting the field configuration angle α. The swimming speed does vary with α, so the configuration

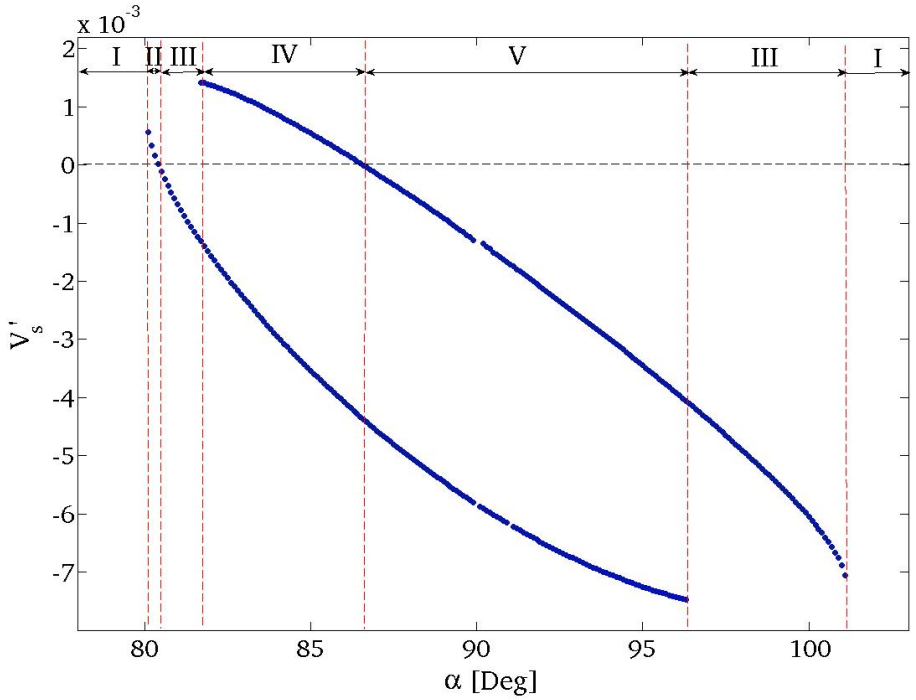

Figure 4.14: Dimensionless swimming velocity versus magnetic field's configuration angle (α) at Ma = 0.167. Regions are defined in the same fashion as in Figures 4.12 and 4.13.

angle could be used to control speed like Ma, but α can also be used to control the qualitative features of the solutions as described below.

First, beyond the step-out frequency unsteady rotation occurs. However, this unsteady wiggling motion can be avoided, by adjusting angle α such that the step-out frequency is as high as possible.

Second, even if there are only monostable regimes such as in Fig. 4.12, changing α can control the direction of swimming by choosing between region II and region III, for a fixed frequency.

Third, experiments have observed bistability in certain frequency regimes for helical swimmers [2]. Bistability also hinders control, for example, in regions IV and V. In region IV the solutions have swimming velocities of opposite direction. In this case, the direction in which the swimmer moves may depend on the initial conditions, which cannot be predicted based on these graphs. In region V, bistable solutions result in swimming velocities of the same direction, but the swimming speed can take different values and therefore, cause uncertainty in control capacity. We can avoid bistability by adjusting α to stay away from regions IV and V. At any Mason number, we can also choose the swimming direction to be in the same direction as the rotation by choosing region II, or we can choose it to be in the opposite direction of the rotation by working in region III. Thus, the angle α may serve as a useful parameter to enhance control of these type of microswimmers.

While preparing this manuscript we learned that a control scheme involving the introduction of nonzero $B_{\|}$ and hence $\alpha \neq 90^{\circ}$ has recently been employed by Cheang *et al.* [74]. Our work provides a physics-based model to predict the behavior of swimmers in such a scheme, as well as develop more sophisticated control strategies which vary the configuration angle α.

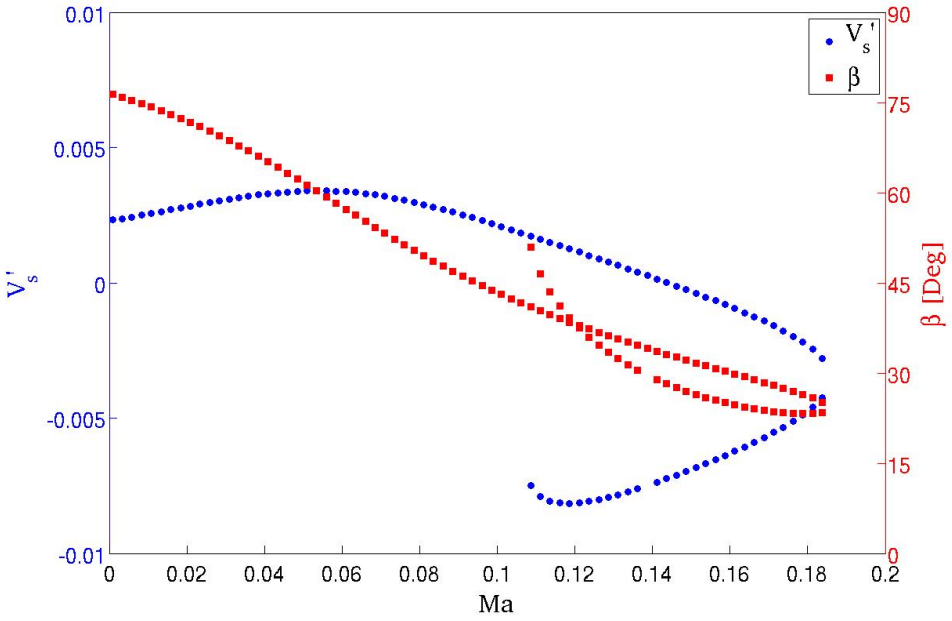

Figure 4.15: Dimensionless swimming V_s' (blue squares) and precession angle β (red circles) vs Mason number at $\alpha = 90°$.

4.4.4 Rotation axes and precession

Finally, we wish to discuss the steady solutions we have found in the context of the wobbling/tumbling, precession, and propulsional behavior discussed in the literature for helical swimmers [2, 3, 38, 41]. For our swimmer, the rotation axis depends on the Mason number, which is similar to previous experimental observations and theoretical results for helices. For helices, the rotation has been characterized by a precessional angle β between the helical axis and the rotation axis [41]. To compare to our swimmer, which is not a helix, we introduce the precession angle β between the long axis of the swimmer ($\mathbf{e}_2$, which has the largest eigenvalue of $\mathbf{M}$) and the direction of rotation ($\hat{\mathbf{\Omega}}$). $\beta = 0$ corresponds to rotation about the long axis, while $\beta = 90°$ corresponds to what has been called tumbling and $\beta \neq 0$ corresponds to wobbling.

Figure 4.15 shows how the precession angle depends on Mason number for the perpendicular case ($\alpha = 90°$). As observed above, the bistability results in two

possible precession angles for certain values of Mason number.

Like the helices, near zero Mason number (small frequencies) the precession angle is closer to 90°, and then decreases as the frequency increases. However, unlike the results for helices, the precession angle does not scale with the inverse of the Mason number, the precession angle does not approach 0° as the frequency increases, nor is there an abrupt transition from tumbling ($\beta \approx 90°$) to precessional motion with $\beta \neq 0°$ [2, 41].

Furthermore, a helix shows a continual, almost linear increase in swimming velocity as the frequency increases towards step-out, and then a sharp drop as step-out is exceeded. In terms of the dimensionless velocity V_s', which is scaled by $L_c\omega$, this would correspond to a nearly flat V_s' as a function of Ma below step-out (where steady solutions exist). In contrast, our swimmers show a gentle rise in swimming velocity which peaks at a frequency below step-out, and then the velocity decreases until step-out.

The differences in precession angle and velocity as a function of Mason number between our results and helices are not unexpected since our geometry is quite different from a helix.

4.5 Conclusion

We described a method to investigate dynamical stability that can be generally applied to any rigid geometry and does not require any geometric simplifications. We found that certain experimental settings result in bistability. We show that one can effectively avoid bistable regions by adjusting the relative angle between magnetic field and its axis of rotation. This provides a physics-based model for control which allows us to predict the swimming speed and direction deterministically. Our model is also capable of illuminating the wobbling motion as reported in the literature for

helices. While here we studied the wobbling of a three-bead geometry we also can apply our method to helices to further elucidate their rotational behavior while accurately taking into account the helical geometry [43]. Furthermore, our analysis can be extended to arbitrary swimmer geometries in unsteady regimes (such as the regime beyond the step-out frequency) through numerical integration of the rotational dynamics using accurately calculated mobility matrices. Although our $\approx 10\,\mu$m swimmers are negligibly affected by Brownian fluctuations, numerical integration of the rotational dynamics including Langevin noise can also extend our analysis to smaller swimmers where thermal fluctuations are more important [75]. Paramagnetic and soft-ferromagnetic magnetic response can be incorporated through the appropriate relationship between moment and magnetic field. Finally, our work may serve as a precursor to investigations of the behavior of groups or swarms of interacting magnetic microswimmers, since understanding the individual dynamics of magnetic swimmers provides the first step before interactions between swimmers can be considered.

4.6 Acknowledgments

This work was funded by National Science Foundation awards (CBET-1067798, DMR-1307497, and CMMI-1435652) to H. Fu.

Chapter 5

Magnetization Directions and Geometries of Helical Microswimmers for Linear Velocity-Frequency Response

5.1 Abstract

Recently, there has been much progress in creating microswimmers or microrobots capable of controlled propulsion in fluidic environments. These microswimmers have numerous possible applications in biomedicine, microfabrication, and sensing. One type of effective microrobot consists of rigid magnetic helical microswimmers that are propelled when rotated at a range of frequencies by an external rotating magnetic field. Here, we focus on investigating what magnetic dipoles and helical geometries optimally lead to linear velocity-frequency response, which may be desirable for the precise control and positioning of microswimmers. We identify a class of optimal magnetic field moments. We connect our results to the wobbling behavior previously

observed and studied in helical microswimmers. In contrast to previous studies, we find that when the full helical geometry is taken into account, wobbling-free motion is not possible for magnetic fields rotating in a plane. Our results compare well quantitatively to previously reported experiments, validating the theoretical analysis method. Finally, in the context of our optimal moments, we identify helical geometries for minimization of wobbling and maximization of swimming velocities.

5.2 Introduction

Micro- and nano-robots capable of controlled propulsion have been pursued for a variety of microfabrication and biomedical applications. Biomedical applications include drug delivery [7, 8], tissue manipulation [5, 6, 10], and *in vivo* diagnostics and sensing [9, 11–13]. A number of types of microrobots employing different propulsion techniques have been developed, including chemically-powered microrobots dependent on external fuels to create phoretic flows [16–24], externally controlled biotic systems [14], dielectrophoretically manipulated robots [76], and magnetically actuated robots, including those that require a nearby surface [34, 35, 56, 57], and those that can swim in bulk fluids [15, 45, 46, 59–61, 63–67]. In this paper, we focus on magnetically actuated microswimmers in bulk fluids which can be propelled when rotated by an external magnetic field [15, 45, 46, 59–61, 63, 64].

These magnetic swimmers are one of the most promising types of microrobotic systems under current investigation. Compared to other swimmers, magnetic swimmers have advantages for *in vivo* use [36], since they do not require a potentially toxic chemical fuel, and magnetic fields permeate through tissue with little attenuation. Furthermore, swimmers rotated via a magnetic torque produced by field-dipole interactions can be scaled down to micro- and nanoscales unlike those which rely on magnetic forces produced by field gradient-dipole interactions. Although non-helical

magnetically rotated swimmers have been reported [46], nearly all such swimmers so far have been helical in geometry [45, 59–61, 63], mimicking the rigid helical flagella of bacteria. Thus, in this paper we focus on the swimming properties of helical geometries.

These swimmers are actuated by a magnetic field of magnitude H, which has a time-dependent direction that rotates with angular velocity $\boldsymbol{\omega}$. In typical experiments, the magnitude of the field is kept constant, while the rotation direction $\hat{\boldsymbol{\omega}}$ and frequency $\omega = |\boldsymbol{\omega}|$ are varied. The direction $\hat{\boldsymbol{\omega}}$ controls the swimming direction (along $\hat{\boldsymbol{\omega}}$), while the frequency ω is most often used to control the speed. Typically, the magnetic field is rotated in a plane perpendicular to its rotation axis, and we will focus on that case here.

One desirable feature for control is a linear relationship between velocity and frequency [3]. This allows simple proportional control of the swimming velocity as frequency is varied, and is especially useful for precise control if the linear relationship extends all the way to zero velocity. One way to achieve a linear velocity-frequency relationship is to maintain a constant axis of rotation as frequency changes [3, 46], but for generic geometries, the axis of rotation varies as frequency is changed while magnetic field strength stays constant [46]. Previous studies have observed these changes in rotation axis for magnetically rotated helices as frequency is varied [2,3,38]. The change in rotation axis leads to nonlinear velocity-frequency response and hinders ease of control. The rotation axis can be characterized by a "precession angle" (β), which is the angle the axis of rotation makes with the longitudinal helical axis (Fig. 5.1). For $\beta = 0°$, the swimmer rotates as designed around the helical axis, while for $\beta = 90°$ the swimmer rotates about an axis perpendicular to the helical axis, which has been called "tumbling." Rotation about intermediate axes with $0° < \beta < 90°$ has been called "wobbling." For example, Ghosh *et al.* [2] observed that helices

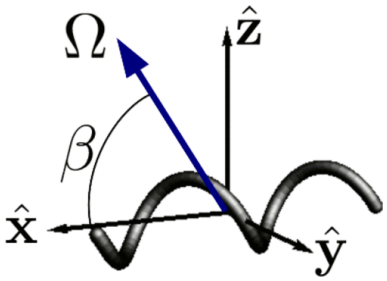

Figure 5.1: Rotation of the helix by angular velocity $\mathbf{\Omega}$ can be characterized by the precession angle β.

magnetized with moments which were not perpendicular to the helical axis tumble at the lowest frequencies, and show little forward propulsion. As frequency is increased past a critical frequency, the tumbling transitions to wobbling and the precession angle decreases while the velocity increases nonlinearly as frequency is further increased. The precession angle approaches zero and the swimming velocity peaks at the so-called step-out frequency. Beyond the step-out frequency, steady rotation is no longer possible since the magnetic torque is not large enough to rotate the swimmer as fast as the field, and the swimming velocity decreases.

The tumbling and wobbling of magnetically rotated helices has been theoretically examined in a number of previous studies. Man and Lauga [41] showed that during wobbling the precession angle scales as inverse frequency using numerics and asymptotics of nearly straight helices. Ghosh *et al.* [2,44] and Morozov and Leshansky [39] investigated the transition of stability from tumbling to wobbling behavior as frequency increases by treating the rotational dynamics as that of ellipsoids numerically and analytically, respectively.

Two studies have explored what types of magnetization are optimal for helical microswimmers. Recently, Peters *et al.* [3] proposed that wobbling can be eliminated by fabricating superparamagnetic helical microswimmers in a way such that the paramagnetic easy-axis is perpendicular to the helical axis. They showed that

microswimmers with such magnetization had much reduced wobbling compared to microswimmers with random easy-axis, as well as improved swimming characteristics. In addition, in a theoretical examination of the rotational and swimming behavior of helices with permanent magnetic dipole, Morozov and Leshansky [39] concluded that for such microswimmers, it is optimal to have the magnetic dipole perpendicular to the helical axis to minimize wobbling.

In previous publications [42, 46], we have described a modeling method for rigid magnetically rotated swimmers that is applicable for arbitrary geometries. The method identifies stable steady rotating orbits of the swimmer for given experimental conditions in terms of the rotation axis of the swimmer and the orientation of the swimmer relative to the magnetic field. Here, we apply our techniques to investigate how the magnetization direction and geometry of helical swimmers can be designed in order to control the rotation axis, reduce wobbling, and produce linear velocity-frequency response, which may enable simplified control, especially at the low speeds required for precise position control.

In the previous work on the rotational dynamics of helical microswimmers mentioned above [2, 39, 44], the rotational dynamics was approximated by the dynamics of an ellipsoid or rod, ignoring chirality and non-axisymmetry of the helix. Here, we treat the rotational dynamics of a truly helical geometry. We investigate theoretically whether the direction of magnetization can be used to guarantee wobble-free rotation about the helical axis, and find that it cannot. We show that although no moment can completely eliminate wobbling, there are ideal directions of magnetization that are optimal in the sense that they can guarantee linear velocity-frequency relationships. For helices with large aspect ratios (helical length/helical radius), the ideal magnetization directions are close to those suggested previously (i.e., perpendicular to the helical axis) by studies using the ellipsoidal approximation, and we provide a comparison to illustrate how the difference increases as the aspect ratio decreases. We

also compare swimming speeds predicted by our theory to those reported for helical swimmers in the literature and find good agreement. Finally, in the context of these ideal directions of magnetization, we investigate what helical geometries minimize wobbling and maximize velocities. Previous work investigating optimal shapes for helical swimmers [77] assumed that the rotation is along the helical axis; here we incorporate the full wobbling dynamics of helices rotated by magnetic fields.

In this work we use both resistive force theory [78] as well as the method of regularized stokeslets [51] to calculate mobility matrices for helical geometries. The resistive force theory is useful for obtaining analytical results which allow exploration of varying helical geometries, while the method of regularized stokeslets allows quantitative comparison with experiments. Resistive force theory is commonly used to investigate both artificial microswimmers as well as biological microswimmers, and by comparing the results of resistive force theory and the method of regularized stokeslets, we also show how thin the helix filament should be for the resistive force theory approximation to hold.

Besides its application to the helical swimmers, the work reported here also provides quantitative validation of the modeling technique used. In [46] and [42] we reported the technique as a method applicable to generic geometries, providing qualitative comparison to observations in [46], but did not quantitatively compare it to experimental results. The agreement between our model and experimental swimming speeds for helices lends support to the use of our model for a wide variety of geometries, including achiral geometries [46]. The potential insights allowed by our technique are demonstrated by investigations of stability in varying magnetic field conditions [42] as well as the rotational dynamics of helices reported here. Our model may be useful for designing effective microswimmers from a much larger geometry space than helical geometries alone. Furthermore, the conclusion that a moment perpendicular to the principal axis of the rotational mobility matrix leads to linear

velocity-frequency response applies to nonhelical geometries, which may be useful for general design of microswimmers.

5.3 Model and method

We follow the general framework for modeling the rotational propulsion of rigid bodies described in Ref. [42]. Here we summarize the essential features for the present study; for more details please see Ref. [42]. In the zero Reynolds number limit appropriate for microswimmers, the instantaneous velocity ($\mathbf{v}$) and angular velocity ($\mathbf{\Omega}$) applied to a rigid body are linearly related to the external force ($\mathbf{F}$) and torque ($\mathbf{N}$) through a 6×6 mobility matrix,

$$\begin{pmatrix} \mathbf{v} \\ \mathbf{\Omega} \end{pmatrix} = \begin{pmatrix} \mathbf{K} & \mathbf{C} \\ \mathbf{C}^{\mathsf{T}} & \mathbf{M} \end{pmatrix} \begin{pmatrix} \mathbf{F} \\ \mathbf{N} \end{pmatrix}. \tag{5.1}$$

In the above, $\mathbf{K}$, $\mathbf{M}$, and $\mathbf{C}$ are 3×3 submatrices that relate translations to forces, rotations to torques, and translations to torques, respectively. According to this definition $\mathbf{K}$ and $\mathbf{M}$ are positive definite.

In typical experiments, a uniform field interacts with a magnetic dipole to produce zero external force and a net torque $\mathbf{N} = (\mathbf{m} \times \mathbf{H})$, so the instantaneous angular velocity of the swimmer is

$$\mathbf{\Omega} = \mathbf{M}(\mathbf{m} \times \mathbf{H}). \tag{5.2}$$

A steady solution occurs when the angular velocity of the swimmer is equal to the angular velocity of the rotating magnetic field, so that in a body-fixed frame co-rotating with the swimmer, the magnetic field and hence angular velocity are

constant[1]. Thus a steady solution obeys

$$\mathbf{\Omega} = \boldsymbol{\omega} = \mathbf{M}(\mathbf{m} \times \mathbf{H}), \tag{5.3}$$

and finding steady solutions amounts to identifying pairs of $\mathbf{H}$ and $\boldsymbol{\omega}$ in the body-fixed frame that satisfy Eq. 5.3.

In many experiments, the magnetic field is rotated in a plane perpendicular to its rotation axis. In this work, we restrict ourselves to this condition unless explicitly stated otherwise. For such a field, the steady solutions can be found by finding the magnetic field directions which satisfy

$$0 = \hat{\mathbf{H}}^{\mathbf{T}}\mathbf{M}(\mathbf{m} \times \hat{\mathbf{H}}). \tag{5.4}$$

For example, the direction of the field can be specified using spherical coordinates defined in Fig. 5.2b,

$$\hat{\mathbf{H}} = (\cos\theta, \sin\theta\cos\phi, \sin\theta\sin\phi)\,, \tag{5.5}$$

in which case Eq. 5.4 provides a constraint on the angles (θ, ϕ).

Once the magnetic field direction for a steady solution is identified, the instantaneous swimming velocity can be calculated from Eq. 5.1 as $\mathbf{v} = \mathbf{CN} = \mathbf{C}(\mathbf{m} \times \mathbf{H})$, which is also constant in the body-fixed frame. The average swimming velocity over a rotation period is the component of the instantaneous swimming velocity along the rotation direction,

$$V_s = \mathbf{v} \cdot \hat{\mathbf{\Omega}}. \tag{5.6}$$

Note that while the instantaneous velocity, which has been used by others as a measure of swimming speed, depends on the origin chosen for the body-fixed frame, the

[1]Our definition of steady solution excludes the solutions with phase slip discussed by Ghosh *et al.* [44] and Morozov and Leshansky [39]

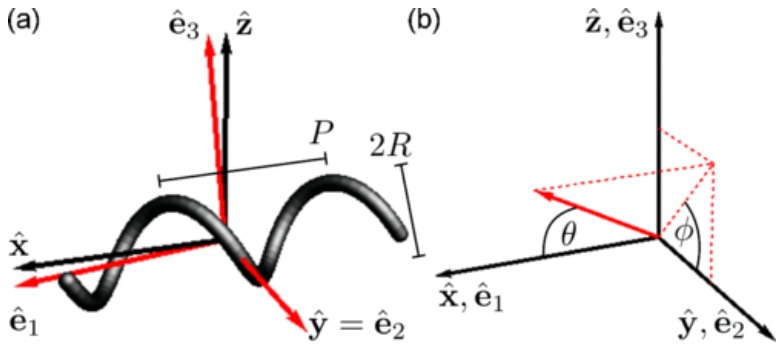

Figure 5.2: a) Helix with two turns, pitch P, and radius R. The helical axis is along $\hat{\mathbf{x}}$, and the helix is symmetric about a 180° rotation about $\hat{\mathbf{y}}$. The principal axes of the rotational mobility matrix $\mathbf{M}$ are $\hat{\mathbf{e}}_1$, $\hat{\mathbf{e}}_2$, and $\hat{\mathbf{e}}_3$. b)Angles ϕ and θ used for expressing the magnetic field direction $\hat{\mathbf{H}}$ in spherical coordinates. As specified in text, the angles may be used relative to the symmetry (x, y, z) axes or the principal (1,2,3) axes.

swimming velocity of Eq. 5.6 is independent of the choice of origin.

One way a linear relationship between swimming velocity and frequency can be achieved if the rotation axis remains constant as the frequency is altered. In that case, Eq. 5.2 implies that the torque $\mathbf{m} \times \mathbf{H}$ also has constant direction and increases in magnitude linearly with the frequency. Therefore $\mathbf{v}$ also has constant direction and increases linearly with frequency, and so Eq. 5.6 implies V_s increases linearly with frequency. Thus, maintaining a constant rotation axis for different frequencies can be viewed as a design goal for helical swimmers.

One way to achieve a constant rotation axis is to increase the magnetic field strength proportionally to the frequency as the frequency of the rotation is increased [46]. In this case, it should be clear that the magnetic field direction and rotation direction satisfying Eq. 5.2 remains fixed while both the field magnitude and frequency increase. However impractically large magnetic fields may be required at higher frequencies so we will search for other ways to achieve linear velocity-frequency response.

Steady solutions can be evaluated for stability by evaluating the eigenvalues of

the matrix $\mathbf{Q}$ [42],

$$Q_{in} = \left(M_{ij}\epsilon_{jkl}m_k\epsilon_{lmn}H_m - \epsilon_{ijn}M_{jl}\epsilon_{lmo}m_mH_o\right). \tag{5.7}$$

If the real parts of the eigenvalues are all negative, then the solution is stable, otherwise, it is unstable.

5.4 Mobility matrix for a helix

Consider a helix with centerline specified by

$$\mathbf{r}(\xi) = \xi\hat{\mathbf{x}} + R\cos(2\pi\chi\xi/P)\hat{\mathbf{y}} + R\sin(2\pi\chi\xi/P)\hat{\mathbf{z}}, \tag{5.8}$$

where P is the helical pitch, R is the helical radius, ξ varies from $-nP/2$ to $nP/2$, and n is the number of turns. (See Fig. 5.2a.) The parameter $\chi = \pm 1$ controls the chirality of the helix. Note that the arclength $s = \xi/\cos\alpha$, where $\alpha = \arctan(2\pi R/P)$ is the pitch angle.

In these coordinates, the helix is unchanged by the symmetry operation of a 180° rotation about the $\hat{\mathbf{y}}$ axis. Applying the symmetry arguments described in Chapter

5 of Happel of Brenner [73], the mobility matrix takes the form

$$\mathbf{K} = \begin{pmatrix} K_{xx} & 0 & K_{xz} \\ 0 & K_{yy} & 0 \\ K_{xz} & 0 & K_{zz} \end{pmatrix} \tag{5.9}$$

$$\mathbf{M} = \begin{pmatrix} M_{xx} & 0 & M_{xz} \\ 0 & M_{yy} & 0 \\ M_{xz} & 0 & M_{zz} \end{pmatrix} \tag{5.10}$$

$$\mathbf{C} = \begin{pmatrix} C_{xx} & 0 & C_{xz} \\ 0 & C_{yy} & 0 \\ C_{zx} & 0 & C_{zz} \end{pmatrix}. \tag{5.11}$$

In this study, we calculate the mobility matrix for a helix using resistive force theory [78], which is often applied to slender objects such as helical filaments. Although resistive force theory is not always quantitatively accurate [79], it is a convenient way to capture the qualitative dependence of the hydrodynamic mobility matrix on the helical geometry using analytic expressions. Consider a helix moving due to external forces and torques in a quiescent fluid. In resistive force theory, the force per unit length on a segment of the helix is

$$\mathbf{f}(\xi) = [\zeta_{\parallel}\hat{\mathbf{n}}\hat{\mathbf{n}} + \zeta_{\perp}(1 - \hat{\mathbf{n}}\hat{\mathbf{n}})]\mathbf{v}^{rel}(\xi), \tag{5.12}$$

where $\mathbf{v}^{rel}(\xi)$ is the velocity of the segment relative to the quiescent background, $\hat{\mathbf{n}}(\xi)$ is the tangent to the helix segment, and $\zeta_{\parallel}$ and $\zeta_{\perp}$ are the resistive force theory coefficients. The ratio $\zeta_{\perp}/\zeta_{\parallel}$ depends only logarithmically on the thickness of the helix relative to its pitch, so in this work, we keep the ratio constant ($\zeta_{\perp}/\zeta_{\parallel} = 2$) for

our qualitative investigations of the effects of varying helical geometry.

The total force $\mathbf{F}$ and torque $\mathbf{N}$ on the helix are

$$\mathbf{F} = \int_{-nP/2}^{nP/2} \frac{\mathrm{d}\xi}{\cos\alpha} \mathbf{f}(\xi) \tag{5.13}$$

$$\mathbf{N} = \int_{-nP/2}^{nP/2} \frac{\mathrm{d}\xi}{\cos\alpha} \mathbf{r}(\xi) \times \mathbf{f}(\xi) \tag{5.14}$$

If the helix undergoes rigid body motions with translational velocity $\mathbf{v}$ and angular velocity $\mathbf{\Omega}$, then $\mathbf{v}^{rel}(\xi) = \mathbf{v} + \Omega \times \mathbf{r}(\xi)$. Calculating the total force and torque when $\mathbf{v}$ and $\mathbf{\Omega}$ take values along cartesian directions yields the elements of the resistance matrix, which is the inverse of the mobility matrix. In the appendix we list the elements of the resistance matrix. The form of the matrix agrees with that predicted by the symmetry analysis.

5.5 Magnetization perpendicular to the helical axis does not lead to rotation about the helical axis.

Here we examine whether a permanent magnetic dipole oriented perpendicularly to the helical axis (*i.e.* in the y-z plane), similar to that proposed by Peters *et al.* [3] and Morozov and Leshansky [39], leads to rotation about the helical axis ($\Omega = \Omega\hat{\mathbf{x}}$) and hence no wobbling.

To do so, consider what moments and magnetic fields are needed to yield a rotation axis in the x-direction. The inverse of $\mathbf{M}$ has the same form as $\mathbf{M}$; call its nonzero elements

$$\mathbf{M}^{-1} = \begin{pmatrix} R_{xx} & 0 & R_{zx} \\ 0 & R_{yy} & 0 \\ R_{zx} & 0 & R_{zz} \end{pmatrix}. \tag{5.15}$$

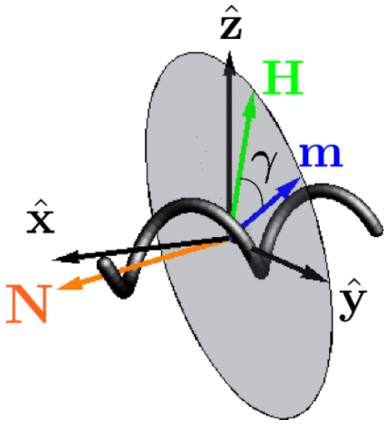

Figure 5.3: For a rotation axis along the helical axis ($\hat{\mathbf{x}}$), the torque $\mathbf{N}$ is not in the x-direction, and the moment $\mathbf{m}$ and field $\mathbf{H}$ lie in a plane perpendicular to the torque. As the rotation frequency changes, the angle $\mathbf{H}$ shifts to make a different angle γ with $\mathbf{m}$.

In order to achieve a rotation $\Omega\hat{\mathbf{x}}$, Eq. 5.2 requires that the torque $\mathbf{m} \times \mathbf{H} = \Omega(R_{xx}\hat{\mathbf{x}} + R_{zx}\hat{\mathbf{z}})$. Note that the helical geometry leads to off-diagonal elements R_{zx} so that the torque has a z as well as x component. To satisfy this torque, both $\mathbf{m}$ and $\mathbf{H}$ must lie in a plane perpendicular to $\Omega(R_{xx}\hat{\mathbf{x}} + R_{zx}\hat{\mathbf{z}})$ (see Fig. 5.3). Consider what happens as the frequency of rotation changes. For a given moment $\mathbf{m}$ in that plane, at small frequencies the field $\mathbf{H}$ will point in a direction close to $\mathbf{m}$. As frequency increases, $\mathbf{H}$ will rotate in the plane to make a larger angle with $\mathbf{m}$ and increase the torque. However, since the plane is perpendicular to $\Omega(R_{xx}\hat{\mathbf{x}} + R_{zx}\hat{\mathbf{z}})$ and not $\mathbf{\Omega} = \Omega\hat{\mathbf{x}}$, the angle between $\mathbf{H}$ and $\mathbf{\Omega}$ must change as the frequency changes. In particular, for almost all frequencies $\mathbf{H}$ will not be perpendicular to $\mathbf{\Omega}$. Thus, to achieve a rotation about the helical axis requires a careful tuning of the angle between the field and its rotation axis as the frequency changes, which may be difficult to implement experimentally.

The above argument applies to any moment in the plane perpendicular to the torque. Of those, only one is also perpendicular to the helical axis, $\mathbf{m} = m\hat{\mathbf{y}}$. Thus for a helical geometry, in contrast to what is suggested by the ellipsoidal approximation,

having a moment perpendicular to the helical axis does not lead to rotation about the helical axis for fields perpendicular to rotation. Is there another strategy that could be employed for easier control? Below, we show that although rotation about the helical axis is not easily achievable, one can still choose a moment to obtain linear velocity-frequency response.

5.6 Rotation about the principal axis of M.

Although the rotational mobility submatrix $\mathbf{M}$ is not diagonal when referred to the symmetry basis $\hat{\mathbf{x}}$, $\hat{\mathbf{y}}$, $\hat{\mathbf{z}}$, it is diagonal when referred to the principal axes $\hat{\mathbf{e}}_1$, $\hat{\mathbf{e}}_2$, $\hat{\mathbf{e}}_3$. Call the respective eigenvalues M_1, M_2, and M_3, which are all positive. For typical helices with large aspect ratio, M_{xz} is small compared to M_{xx} and M_{zz} and one of the eigenvectors of $\mathbf{M}$ will be close to $\hat{\mathbf{x}}$. Let $\hat{\mathbf{e}}_1$ be the principal axis closest to $\hat{\mathbf{x}}$. As the aspect ratio decreases, $\hat{\mathbf{e}}_1$ increasingly deviates from $\hat{\mathbf{x}}$. Below, we show that if the moment is chosen to lie perpendicular to $\hat{\mathbf{e}}_1$, then the rotation axis will be along $\hat{\mathbf{e}}_1$, independent of frequency, and there will be a linear velocity-frequency response.

First, consider how one could obtain rotation along the 1-direction ($\mathbf{\Omega} = \Omega\hat{\mathbf{e}}_1$). Repeating the argument from the previous section but in the principal axis frame, since the mobility matrix is now diagonal the torque is in the 1-direction, and $\mathbf{m}$ and $\mathbf{H}$ lie in the 2-3 plane. In this case, the 2-3 plane is always perpendicular to the rotation axis, so no tuning of the angle between the field and the rotation axis is necessary as frequency is changed.

To be more specific, consider a magnetic moment in the 2-3 plane, $\mathbf{m} = m_2\hat{\mathbf{e}}_2 + m_3\hat{\mathbf{e}}_3$. Specify the field direction using spherical coordinates as in Eq. 5.5, referred to the principal axes (i.e., θ is the angle between $\mathbf{H}$ and the 1-axis). Then, substituting

into Eq. 5.4, the field directions giving steady solutions satisfy the constraint

$$0 = \sin\theta\cos\theta\left[(M_1-M_2)m_3\cos\phi - (M_1-M_3)m_2\sin\phi\right]. \tag{5.16}$$

There are two families of solutions to the above constraint equation.

For the first family of solutions, $\theta = \pi/2$ and $\mathbf{H}$ is in the 2-3 plane ($\mathbf{H} = H_2\hat{\mathbf{e}}_2 + H_3\hat{\mathbf{e}}_3$), leading to

$$\mathbf{\Omega} = M_1(m_2H_3 - m_3H_2)\hat{\mathbf{e}_1}. \tag{5.17}$$

This is the solution discussed two paragraphs above, and is similar to the "propulsive" or "wobbling" solutions found under the ellipsoidal approximation employed by Ghosh *et al.* [2, 44] and Morozov and Leshansky [39, 80]. Since the rotation axis is always in the 1-direction, it will have a linear velocity-frequency response. This solution exists as long as $\omega < M_1mH$, the step-out frequency.

The second family of solutions is specified by

$$\tan\phi = \frac{(M_1 - M_2)m_3}{(M_1 - M_3)m_2} \tag{5.18}$$

for any value of θ. (Note that this includes solutions to Eq. 5.16 with $\theta = 0$.) Referred to the principal axes, the corresponding field directions are given by

$$\hat{\mathbf{H}} = \left[\cos\theta, \pm\sin\theta\frac{(M_1 - M_3)m_2}{\sqrt{(M_1 - M_2)^2m_3^2 + (M_1 - M_3)^2m_2^2}}, \pm\sin\theta\frac{(M_1 - M_2)m_3}{\sqrt{(M_1 - M_2)^2m_3^2 + (M_1 - M_3)^2m_2^2}}\right] \tag{5.19}$$

$$\mathbf{\Omega} = H\left[\mp\frac{M_1m_2m_3(M_2 - M_3)\sin\theta}{\sqrt{(M_1 - M_2)^2m_3^2 - (M_1 - M_3)^2m_2^2}}, M_2m_3\cos\theta, -m_2M_3\cos\theta\right]. \tag{5.20}$$

V_s can be found by direct substitution of $\hat{\mathbf{H}}$ and $\mathbf{\Omega}$ into Eq. 5.6, but the expression

is not illuminating and too unwieldy to write explicitly here. As we will see using a specific example below, this solution corresponds to "tumbling" rotation.

Note that although any moment in the 2-3 plane has a solution with constant rotation axis along the first principal direction, it may be hard to experimentally realize such moments, since aligning swimmers with the principal, as opposed to symmetry, axes may be difficult. However, $\hat{\mathbf{e}}_2 = \hat{\mathbf{y}}$ is perpendicular to both the symmetry and principal axis, and may be feasible to achieve during fabrication. For example, if helices made by glancing angle deposition [61] are magnetized while still attached to substrate, identification of the 180° symmetry axis corresponds to picking a particular direction parallel to the substrate. Therefore, in some sense magnetization along $\hat{\mathbf{e}}_2 = \hat{\mathbf{y}}$ is the most practical option and we investigate it in more detail below.

5.6.1 Moment along 2-direction

For the case of a moment $\mathbf{m} = m_2\hat{\mathbf{e}}_2$ along the 2- (or equivalently y-) direction the above two families of solutions simplify to

$$\begin{aligned} \mathbf{\Omega} &= M_1 m_2 H_3 \hat{\mathbf{e}}_1 = H M_1 m_2 \sin\phi \hat{\mathbf{e}}_1 && (5.21)\\ \mathbf{H} &= H(\cos\phi\hat{\mathbf{e}}_2 + \sin\phi\hat{\mathbf{e}}_3) && (5.22)\\ V_s &= |m_2 H_3| C_{11} = \omega C_{11}/M_1 && (5.23) \end{aligned}$$

for the first family and

$$\begin{aligned} \mathbf{\Omega} &= -M_3 m_2 H_1 \hat{\mathbf{e}}_3 = -H M_3 m_2 \cos\theta \hat{\mathbf{e}}_3 && (5.24)\\ \mathbf{H} &= H(\cos\theta\hat{\mathbf{e}}_1 \pm \sin\theta\hat{\mathbf{e}}_2) && (5.25)\\ V_s &= |m_2 H_1| C_{33} = \omega C_{33}/M_3 && (5.26) \end{aligned}$$

for the second family. It should be clear now that the since the second family rotates about the third principal axis, it is rotating about an axis which is nearly perpendicular to the helical axis and represents the "tumbling" solution. The first family has two solutions with opposite signs of $\mathbf{\Omega}$ for $0 < \omega < |HM_1m_2|$ (corresponding to ϕ and $\phi + \pi$), while the second family has two solutions for $0 < \omega < |HM_3m_2|$ (corresponding to the $\pm$).

Both families are steady solutions, but to determine which solutions are realized experimentally we must evaluate the stability. For the first family, $\mathbf{Q}$ in Eq. 5.7 is

$$\mathbf{Q} = H \begin{pmatrix} -m_2 M_1 \cos\phi & 0 & 0 \\ 0 & 0 & m_2 M_1 \sin\phi \\ 0 & -m_2(M_1 - M_3)\sin\phi & -m_2 M_3 \cos\phi \end{pmatrix}. \tag{5.27}$$

The eigenvalues are $\lambda_1 = -M_1 m_2 \cos\phi$ and $\lambda_\pm = (A \pm \sqrt{A^2 + 4BC})/2$, with $A = -m_2 M_3 \cos\phi$, $B = M_1 m_2 \sin\phi$, and $C = -m_2(M_1 - M_3)\sin\phi$. For all helices we have examined, $M_1 > M_3$. Thus $BC = -m_2^2 M_1 (M_1 - M_3)\sin^2\phi < 0$ and the real parts of $\lambda_\pm$ are both negative if and only if $A = -m_2 M_3 \cos\phi < 0$. Therefore stability occurs for $-\pi/2 < \phi < \pi/2$ if $m_2 > 0$ but for $\pi/2 < \phi < 3\pi/2$ if $m_2 < 0$, and in general a stable solution exists for the whole range of ω where there are steady solutions.

For the second family, $\mathbf{Q}$ is

$$\mathbf{Q} = H \begin{pmatrix} \mp m_2 M_1 \sin\theta & m_2(M_1 - M_3)\cos\theta & 0 \\ m_2 M_3 \cos\theta & 0 & 0 \\ 0 & 0 & \mp m_2 M_3 \sin\theta \end{pmatrix} \tag{5.28}$$

The eigenvalues are $\lambda_3 = \mp m_2 M_3 \sin\theta$, and $\lambda_\pm = (A \pm \sqrt{A^2 + 4BC})/2$, where

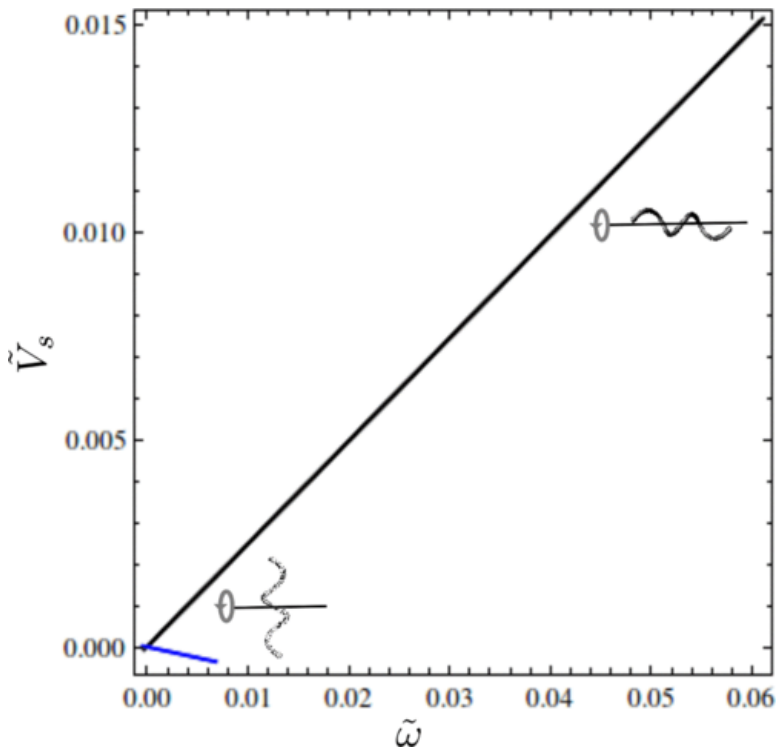

Figure 5.4: The swimming velocity vs frequency for the stable solutions of a rotating helix with 2 turns, $P = 4R$, $\chi = 1$, and a moment along the y-direction. The lower branch corresponds to rotation around an axis with precession angle $\beta = 85°$, while the upper branch corresponds to rotation around an axis with precession angle $\beta = 4.9°$

now $A = \mp m_2 M_1 \sin\theta$, $B = m_2 M_3 \cos\theta$, and $C = m_2(M_1 - M_3)\cos\theta$. In this case, $BC = m_2^2(M_1 - M_3)\cos^2\theta > 0$, so that one of the eigenvalues $\lambda_\pm$ is always positive and the other negative. Thus the second family of solutions is always unstable.

In Fig. 5.4 we plot the swimming velocity versus the frequency for the first and second families of solutions, for a helix with $n = 2$, $P = 4R$ and chirality $\chi = 1$. In the plots we use the dimensionless frequency specified by $\tilde{\omega} = \omega\zeta_\parallel R^3/(mH)$, and the dimensionless velocity $\tilde{V}_s = V_s\zeta_\parallel R^2/(mH)$. Note that for a given swimmer, the nondimensionalization of V_s that we use is not affected by changes in frequency [unlike another possibility, $V_s/(\omega R)$]; thus, our plots directly reflect the dimensional velocity-frequency plots commonly presented for experimental swimmers. For this chirality

$C_{11} > 0$ and $C_{33} < 0$, so the stable first family is the one with positive slope that exists over a larger range.

For this geometry of helix ($n = 2$, $P = 4R$), we can also characterize the rotation via the precession angle β (Fig. 5.1), which is the angle the axis of rotation makes with the helical axis ($\hat{\mathbf{x}}$). For the first family, this is just the angle between $\hat{\mathbf{e}}_1$ and $\hat{\mathbf{x}}$, giving $\beta = 4.9°$, while for the second family, it is the angle between $\hat{\mathbf{e}}_3$ and $\hat{\mathbf{x}}$, giving $\beta = 85°$.

To conclude this section, we have shown that a moment perpendicular to the principal axis rather than helical axis leads to a linear velocity-frequency response. Although the resulting rotation axis (along $\hat{\mathbf{e}}_1$) is not along the helical axis, for many helices it is relatively close. The dependence of precession angle on helical geometry will be explored in more detail in Section 5.9. Finally, note that although we only analytically proved that the propulsion solution is stable and tumbling solution is unstable for moment along the 2-direction, for all helical geometries we have tested, we observed numerically that only the propulsive solution is stable so long as the moment is perpendicular to the first principal axis.

5.7 Comparison to experimental swimming speeds

To validate our results, we compare to experimental results for microswimmers. The examples of microscale swimming magnetic helices in the literature do not exactly correspond with the scenario which we discuss here. Ghosh and Fischer [61] and Ghosh *et al.* [2] examine permanently magnetized helical swimmers with attached heads (which therefore do not have the symmetry of a helix). Other swimmers are soft ferromagnetic helices with heads (e.g., [60]). While Peters *et al.* [3] examine a helical ribbon with no head, their swimmer is paramagnetic. Nonetheless, we can make rough comparisons between these and our calculations to ensure that our models

are reasonable. Because typically the magnetic moment of these swimmers is not measured the most appropriate measure for comparison is the slope of the velocity-frequency curve when nearly linear behavior is observed. If the frequency is measured in Hertz (revolutions/second), the slope corresponds to the distance traveled per revolution, which is a property dependent only on the geometry of the helix in our model. Therefore, in the following we calculate the slope for the propulsion solution with rotation about the first principal axis of $\mathbf{M}$, and compare to experimental results.

Ghosh *et al.* [2] report artificial swimmers that consist of a spherical head attached to a helix, which has a filament diameter which tapers at the end away from the head. In their paper, they find that swimming speeds are best modeled using an "effective pitch," the amount of translation after one revolution about the helical axis, of 0.08 pitches/revolution. The effective pitch is independent of the moment direction and is a property of geometry of the helix. We model the tail as a helix with constant diameter (see Appendix for details). In Sections 5.6, 5.8, and 5.9, we use resistive force theory to calculate mobility matrices. Although resistive force theory is useful for obtaining analytical expressions that reflect the symmetry of helices and can reveal qualitative trends, it is not expected to be quantitatively accurate for experimental swimmers with thick filaments. We find that resistive force theory is only accurate for filament radii less than $0.035P$, which are much thinner than experimental microswimmers (see Appendix for details).

Thus, we calculate the mobility matrix using the method of regularized stokeslets [51] (see Appendix for details). For our model helix, we calculate a velocity-frequency slope of 0.09 pitches, and a precession angle of $< 1°$, which means that the rotation axis is nearly the same as the helical axis. Our calculation does not include the spherical head; its effect can be approximated by calculating the increase in drag in the direction of the helical axis when a head is included in the mobility matrix calculation, and decreasing the effective pitch by the same proportion. With this correction,

the estimated velocity-frequency slope is 0.085 pitches/revolution, comparable to the experimental effective pitch of 0.08 pitches/revolution.

Peters *et al.* [3] report superparamagnetic ribbons wound into a helix with no head, which they can rotate nearly without wobble. Again, for such a thick and noncircular cross section resistive force theory is not expected to be accurate so we calculate the mobility matrix using the method of regularized Stokeslets (see Appendix for geometry). The resulting velocity-frequency slope is 2.64 microns/revolution, which is in good agreement with the slopes from Figs. 8 and 9 of Peters *et al.*, which have slopes of $2.6 - 2.8\mu$m/revolution.

In contrast, Ghosh and Fischer [61] report a microswimmer with similar (but smaller) geometry to that of Ghosh *et al.* [2], and find that the velocity corresponds to 0.64 pitches per revolution. However, our model for this helix (see Appendix for details) leads to a velocity-frequency slope about an order of magnitude smaller. We cannot explain the discrepancy; but we note that in addition to being inconsistent with our calculation, the quite large value of 0.64 pitches per revolution is also inconsistent with the effective pitch reported by Ghosh *et al.* [2] as well as biological helical propulsion, which always involves a significant amount of slip of the helix with respect to the fluid.

Based on our numerics and the imprecision of microswimmer geometries, we expect our results to be accurate within 15% (see Appendix for details). Thus, the results for our model are in good overall agreement with the results from two different research groups (Ghosh *et al.* [2] and Peters *et al.* [3]).

5.8 Comparison to moment perpendicular to helical axis

In this section, we calculate the rotational and swimming dynamics for a moment along $\hat{\mathbf{z}}$, which is perpendicular to the helical axis, but not perpendicular to the principal axis. We compare it to the case described in section 5.6 to show how moments perpendicular to the helical axis can lead to undesirable swimming properties.

Returning to Eq. 5.4, but referred to the symmetry axes $\hat{\mathbf{x}}, \hat{\mathbf{y}}, \hat{\mathbf{z}}$, we substitute magnetic field directions specified in spherical coordinates by Eq. 5.5, where θ is the angle from the x-direction. This yields

$$0 = -m_3 \cos\phi \sin\theta \left[(M_x - M_y) \cos\theta + M_{xz} \sin\phi \sin\theta \right], \tag{5.29}$$

which admits solutions for steady orbits in two families.

The first family is specified by

$$\tan\theta = -\frac{M_x - M_y}{M_{xz} \sin\phi} \tag{5.30}$$

or

$$\mathbf{H} = \frac{[M_{xz} \sin\phi \hat{\mathbf{x}} + (M_y - M_x) \cos\phi \hat{\mathbf{y}} + (M_y - M_x) \sin\phi \hat{\mathbf{z}}]}{\sqrt{M_{xz}^2 \sin^2\phi + (M_x - M_y)^2}}. \tag{5.31}$$

From this equation, $\mathbf{\Omega}$ and V_s can be obtained by substitution into Eqs. 5.2 and 5.6, but the expressions are not illuminating so we do not write them here. This solution corresponds to the previously observed wobbling solutions [2].

The second family has $\phi = \pi/2$ and $\mathbf{H}$ in the x-z plane,

$$\mathbf{H} = H(\cos\theta\hat{\mathbf{x}} + \sin\theta\hat{\mathbf{z}}) \tag{5.32}$$

$$\mathbf{\Omega} = M_y m_z H_x \hat{\mathbf{y}} = H M_y m_z \cos\theta\hat{\mathbf{y}} \tag{5.33}$$

$$V_s = C_{yy}|m_z H_x| = \omega C_{yy}/M_y, \tag{5.34}$$

which represents a tumbling solution around the y-axis with linear velocity-frequency response.

Performing a stability analysis on the two families of solutions reveals that the tumbling solutions are stable at the lowest frequencies up to a critical frequency and become unstable at frequencies above the critical frequency ω_c. Below the critical frequency, the first family of solutions is unstable, but above it the first family of solutions is stable. This is similar to the behavior of ellipsoids with magnetic moments which are not perpendicular to the long axis in studies where the geometry of a helix is approximated as an ellipsoid [39, 44].

We can obtain an expression for the critical frequency by examining the stability matrix $\mathbf{Q}$ of Eq. 5.7 for the second (tumbling) family, which is

$$\mathbf{Q} = H m_z \begin{pmatrix} -M_x\sin\theta & 0 & (M_x - M_y)\cos\theta \\ 0 & -M_y\sin\theta & 0 \\ M_y\cos\theta - M_{xz}\sin\theta & 0 & M_{xz}\cos\theta \end{pmatrix}. \tag{5.35}$$

The eigenvalues are $\lambda_1 = -M_y\sin\theta$, which is less than zero over the entire range of θ, and $\lambda_\pm = [(A+D) \pm \sqrt{(A+D)^2 - 4(AD-BC)}]/2$. Here, $A = -M_x\sin\theta$, $B = (M_x - M_y)\cos\theta$, $C = M_y\cos\theta - M_{xz}\sin\theta$, and $D = M_{xz}\cos\theta$. In order for the tumbling solution to be stable, both of the $\lambda_\pm$ must also be negative, which requires

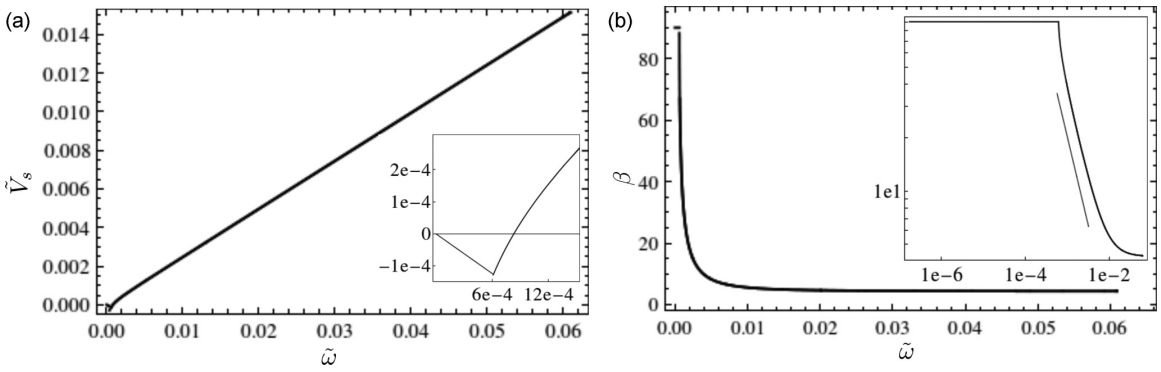

Figure 5.5: The a) swimming velocity and b) precession angle vs frequency for the stable solutions of a rotating helix with 2 turns, $P = 4R$, and a moment along the z-direction, which is perpendicular to the helical axis but not the first principal axis. The inset to (a) zooms into the low frequency regime, illustrating the transition between tumbling with rotation about the y-axis at the smallest frequencies, to wobbling rotation with varying precession angle at frequencies above the critical frequency ω_c. The inset to (b) shows a log-log plot of the precession angle vs frequency. The straight line has slope -1, demonstrating the relation $\beta \sim \omega^{-1}$.

that both $(A + D) < 0$ and $(AD - BC) > 0$. Using Eq. 5.33, it can be shown that if $M_x > M_y$ (which holds for helices with aspect ratio larger than 1), then both inequalities are satisfied for

$$\omega^2 < \omega_c^2 = \frac{(m_z M_y H)^2}{1 + (M_x - M_y)^2 / M_{xz}^2}. \tag{5.36}$$

In Fig. 5.5a, we plot the (nondimensional) velocity vs frequency for the stable solution as a function of frequency, for a helix with $n = 2$, $P = 4R$. The inset shows the transition from the tumbling solution at low frequencies to the wobbling solution above ω_c. Note that both the existence of the transition and the frequency dependence of the wobbling solutions lead to nonlinear dependence of the velocity on frequency, which are disadvantageous for precise swimmer control, especially at low frequencies. At higher frequencies the velocity depends on the frequency nearly linearly. The form of the dependence is similar to that observed for helices by Ghosh

et al. [2], and modeled for ellipsoids with moment non-perpendicular to the long axis by Ghosh *et al.* [44] and Morozov and Leshansky [39]. However, those previous studies had found that in the ellipsoidal approximation, any moment perpendicular to the helical axis did not have stable tumbling solutions. Here, we show that by taking into account the helical geometry, even moments perpendicular to the helical axis lead to tumbling-wobbling transitions and nonlinear velocity-frequency response. In order to achieve the linear velocity-frequency response, one must instead target rotation about the principal axis using a moment perpendicular to $\hat{\mathbf{e}}_1$.

In Fig. 5.5b, we plot the precession angle β as a function of frequency for the stable solution. Below the critical frequency, the tumbling solution rotates around the y-axis, so $\beta = 90°$. Above the critical frequency, the wobbling solution starts with $\beta = 90°$ and decreases as frequency increases. Man and Lauga have shown that $\beta \sim \omega^{-1}$ for asymptotically straight helices. In the inset of Fig. 5.5b, we plot the precession angle as a function of frequency in a log-log plot, to show that for a range of frequencies our precession angle has the same ω^{-1} dependence (straight line).

Fig. 5.5 shows that for a helix with $n = 2$ and $P = 4R$, the critical frequency is relatively small compared the the step-out frequency, so that the nonlinear response regime is quite small. Is the nonlinear response regime always small? To investigate this, in Fig. 5.6 we plot the velocity-frequency response for helices with a number of different geometries. The general trend is that as the aspect ratio (helix length/helix diameter) decreases, the critical frequency increases and the nonlinear regime grows in size. For a helix with $n = 1$ and $P = 2R$, ω_c is about a third of the stepout frequency, and the nonlinear regime is a significant portion of the frequency range below stepout. Thus results from the ellipsoidal approximations, which predict that rotation about the helical axis can be achieved for moments perpendicular to the helical axis, fail strongly when the aspect raio of helices is no longer large.

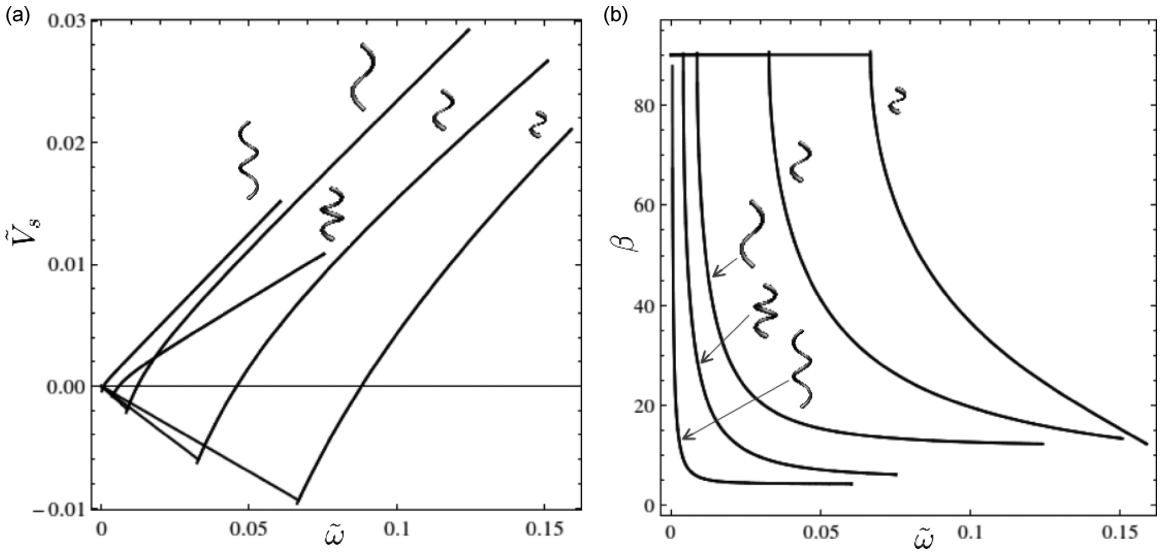

Figure 5.6: The swimming velocity (a) and precession angle (b) vs frequency for the stable solutions of rotating helices with moment along the z-direction. From left to right [for (a), as measured by location of sketched helices], and bottom to top [for (b)], curves correspond to helices with: 2 turns, $P = 4R$ [same case as in Fig. 5.5]; 2 turns, $P = 2R$; 1 turn, $P = 5R$; 1 turn, $P = 3R$; 1 turn, $P = 2R$. Curves are only plotted for frequencies below the step-out frequency. As the aspect ratio (length/diameter) of the helix decreases, a greater portion of frequencies below stepout exhibit tumbling rotation.

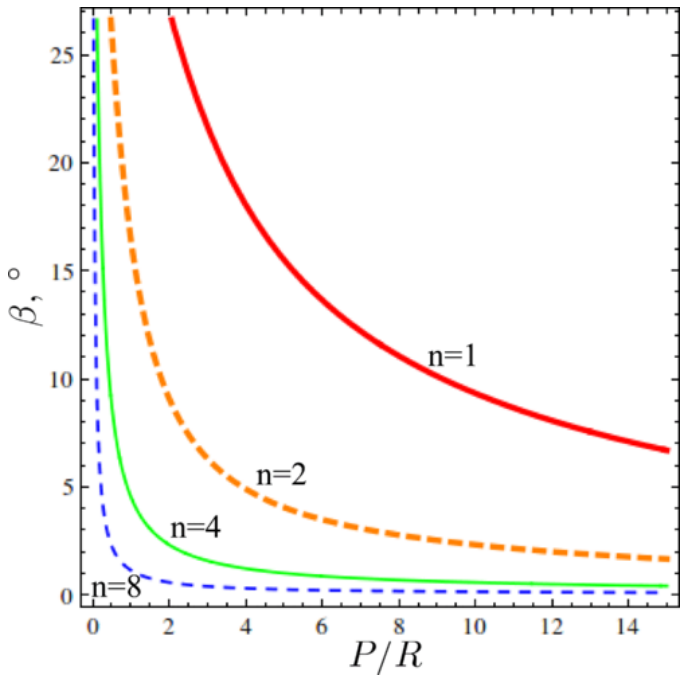

Figure 5.7: The precession angle of a helix with moment along the y-direction, perpendicular to the first principal axis, as a function of ratio of helical pitch and radius (P/R), for helices with different numbers of turns: one turn (red, thick solid), 2 turns (orange, thick dashed), 4 turns (green, thin solid), and 8 turns (blue, thin dashed).

5.9 Dependence on helical geometry

In this section, we continue to investigate the influence of helical geometry on swimming properties. We return to our proposed moment $\mathbf{m} = m_2\hat{\mathbf{y}}$ which is perpendicular to the principal axis $\hat{\mathbf{e}}_1$ and leads to rotation about $\hat{\mathbf{e}}_1$ and a linear velocity-frequency response. For this moment direction, we investigate what helical geometries will lead to a) low precession angles, b) maximum velocity:frequency slopes, and c) greatest maximum velocity.

In Fig. 5.7 we plot the precession angle of the swimmer as a function of helical pitch for various numbers of turns. Recall that this precession angle is simply the angle between $\hat{\mathbf{e}}_1$ and the x-axis. A small precession angle may be desirable if one wishes to precisely control the location of the tip of the helix during swimming. Typically, the

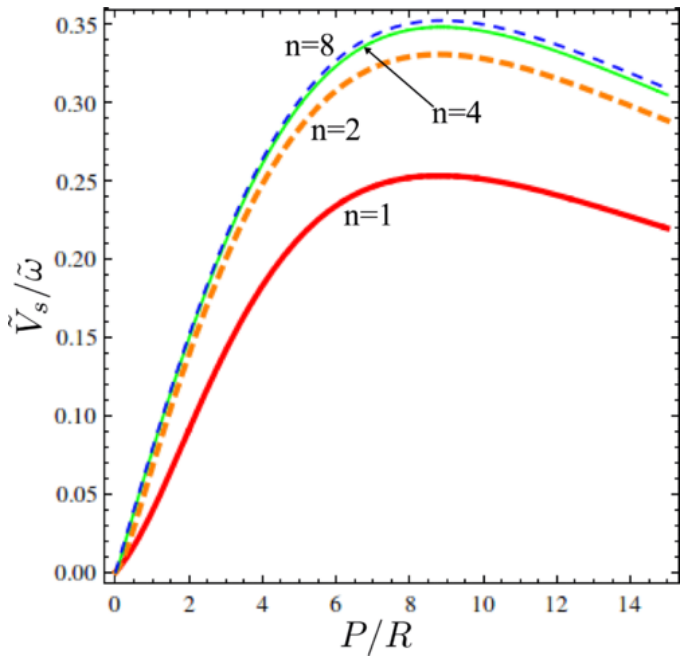

Figure 5.8: The velocity:frequency ratio of a helix with moment along the y-direction, perpendicular to the first principal axis, as a function of ratio of helical pitch and radius (P/R), for helices with different numbers of turns: one turn (red, thick solid), 2 turns (orange, thick dashed), 4 turns (green, thin solid), and 8 turns (blue, thin dashed).

precession angle decreases for larger aspect ratios. Specifically, in order to achieve a precession angle $\beta < 10°$, for $n \geq 2$ the pitch must satisfy $P > 2R$, while for $n = 1$, the pitch must satisfy $P > 8$. These results are in accord with the arguments made by Morozov and Leshansky about the effect of helical geometry on rotational dynamics modeled using ellipsoids [39]; here we quantify how the helical geometry leads to a breakdown of the ellipsoidal approximation.

In Fig. 5.8 we plot the slope of the velocity-frequency response $\tilde{V}_s/\tilde{\omega}$ of the swimmer as a function of helical pitch for various numbers of turns. Recall that the dimensionless frequency is $\tilde{\omega} = \omega\zeta_{\|}R^3/(mH)$, and the dimensionless velocity is $\tilde{V}_s = V_s\zeta_{\|}R^2/(mH)$; thus the dimensionless slope is nondimensionalized by the helical radius R, *i.e.* $\tilde{V}_s/\tilde{\omega} = (V_s/\omega)/R$. Therefore, Fig. 5.8 is best interpreted as

investigating the variation of the slope as the helical pitch changes but the helical radius stays fixed.

For a fixed number of turns, the maximum slope occurs for a pitch around 8-10 R. As the number of turns increases, the slope increases, but saturates around $n = 8$.

In Fig. 5.9a we plot the maximum velocity $\tilde{V}_s^{max}$ of the swimmer as a function of helical pitch for various numbers of turns. Note that the maximum velocity is distinct from the velocity:frequency slope, since it is the product of the velocity:frequency slope and the step-out frequency. The choice of whether it is more important to optimize velocity:frequency slope or maximum velocity depends on the application. For a fixed number of turns, the maximum velocity occurs for pitches around 4-6 R, at smaller pitch values than the maximum slope. This can be rationalized by observing how the step-out frequency $\tilde{\omega}^{stepout}$ behaves for different helical geometries, as plotted in Fig. 5.9b. For a fixed number of turns, the stepout frequency is highest for small pitches near R. Since the maximum velocity is the product of the slope (Fig. 5.8) and the stepout frequency (Fig. 5.9b), it at intermediate pitch. Similarly, one can rationalize why swimmers with many turns ($n = 8$) have the largest velocity:frequency slope in Fig. 5.8 but the smallest maximum velocity in Fig. 5.9; the large velocity:frequency slope is multiplied by a small step-out frequency (Fig. 5.9b) to yield small maximum velocities.

Based on Fig. 5.9a, the fastest swimmers would be obtained for $n = 1$ and $P \approx 5R$; however, these would have relatively large precession angles ($\beta \approx 15°$). For $n = 2$ and $P = 4R$, the maximum velocity is about half as much, but the precession angle is reduced to $\beta \approx 5°$.

Note that all the discussion of geometrical dependence in this section uses the helical radius R to nondimensionalize the velocities. Thus, the results should be interpreted as keeping the helical radius R fixed while the pitch and number of turns are varied. For the most common fabrication processes, it is easiest to maintain

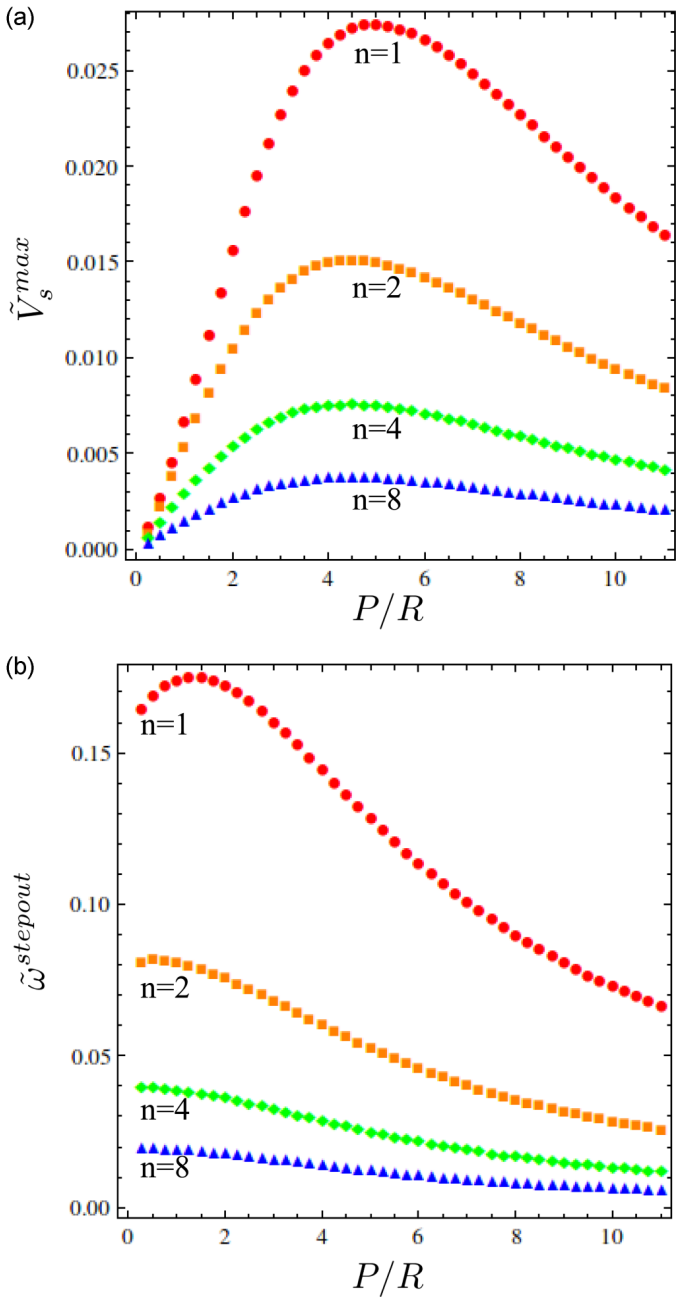

Figure 5.9: a) The maximum velocity of a helix with moment along the y-direction, perpendicular to the first principal axis, as a function of ratio of helical pitch and radius (P/R), for helices with different numbers of turns: one turn (red, circles), 2 turns (orange, squares), 4 turns (green, diamonds), and 8 turns (blue, triangles). b) The step-out frequency of the same helices as a function of P/R.

constant helical radius R as we have done. However, if one wished to design helices with varying R, the results would be different since the scaling of our plotted results with R would need to be taken into account.

5.10 Discussion

We investigated the rotational and swimming dynamics of rigid helical microswimmers rotated by an external magnetic field. We investigated how the rotation axis and dependence of velocity on frequency is affected by the direction of magnetic moment and geometry of the helix. We use resistive force theory to obtain mobility matrices that capture the helical geometry of the swimmers, going beyond approximations which treat the rotational dynamics of such swimmers as that of ellipsoids. A linear velocity-frequency response is desirable for control of such microswimmers, and we show that this can be achieved by choosing the magnetic moment to lie perpendicular to the principal axis closest to the helical axis, which results in a single stable branch of solutions which all rotate about the principal axis. We also show that moments which are perpendicular to the helical axis rather than the principal axis lead to nonlinear velocity-frequency response including a transition between low-frequency tumbling and high-frequency wobbling dynamics. Finally, we explored the dependence of swimming properties on helical geometry in the context of our proposed moment perpendicular to the principal axis. Precession angle, the slope of the velocity-frequency response, and maximum velocity were optimized for different helical geometries.

Our work used the resistive force theory to obtain qualitatively accurate mobility matrices for the helical swimmers. The resistive force theory is sufficient to investigate the trends in behavior by providing a convenient way to calculate the mobility matrices for arbitrary helical pitch and radius, and is sufficient to explore qualita-

tive features of linear velocity-frequency relationships. While resistive force theory is accurate for very slender helix filaments, we used a boundary element method to obtain quantitatively accurate mobility matrices for the thicker helices fabricated in experiments so far and obtained good agreement between our calculated swimming speeds and experimental results.

We assumed a helical geometry, but if a non-helical geometry is used, the mobility matrix may be more complicated than Eq. 5.1 due to a loss of the 180° rotation symmetry. For example, although a helical microswimmer with a head or cargo [60,61] will not have the symmetries we used in our analysis, this can be addressed in two ways. First, if a second head is attached at the other end of the swimmer, the symmetry upon 180° rotation may be restored. Second, even if the swimmer is not symmetric, one can identify the principal axes of its mobility matrix. In that case, the results of Section 5.6 apply insofar as a moment perpendicular to a principal axis will admit steady rotational solutions about the principal axis for a range of frequencies. In addition, rotation about the principal axis with the smallest rotational mobility eigenvalue will be stable.

Our work differs from that of Ghosh *et al.* [44] and Morozov and Leshansky [39] in that they approximate the rotational dynamics as those of an magnetized ellipsoid. One conclusion of their work is that a magnetization perpendicular to the helical axis can reduce wobbling and lead to rotation about the helical axis. As shown in Sections 5.5–5.8, using the true helical geometry means that rotation about the helical axis is not actually feasible, and instead rotation about the principal axis, which differs from the helical axis, is a better target. Incorporating the helical geometry, we find tumbling-wobbling transitions and nonlinear velocity-frequency response even when the moment is perpendicular to the helical axis. Although the difference between principal axis and helical axis is small for helices with large aspect ratio, which justifies the ellipsoidal approximation in those cases, the principal axis and helical axis can be

significantly different for helices with smaller aspect ratios. Thus, the helical geometry alters the conclusions of those earlier studies in a manner which may be significant for the design of microswimmers. We propose that the most convenient moment to target experimentally is one which is perpendicular to both the first principal axis and the helical axis, rather than any direction perpendicular to the helical axis.

In this work we assumed a permanent magnetic dipole and ignored paramagnetic response of the swimmers. Such response has been addressed by Morozov and Leshansky [80]. In that study, rotational dynamics are approximated as that of an ellipsoid, and we would expect that taking into account the helical geometry may yield similar differences with the ellipsoidal approximation that we have found in the case of a permanent magnetic dipole. Note that in particular the paramagnetic response would be expected to alter the linear velocity-frequency relations found in this work.

In this work we also ignored interactions with boundaries and walls. Although many research groups have explored magnetically rotated microswimmers which "roll" along surfaces, the modeling techniques used here are not directly applicable since the presence of the wall means that the steady solutions found here do not exist; instead there is a time-dependent mobility matrix as the swimmer rotates relative to the wall. Treatment of such cases would require integration of such unsteady rotational orbits, and we do not expect our statements about rotation axes to hold when interaction with surfaces and boundaries becomes strong.

5.11 Acknowledgments

This work was supported by National Science Foundation awards (DMR-1307497 and CMMI-1435652) to HF.

5.12 Appendix A: Resistance and mobility matrix for a helix

Here we report the coefficients of the resistance matrix for a helix with pitch P, radius R, and n turns calculated using resistive force theory as described in the main text. Due to the symmetry, the resistance matrix $\mathbf{D}$ has the same nonzero elements as the mobility matrix in the $\hat{\mathbf{x}}$, $\hat{\mathbf{y}}$, $\hat{\mathbf{z}}$ basis,

$$\mathbf{D} = \begin{pmatrix} D_{11} & 0 & D_{13} & D_{14} & 0 & D_{16} \\ 0 & D_{22} & 0 & 0 & D_{25} & 0 \\ D_{13} & 0 & D_{33} & D_{34} & 0 & D_{36} \\ D_{14} & 0 & D_{34} & D_{44} & 0 & D_{46} \\ 0 & D_{25} & 0 & 0 & D_{55} & 0 \\ D_{16} & 0 & D_{36} & D_{46} & 0 & D_{66} \end{pmatrix} \tag{5.37}$$

For integer n, the elements above are specified by:

$$
\begin{aligned}
D_{11} &= (\zeta_{\parallel}R)n\left(\tilde{P}\cos\alpha + 2\pi\tilde{\zeta}_{\perp}\sin\alpha\right) && (5.38)\\
D_{22} &= -(\zeta_{\parallel}R)\pi n\left[(\tilde{\zeta}_{\perp}-1)\sin\alpha - 2\tilde{\zeta}_{\perp}/\sin\alpha\right] && (5.39)\\
D_{33} &= D_{22} && (5.40)\\
D_{13} &= 0 && (5.41)\\
D_{44} &= -(\zeta_{\parallel}R^3)2\pi n\left[(\tilde{\zeta}_{\perp}-1)\sin\alpha - \tilde{\zeta}_{\perp}/\sin\alpha\right] && (5.42)\\
D_{55} &= (\zeta_{\parallel}R^3)\frac{1}{12}n\Big[n^2\tilde{P}^3\tilde{\zeta}_{\perp}\cos\alpha + 12\pi\tilde{\zeta}_{\perp}\sin\alpha\\
&+ \left((15+2n^2\pi^2) - (9-2n^2\pi^2)\tilde{\zeta}_{\perp}\right)\tilde{P}\cos\alpha\Big] && (5.43)\\
D_{66} &= (\zeta_{\parallel}R^3)\frac{1}{12}n\Big[n^2\tilde{P}^3\tilde{\zeta}_{\perp}\cos\alpha + 12\pi\tilde{\zeta}_{\perp}\sin\alpha\\
&+ \left((2n^2\pi^2-3) + (9+2n^2\pi^2)\tilde{\zeta}_{\perp}\right)\tilde{P}\cos\alpha\Big] && (5.44)\\
D_{46} &= -(\zeta_{\parallel}R^3)n\tilde{P}\chi\left[(\tilde{\zeta}_{\perp}-1)\sin\alpha - \tilde{\zeta}_{\perp}/\sin\alpha\right] && (5.45)\\
D_{14} &= -(\zeta_{\parallel}R^2)2\pi n\chi(\tilde{\zeta}_{\perp}-1)\cos(\alpha) && (5.46)\\
D_{25} &= (\zeta_{\parallel}R^2)\frac{3}{2}n\pi\chi(\tilde{\zeta}_{\perp}-1)\cos\alpha && (5.47)\\
D_{36} &= (\zeta_{\parallel}R^2)\frac{1}{2}n\pi\chi(\tilde{\zeta}_{\perp}-1)\cos\alpha && (5.48)\\
D_{16} &= -(\zeta_{\parallel}R^2)n\tilde{P}(\tilde{\zeta}_{\perp}-1)\cos\alpha && (5.49)\\
D_{34} &= 0 && (5.50)
\end{aligned}
$$

Where $\tilde{P} = P/R$ and $\tilde{\zeta}_{\perp} = \zeta_{\perp}/\zeta_{\parallel}$. The mobility matrix is the inverse of the resistance matrix. Our resistance matrix differs from that reported in Man and Lauga [41] since according to their Eq. 1 their origin is located at one end of the helix, while ours is located along the symmetry axis in the center of the helix. They also include contributions to the moment from local moment densities which resistive force theory ignores.

5.13 Appendix B: Quantitative calculation of mobility matrices

In most of the manuscript, we used resistive force theory with the ratio of perpendicular to parallel resistive force coefficients equal to two, which is the expected value in the limit of very slender helical filaments. As the filament radius (a) becomes thicker one can adjust resistive force coefficients; for helices, the following formulas apply [78]:

$$\zeta_{\parallel} = \frac{2\pi\mu}{\log(0.18P/a)} \tag{5.51}$$

$$\zeta_{\perp} = \frac{4\pi\mu}{\log(0.18P/a)+1/2}. \tag{5.52}$$

However, for the experimental geometries described below (*e.g.* $P = 0.91\,\mu$m, $a = 0.19\,\mu$m), these formulas yield negative $\zeta_{\parallel}$, implying that they are too thick to be adequately treated by resistive force theory.

To calculate quantitatively accurate mobility matrices, we used the method of regularized stokeslets [51, 52]. Our group has previously implemented the method [53], including to find mobility matrices for the modeling procedure employed in this paper [42, 46], and details of the method can be found in those references.

Here, we provide geometries and results of convergence studies for the helical microswimmers discussed in Section 5.7. We use these to provide estimates for the error in our calculations of velocity-frequency slopes.

The helical swimmer of Ghosh *et al.* [2] was modeled as a helix with $R = 0.16\mu$m, $P = 0.91\mu$m, 4 turns, and a filament diameter of 0.38μm, as shown in Fig. 5.10a. This geometry was obtained from Fig 1 of [2]. We performed a convergence study by discretizing the surface with varying number of regularized stokeslets (Fig. 5.11).

Figure 5.10: a) Geometry used to model helix of Ghosh *et al.* [2]. b) Geometry used to model helix of Peters *et al.* [3].

The results reported in the main text are for the largest number of elements, 12,134 regularized stokeslets, but we see that even for ≈ 6000 stokeslets there is $< 5\%$ error.

Based on the convergence study above, we can also investigate the accuracy of resistive force theory results for the velocity:frequency slope. In Fig. 5.12 we compare results from resistive force theory to the method of regularized stokeslets for the geometry above but for varying filament radius. The number of discretization elements for the method of regularized stokeslets varies from 6974 to 15544. For filament radii $a < 0.032\,\mu$m ($a/P < 0.035$), there is less than 5% difference between the resistive force theory and method of regularized stokeslets. For resistive force theory, the two largest filament radii plotted ($a = 0.128\,\mu$m and $a = 0.19\,\mu$m) give unphysical negative results, which reflect unphysical resistive force coefficients: Eqs. 5.51 and 5.52 give parallel coefficient *larger* than perpendicular coefficient for $a = 0.128\,\mu$m, and *negative* parallel coefficient for $a = 0.19\,\mu$m.

The helical ribbon of Peters *et al.* [3] was modeled as a helix with $R = 2.9\mu$m, $P = 16\mu$m, 3 turns, and a cross section with width 2.8μm and depth 1.5μm. The geometry is shown in Fig. 5.10b. This geometry was obtained from Fig. 1 of [3]. Based on the convergence study performed for the Ghosh *et al.* helix, the reported results are obtained from discretizations involving 5,832 regularized stokeslets, for which we expect discretization error of $\approx 5\%$. Finally, we note that we observed that changes in

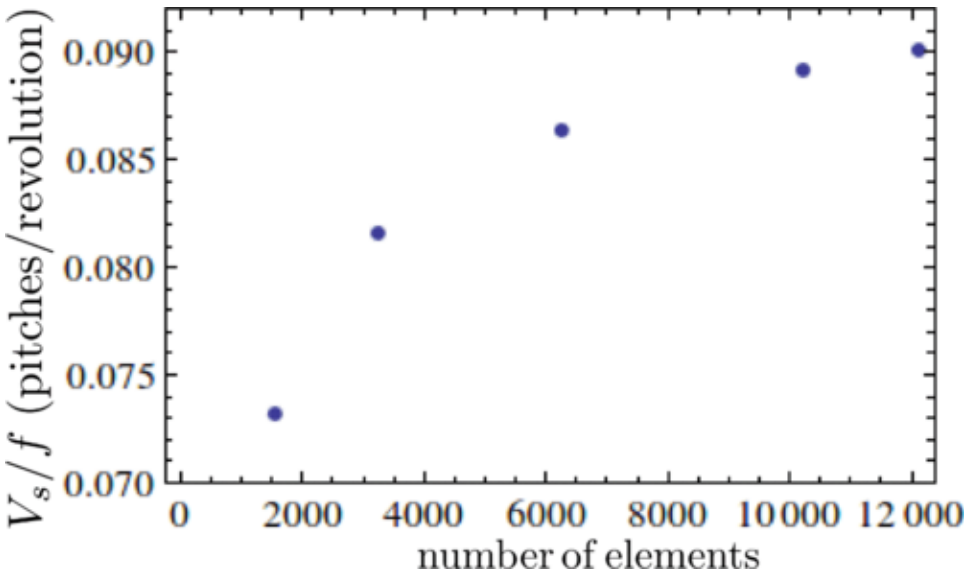

Figure 5.11: Convergence study for modeling helix from [2]: velocity-frequency slope as a function of number of regularized stokeslets used in discretization.

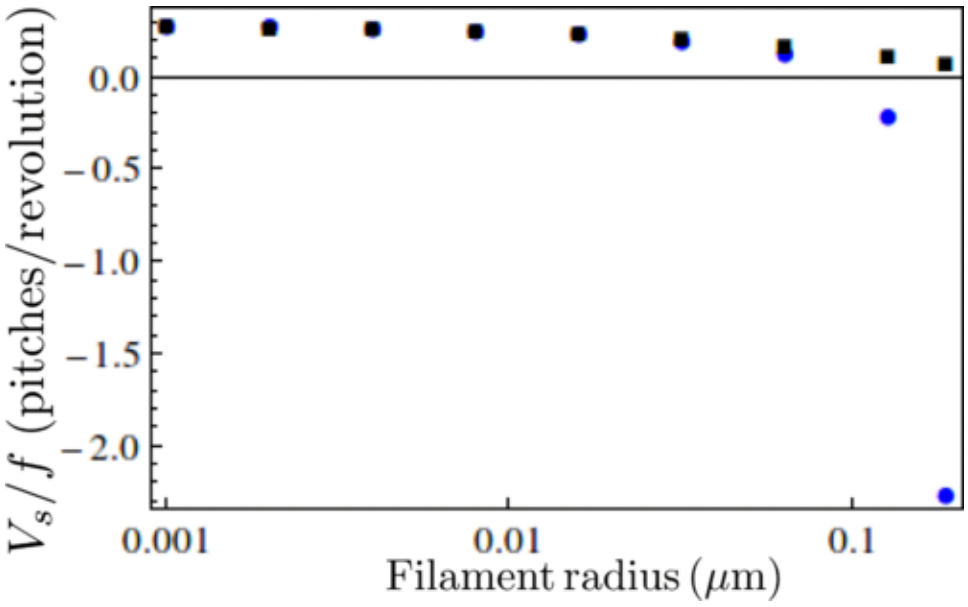

Figure 5.12: Comparison of velocity:frequency slopes calculated using resistive force theory (blue circles) and method of regularized stokeslets (blaack squares) as a function of filament thickness. The helix geometry is from [2], but with the filament radius a altered.

geometry, particularly in the length of the helix, could produce roughly proportional changes in the velocity-frequency slope. Additionally, changing the depth and width of the Peters *et al.* helix to 3.3 μm and 1.8 μm (10-20% changes) reduced the swimming speed by approximately 10%. Based on the imprecision of our measurements of experimental geometries which also do not form perfectly regular helices, we therefore expect an additional 5-10% errors in our results. Combining with the discretization error, we estimate (conservatively) that our calculated velocity-frequency slopes are accurate to within 15%.

Chapter 6

Versatile Microrobotics Using Simple Modular Subunits

6.1 Abstract

The realization of reconfigurable modular microrobots could aid drug delivery and microsurgery by allowing a single system to navigate diverse environments and perform multiple tasks. So far, microrobotic systems are limited by insufficient versatility; for instance, helical shapes commonly used for magnetic swimmers cannot effectively assemble and disassemble into different size and shapes. Here by using microswimmers with simple geometries constructed of spherical particles, we show how magnetohydrodynamics can be used to assemble and disassemble modular microrobots with different physical characteristics. We develop a mechanistic physical model that we use to improve assembly strategies. Furthermore, we experimentally demonstrate the feasibility of dynamically changing the physical properties of microswimmers through assembly and disassembly in a controlled fluidic environment. Finally, we show that different configurations have different swimming properties by examining swimming speed dependence on configuration size.

6.2 Introduction

Modular microrobotics are attractive since they may allow for much greater versatility, enabling a single system to navigate many different environments or perform multiple tasks, which are key hurdles for in vivo biomedical applications. While existing microrobots have demonstrated excellent capabilities to move or work in homogenous environments and to complete a single specific task, modular robots with the ability to change their shape can adapt to varying tasks and environments and can respond to unpredictable situations [81]. This is advantageous for applications that requires the use of micro/nanorobots over a wide range of different environments. Two illustrative examples are targeted/localized drug delivery and minimally invasive surgery.

For drug delivery, recent research in nanomedicine has shown great promise to improve mediated delivery to tumors via the use of nanoparticles [82], [83]. The success rate of using nanoparticle drug delivery methods depends on many uncontrolled factors in various vastly different environments such as circulation in the blood stream, diffusion inside tumor microenvironments, and biological barriers such as extracellular matrix (ECM) [84]. For example, in drug delivery the inability to overcome these environments can lead to poor drug accumulation on tumor cells [85]. Current approaches in nanoparticle drug delivery focus on using diffusive transport and targeting ligands, but there are also several studies using a microrobotics approach to enhance targeting by using magnetic field gradients for direct manipulation [11, 86, 87] which show the potential of using microrobotics in nanoparticle drug delivery. Nonetheless, the challenge of traversing many different environments remains formidable. Since microorganisms use a vast variety of shapes and propulsion methods to navigate many different bio-environments, reconfigurable microrobots that can take many different shapes and sizes could be useful to tackle the diversity of in vivo environments. For example, larger swimmers can move faster according to the Resistive Force Theory [88]

which is useful against adverse flow.

For microsurgery, recent developments in microrobotics have shown revolutionary potential to improve minimally invasive surgical procedures through highly controllable and precise manipulation, which bring intraoperative and postoperative benefits [5–13, 20, 36, 89–91]. Microrobots have been tailored to move and work in specific homogenous environments, as well as completing specific tasks such as on-surface transportation [14, 92, 93], tissue incision [57], puncture of retinal veins [7], and cell scaffolding [10]. However, a reconfigurable system which can travel through various environments and then change configurations to accomplish a variety of tasks would greatly advance microsurgery applications.

Although many types of microrobots have been successfully created, including flexible swimmers [19,65], biological robots [14,15], and chemical propellers [19,21,22,25], we focus on those actuated and controlled by magnetic fields, which is considered to be the most effective method since magnetic fields permeate over long ranges with minimal health effects and easily transmit large amounts of power [36,94]. The most common variety of magnetically-actuated microrobot are helical and chiral [60–63,95–97]. For modular microrobotics, Tottori et al. have previously introduced a method to assemble and disassemble helical microswimmers into different configurations using magnetic force and hydrodynamic interactions [40]. However, although their system could dynamically reconfigure size and shape, the underlying helical geometry, while effective for swimming, is not ideal for modularity as the maximum number of assembled swimmers is three, reducing versatility.

In contrast, the modular microrobots we use for this work utilize magnetic beads as the basic building blocks, allowing a much wider range of module and assembled geometries than helical microswimmers. Much like snake-like macroscale modular robots [81], microscale bead-based modules enable high versatility at low cost, and furthermore synergize well with the particulate drug delivery paradigm. Our modular

microswimmers consist of magnetic microbeads assembled by magnetic attraction. The use of particle-based modules is enabled by our previous work on achiral, particle-based microswimmers [42, 46, 74, 98] which showed that bodies constructed of more than 3 beads can swim. We demonstrate directed assembly of swimmers with other single- or multiple-bead modules, elucidate the physical mechanism of assembly, and use the mechanism to improve assembly efficiency, culminating in a demonstration of modular assembly and disassembly. Finally, to indicate how modular assembly can lead to swimmers capable of different behavior, we investigate how the swimming properties of assembled swimmers vary with size.

6.3 Results

6.3.1 Experimental observation of disassembly and assembly

We placed a sample of the microswimmers (structures with 3 or more beads) with nonmotile module units (single beads) inside a polydimethylsiloxane (PDMS) chamber ($3mm$ diameter, $2mm$ height). The chamber was sealed to prevent evaporation and to minimize flow, then placed inside approximate Helmholtz coils (see Methods Summary) for experiments. Our previous work showed that upon rotation by an external torque, magnetic structures constructed of three or more beads can be controllably propelled along the rotation axis. We propel swimmers constructed of magnetic microbeads ($4.35\mu m$ in diameter, Spherotech) towards additional beads or groups of beads for assembly.

In a representative example shown in Fig. 6.1(a) [also see Supplementary Movie 1], we observed a 7-bead swimming microswimmer rotating at $15Hz$ ($0-9s$) transformed into different shapes and size through disassembly and assembly. To disassemble the microswimmer, we increased the rotation frequency ($10-15s$). The hydrodynamic

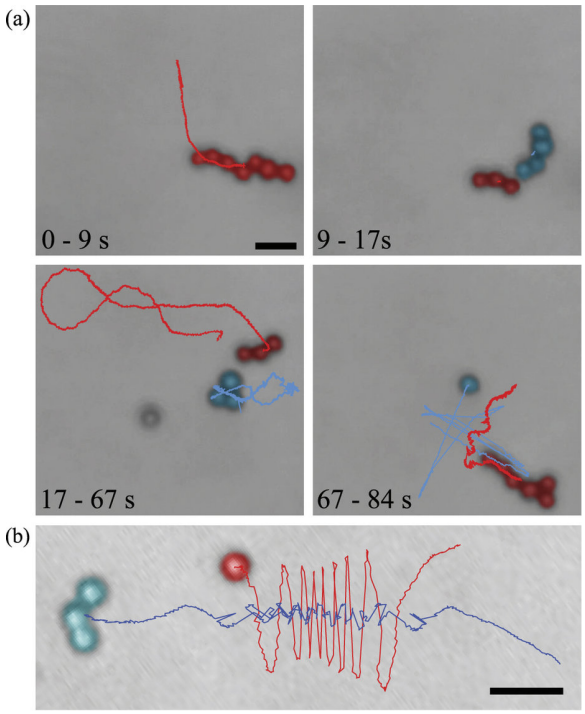

Figure 6.1: Assembly and disassembly for modular microrobotics.(a) Experimental demonstration of assembly and disassembly by manipulation of the control inputs (field strength and rotation frequency). (b) During a failure to assemble, the particles orbit around the microswimmer due to hydrodynamic force.

stress on the swimmer due to the high rotation frequency physically deformed the swimmer by creating a twisting effect [see Supplementary Movie 1] which led to disassembly at $16s$ when the swimmer broke into a 3-bead and 4-bead swimmer. The 3-bead swimmer demonstrated swimming at $15Hz$ rotation while the 4-bead structure remained stationary ($18-65s$). Cheang *et al.* provided a detailed explanation on why one structure can swim while the other does not [98]. At $65-70s$, the 3-bead swimmer then approached the 4-bead structure for assembly, however, one of the beads from the 4-bead structure detached, resulting in a final 6-bead assembled structure. From $71-84s$, the 6-bead swimmer demonstrated swimming at $15Hz$ rotation.

Not every approach leads to successful assembly. Figure 6.1(b) illustrates a single bead orbiting around an approaching microswimmer at $20Hz$ without mechanical

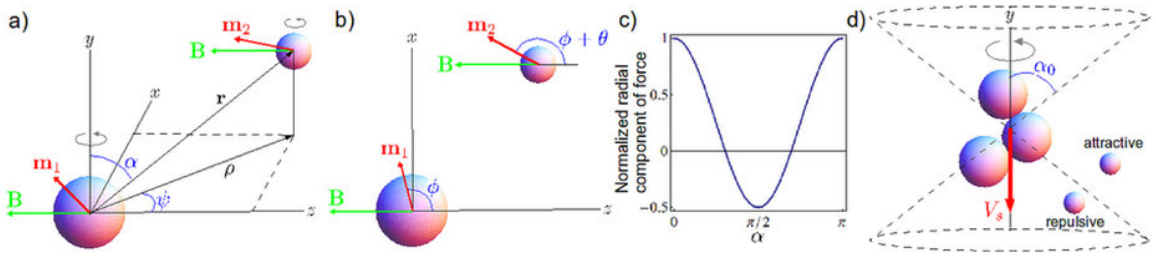

Figure 6.2: Schematic for assembly model. (a) Schematic for magnetic interaction between two magnetic beads with dipole $\mathbf{m}_{1,2}$ rotated by magnetic field $\mathbf{B}$. (b) Top view, showing lag angle θ. (c) Spatial dependence of normalized radial force on angle α describes (d) cones of repulsion in front and behind swimmer, and attractive region beside swimmer.

contact [see Supplementary Movie 2]. For the 3-bead microswimmers in this paper, most of the approaches at rotation rates higher than $20Hz$ resulted in failure.

6.3.2 Hydrodynamic and magnetic interactions for assembly

Although the observations above demonstrate assembly and disassembly, it is evident that the processes are not robustly controlled. To understand the mechanism of assembly and to improve its effectiveness, we developed a minimal physical model of the process.

We treat the magnetic interaction as the force between two spheres in a viscous fluid with permanent magnetic dipoles rotated by an external magnetic field (schematic in Fig. 6.2). The magnetic force between two dipoles with moments $\mathbf{m}_{1,2}$ separated by displacement $\mathbf{r}$ is

$$\mathbf{F} = \frac{3\mu_0}{4\pi r^4}\left[(\hat{\mathbf{r}} \times \mathbf{m}_1) \times \mathbf{m}_2 + (\hat{\mathbf{r}} \times \mathbf{m}_2) \times \mathbf{m}_1 - 2\hat{\mathbf{r}}\,(\mathbf{m}_1 \cdot \mathbf{m_2}) + 5\hat{\mathbf{r}}\,((\hat{\mathbf{r}} \times \mathbf{m}_1) \cdot (\hat{\mathbf{r}} \times \mathbf{m}_2))\right] \tag{6.1}$$

In the absence of interactions, each sphere rotates due to the external field. For rotation rates below step-out, each sphere will rotate at the same rate as the field with a fixed lag angle between each dipole and the field determined by equating the

magnetic torque ($\mathbf{m} \times \mathbf{B}$, where m is magnetic moment and B is magnetic field) and the rotational drag of the sphere ($8\pi\mu r^3 \boldsymbol{\omega}$). Therefore the lag angle θ in Fig. 6.2(b) is constant while ϕ steadily increases. Note that upon adding magnetic interaction between two rotating spheres, the rotation axis and dynamics are not strongly altered: dipole fields decay quickly with separation, and for the typical moments of our beads ($\approx 10^{-15} J/T$) dipole fields only approach the magnitude of our external fields ($\approx 1mT$) at distances $\ll 1\mu m$. Nonetheless, even small non zero radial attraction or repulsion (via equation (6.1)) can ultimately lead to approach and successful assembly.

Experimentally, it is observed that swimmers rotate quickly compared to changes in position; hence, it is appropriate to average the magnetic force over the angle ϕ. The result of such averaging is a radial component of magnetic force proportional to $\cos\theta\,(1 + 3\cos 2\alpha)\,/r^4$, where α is the angle between the displacement vector and rotation axis (Fig. 6.2(a)), which is also in the direction of average swimming. Since the difference in lag angles (θ) is always less than $\pi/2$, the radial component of the magnetic force (Fig. 6.2(c)) is positive or repulsive at small and large α (in front or behind the swimmer) and negative or attractive for α in a range around $\pi/2$ (towards the side of the swimmer). Thus, there are cones of repulsive magnetic force in front of and behind the swimmer and a zone of attraction beside the swimmer (Fig. 6.2(d)). This simplified magnetic model suggests that during assembly, as a swimmer swims towards a module, it is in the repulsive region ($\alpha < \alpha_0$) and gets pushed off axis. Only when the swimmer moves beside the module can the module get attracted to and assemble with the swimmer.

Turning towards hydrodynamic interactions, the simplest model of the hydrodynamics is to treat the module as advected by the swimmer's velocity field, so that it behaves as a Lagrangian tracer particle. To produce swimming, we model the swimmer as a rigid three-sphere assembly with a permanent magnetic dipole ($\mathbf{m}$).

We calculate the mobility matrix of the swimmer using the method of regularized Stokeslets [52]. The mobility matrix relates the instantaneous velocity and angular velocity to the external magnetic torque ($\mathbf{N} = \mathbf{m} \times \mathbf{B}$); for homogeneous fields there is no magnetic force on a dipole. As in our previous work, we find a steadily rotating solution to the dynamics when the angular velocity is equal to the rotation of the field, which requires a specific orientation of the swimmer relative to the rotation axis and magnetic field [42, 46]. Once the orientation of the swimmer is known, the total torque, linear velocity, and angular velocity of the swimmer are determined and hence the velocity field around the swimmer can be calculated from the method of regularized Stokeslets.

Without magnetic interactions, integrating the velocity field around a rotating swimmer yields the trajectory of a nonswimming module. To interpret trajectories, we compute a Poincare return map that reveals where a particle moves after one orbit around the swimmer (Fig. 6.3(a)). The map takes a point on the horizontal plane in the swimmer frame which contains the rotation axis, and maps it to the second intersection of its trajectory with the plane, *i.e.*, its position after a full orbit around the swimmer. Examining the map of all points of the plane (Fig. 6.3(b)) yields insight into the dynamics; for example, long-term behavior of particles can be deduced from repeated applications of the map. Notably, without magnetic interactions, there is no strong tendency towards attraction or repulsion; rather particles get advected past the swimmer (upwards in the Fig. 6.3) due to the swimming flow.

Magnetic and hydrodynamic interactions can be combined by altering the instantaneous velocity of the module in the above by the Stokes drag velocity $\mathbf{v} = \mathbf{F}/(6\pi\mu\alpha_2)$ resulting from the magnetic interaction force, which alters the time-integrated trajectories and hence Poincare return map (see Fig. 6.3(c) for an example). With the addition of magnetic interactions, the Poincare map reveals that (1) there is a stagnation region in front of (below in the Fig. 6.3) the swimmer mag-

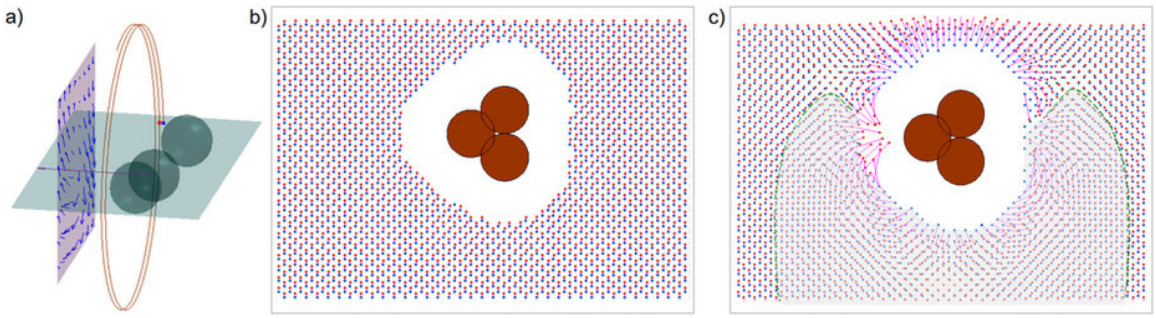

Figure 6.3: Poincare return map. (a) Velocity field on one vertical plane and lagrangian particle trajectory in swimmer frame. Poincare return map reveals movement of bead after one orbit around swimmer, mapping an initial position on horizontal plane (blue point) to the second intersection of its trajectory with the plane (red point). (b) Poincare return map of lagrangian particle trajectories for swimmer moving downwards. Initial positions (blue) are mapped to final positions (red). (c) Poincare return map when magnetic interactions are included. The shaded area is the area of attraction for particles in front of swimmer.

netic repulsion pushes the module away, leading to difficulty in approach; and (2) all particles in an attraction zone surrounding the front and sides of the swimmer (shaded and delineated by dashed line in Fig. 6.3) eventually move towards the side of the swimmer as a result of cumulative magnetic forces, even if they are initially repelled in front of the swimmer.

We used the model to improve the success rate of approaching modules for assembly. The model predicts an attractive zone in front of and beside the swimmer. Assembly will only occur if the swimmer can be steered such that the module enters the attractive zone. One method to place the module in the attractive zone is to steer the swimmer so that the module is in front of the swimmer and then swim towards the module. This method requires a relatively small approach angle α. Previously, we steered the swimmer to approach the module head-on. The model suggests that head-on approach may be slower due to the stagnation region; instead, a slightly off-center approach may be better. In addition, the model determines how far off-center the approach can be: the range of allowable module placements can be quantified

by the width of the attraction region at the bottom of Fig. 6.3(c), which we call Δx. We varied the frequency of rotation in our model to investigate the frequency-dependence of the size of the attraction region and Δx. Although there was not a one-to-one correlation due to the fact that the rotation axis of the swimmer changes as frequency changes [52], in general increasing the frequency decreased both the size of the attraction region and Δx. A second method of assembly is, instead of steering so that the module approaches at a small approach angle, to swim near the module, and then turn suddenly by a large angle so that the module is beside the swimmer, *i.e.* the module enters the side lobes of the attraction region.

6.3.3 Qualitative investigation of assembly

We performed a set of experiments (Fig. 6.4) to corroborate the predictions of our physical model for assembly and to improve the assembly process. During approach to a single bead, we measured the angle α between the swimmer rotation axis and the displacement vector $\mathbf{r}$ from the swimmer centroid to the approached bead. Due to 2D images from the recorded videos, we were restricted to measuring α and $\mathbf{r}$ once per rotation, when the particle and the swimmer lie in the focal plane. First, we note that in each of these and other observations, during approach the particle orbits around the swimmer as predicted from the velocity fields calculated in our model. Second, we verified the existence of an attractive region. In Fig. 6.4(a-c), we show pairs of approaches at similar frequencies; in each pair there is one unsuccessful approach and one successful approach. As predicted, for each pair the successful approach starts with smaller α, placing the module in the attractive width Δx, while the unsuccessful approach has larger α. Third, the frequency dependence of the size of the attraction zone can be seen by comparing Fig. 6.4(a-c): for Fig. 6.4(a), the width of the attraction zone is between $\alpha = 33.4^\circ$ (successful) and $\alpha = 66^\circ$ (unsuccessful)

for $45Hz$ rotation, while at the higher frequencies the width of the attraction zone is between $\alpha = 11.3°$ (successful) and $\alpha = 26.2°$ (unsuccessful) for $10Hz$ rotation, or $\alpha = 14.5°$ (successful) and $\alpha = 73°$ (unsuccessful) for $1025Hz$ rotation. In addition, in Fig. 6.4(b), there are much smaller orbital distances for the unsuccessful approach than in the unsuccessful approach in Fig. 6.4(a) as the particle passes the swimmer. All of this evidence supports the prediction that increasing the rotation frequency decreases the size of the attractive zone. Fourth, in the initial portions of Fig. 6.4(d), we show how a head on approach at very small α can be disadvantageous due to the stagnation region predicted by the model. For top case in Fig. 6.4(d), the microswimmers approached the modules at $\alpha = 17.9°$ resulting in the particle being trapped inside the stagnation region; as a result, α decreased to 7.5° and $\mathbf{r}$ plateaued at $5\mu m$ until $6.1s$. The same phenomena was observed for the bottom case in Fig. 6.4(d) where the microswimmers approached the modules at $\alpha = 2°$ and $\mathbf{r}$ plateaued at $9\mu m$ until 20.8 s. Fifth, starting from the head-on configurations in Fig. 6.4(d), we demonstrate the second method of assembly suggested by our model: we were able to trigger assembly by a change of ($34.1°$ at $8.2s$, top; $\alpha = 38.9°$ at $30.4s$, bottom) placing the module beside the swimmer rather than in front of it. To summarize, we found that slower frequencies and small (but not exactly head-on) approach angles were efficient assembly strategies.

6.3.4 Demonstration of modular microrobotics

Finally we describe a representative experiment showing the extent of modular capabilities by starting with a microswimmer with minimal number of beads (3 beads) and modulating into a nine-bead swimmer. In accord with the assembly strategy discussed above, at each of the stages involving assembly, the rotation of the microswimmer was decreased in order to promote magnetic assembly. Figure 6.5 is a collage of the exper-

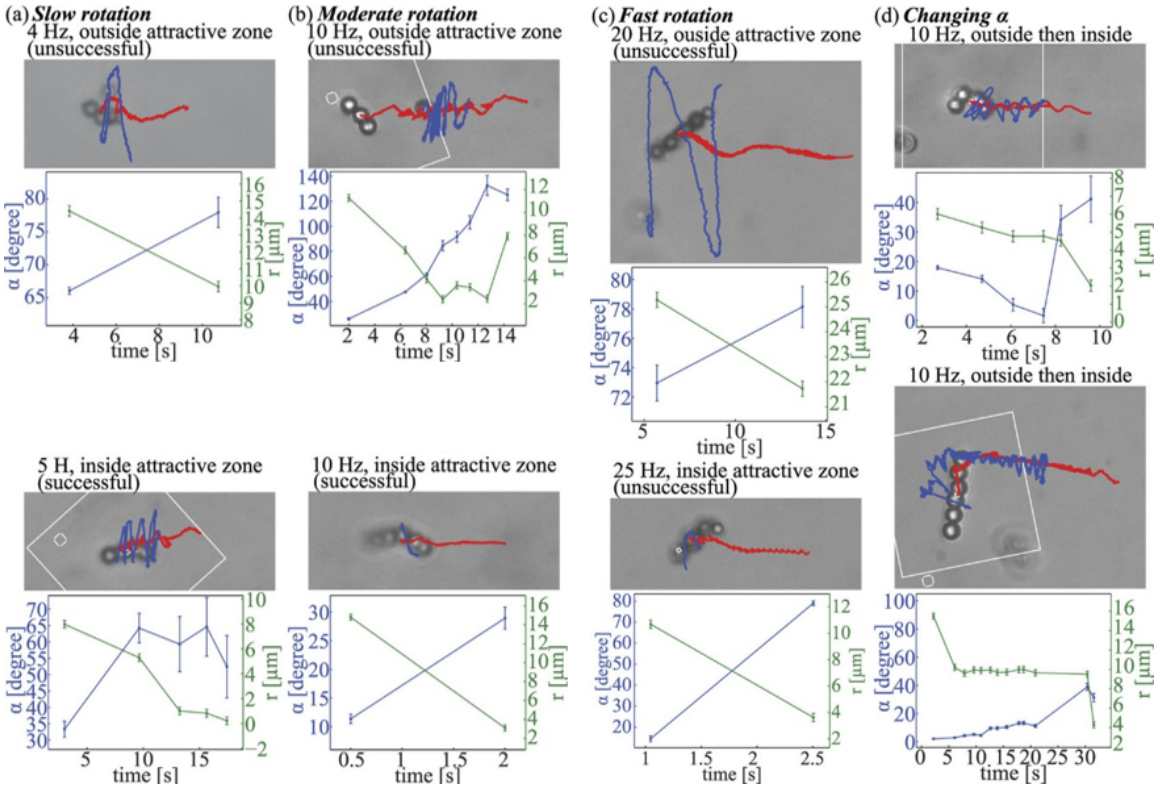

Figure 6.4: (a) Assembly under low rotation rate ($45Hz$). The large attractive zone as a result of the slow rotation yields unsuccessful assembly when the orbital distance is very large (top) and successful assembly when the orbital distance is smaller (bottom). (b) Assembly under moderate rotation rate ($10Hz$). The small attractive zone as a result of the increased rotation rate yields unsuccessful assembly when the orbital distance is very small (top) and successful assembly when the swimmer approaches the single bead at a very small α (bottom). (c) Assembly under fast rotation rate ($2025Hz$). The attractive zone becomes very small due of the fast rotation rate which results in the single particle being repelled radial causing a very large orbital distance and failure of assembly (top). Successful assembly was possible when the swimmer approach the single bead at a very small α, similar to (b) (bottom). (d) Initial α was small resulting in very small orbital distances and trapping in magnetohydrodynamic stagnation region in front of swimmer. When α was increased by steering the swimmer to different direction, assembly became possible.

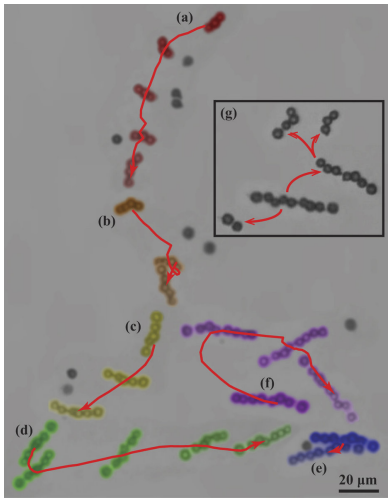

Figure 6.5: Representative experiment of a modular microrobot.From (a), a 3-bead robotic microswimmer approaches and assemble with a single non-motile bead and transform into a 4-bead microswimmer. From (bf), the microswimmer continues to approach and combine with single beads, and eventually modulate into a 9-bead microswimmer. At (g), the 9-bead microswimmer breaks into three different microswimmers under high rotation frequency due to increased shear stress leading to structural flexing.

iment showing 7 stages [see Supplementary Movie 3]. At stage 1, the microswimmer started as a 3-bead microswimmer and assembled with a single non-motile bead to become a 4-bead microswimmer. Likewise from stage 2 to 6, the microswimmer continued to assemble with nearby single beads until it formed a 9-bead microswimmer. At stage 7, a high rotation frequency was introduced which sequentially breaks the microswimmer into three entities: a 2-bead structure, a 3-bead microswimmer, and a 4-beads microswimmer. The 3-bead and 4-bead microswimmers swim controllably, whereas the movement of the 2-bead is not controlled hence we speculate to be driven by neighboring flow fields.

6.3.5 Assembled swimmers of various sizes have varying swimming behavior

Modular microrobotics is most useful if swimmers of different geometries can be constructed with varying abilities to navigate diverse environments or to perform diverse tasks. We have demonstrated modular assembly and disassembly, but our modular microrobotic system has not been optimized for accomplishing such diverse tasks. However, to suggest the potential of a modular approach, we investigate whether the swimmers of different sizes that we create through our modular microrobotics display different behavior. The particle based microswimmers have different configurations which we refer to as 3-bead, 4-bead, 5-bead, etc. While the minimal geometry requirement for low Reynolds number swimming is three beads [46], microswimmers with more than three beads also demonstrated swimming capability. Usually, dipole-dipole interactions lead to linear assembly [99], but in the context of our modular system, nonlinear geometries can easily be generated, as seen in Fig. 6.6, which shows representative examples of three, eight, and thirteen bead microswimmers. This is in fact advantageous since perfectly straight structures cannot generate propulsion upon rotation. To show that different modular configurations have different swimming characteristics, we statistically measured the swimming speed of microswimmers with different body lengths. Microswimmers with more beads tend to swim faster, as shown in Fig. 6.6. Data for each configuration from Fig. 6.6 was taken from multiple microswimmers; the three bead swimmers rotating at $6Hz$ have an average velocity of $2.53 \pm 0.56 \mu m/s$ and the eleven bead swimmers have an average velocity of $17.85 \pm 1.51 \mu m/s$ (see Supplementary Movie 4). The standard deviations are generally larger for microswimmers with more beads due to geometrical reasons, since each additional bead adds to geometrical variability.

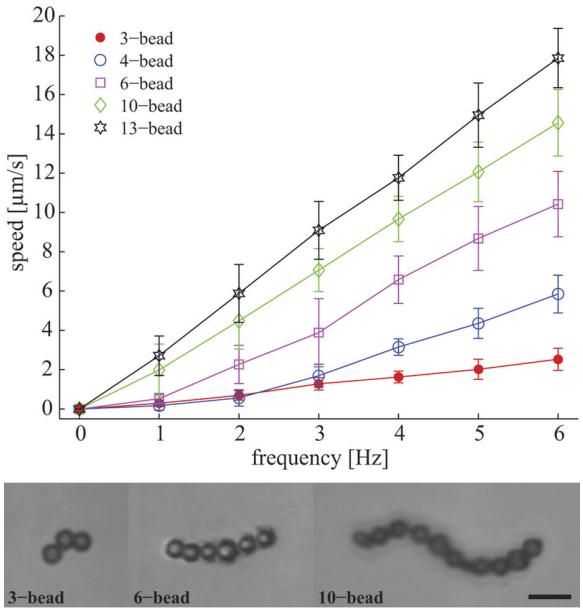

Figure 6.6: Characterization of swimming capability for microswimmer at various lengths. Swimming speed plotted as a function of rotation frequency for magnetic swimmers with different number of beads. This highlights the increase in swimming power as the size and aspect ratio of the swimmers increase.

6.4 Discussion and conclusions

We have demonstrated that magnetic microbeads can be used as modular units to create dynamically reconfigurable microswimmers. Versatile modularity is enabled by the ability of generic geometries to be propelled by a rotating magnetic field. Both assembly and disassembly can be achieved. We developed a mechanistic physical model incorporating magnetic and hydrodynamic interactions to understand the assembly process, and used it to find improved assembly strategies, enabling controlled assembly from 3-bead to 9-bead microrobotic systems. Finally, we showed that different configurations have different swimming properties. While we investigated how swimming speed depends on the number of beads in assembled swimmers, for the applications of drug delivery and minimally invasive microsurgery future work remains to demonstrate that different assembled configurations can achieve navigation

through various *in vivo* environments, and can be constructed to accomplish different tasks during operative procedures. We believe that the mechanistic insight into the assembly process we discussed in the manuscript will greatly aid future efforts at developing configurations capable of achieving these crucial abilities.

6.5 Methods

6.5.1 Magnetic control system

To generate the rotating magnetic field which actuates the achiral microswimmers, we used a control system consisting of three pairs of electromagnetic coils arranged in an approximate Helmholtz configuration, three Kepco power supplies (BOP 205M), a National Instruments data acquisition (DAQ) system, a computer, an inverted microscope (Leica DM IRB), and a high speed camera (FASTCAM SA3). Through the use of a DAQ system, the power supplies generate sinusoidal outputs to the coils to create a rotating magnetic field. The high speed camera provides visual feedback and records videos at high frame rates ($60100 fps$). The computer is used as interface for the camera and the DAQ system. The three pairs of coils are designed to exert torque on the swimmer without introducing translational force by creating a spatially uniform magnetic field with any specified time-dependent magnitude and direction in a $2mm \times 2mm \times 2mm$ region. Experiments take place with swimmers immersed in distilled water (viscosity of $1 mPa \cdot s$) in a $3mm \times 3mm \times 2mm$ ($L \times W \times H$) polydimethylsiloxane (PDMS) chamber, sealed to minimize fluid flow and evaporation, and placed at the center of the Helmholtz coil system mounted on the microscope.

The coil system is designed to exert constant torque on the microswimmer without introducing translational force. The coils are arranged in a slightly different configu-

ration than that of the normal Helmholtz coil. Conventionally, Helmholtz coil restrict the distance between two coils of the same size to be the radius of the coils. Given the space constraint of our microscope, our configuration was designed to optimize the magnetic field profile in order to create a near constant region at the center of the coils. In this study, the distance between the coils is equal to the outer diameter of the coils plus the thickness for the coil, creating a cube-like configuration for the 3D coil system.

Computer simulation and direct measurements from a tesla meter were used to model the magnetic field generated from the 3D coil system. With 1 Amp of current passing through two pairs of coils, the simulation result yielded a value of $5.06mT$ at the center of the field, which matches the experimentally measured value of approximately $5mT$. We also investigated the field profile and demonstrated the ability of the coil system to generate a near-constant magnetic field at the center region approximately within a $2mm$ diameter. The size of this region approximately matches the size of the area where experiments take place. Given the size of the microswimmers being tested, the $2mm$ region provides sufficient space needed for experimentation.

6.5.2 Steering microswimmers using magnetic fields

The magnetic field strength (mT), rotational direction of the magnetic bead (CW or CCW), and rotational frequency (Hz) of the field generated by the coils can be controlled through LabVIEW. The effective magnetic field ($\mathbf{B}$) is the vector resultant of the $x-$, $y-$, and $z-$components. To create a rotation, there must be at least two pairs of electromagnetic coils; for example, one pair in the y direction and one pair in the z direction create a rotating field in the $yz-$plane. The two pairs generate sinusoidal outputs with 90° phase lag. Using $xy-$ planar control, the resultant field

can be expressed as [74]

$$\mathbf{B} = B_0 \begin{bmatrix} \sin\theta \sin(\omega t + \phi)\,\hat{\mathbf{i}} \\ \cos\theta \sin(\omega t + \phi)\,\hat{\mathbf{j}} \\ \cos(\omega t + \phi)\,\hat{\mathbf{k}} \end{bmatrix} \tag{6.2}$$

which rotates with angular velocity ω around the unit vector

$$\mathbf{n} = \begin{bmatrix} -\cos\theta \\ \sin\theta \\ 0 \end{bmatrix} \tag{6.3}$$

where B_0 is the maximum amplitudes of the magnetic field generated by the x, y, and z pair coils respectively, ω is the rotational frequency of the field, ϕ is the phase, θ is the direction of rotation, and is time. By controlling the field strength of x, y, and z components and the frequency; the frequency of the microswimmers rotation and the corresponding mode of motion can be fully controlled.

6.5.3 Tracking algorithm

A MATLAB tracking algorithm was used for the analysis of the microswimmers trajectories. Data taken from experiment are avi video files which can be decompressed in MATLAB and analyzed frame by frame. For each frame, the algorithm processes the image using four main steps: image binarization using grayscale thresholding, structure definition based on pixel continuity, size thresholding to filter out unwanted pixels, and calculation of geometrical centroid. First, in image binarization, a threshold defines a grayscale cutoff value for each pixel and converts the image to binary (black/white). Afterward, the interior of the microswimmer is filled and sequentially

labelled as 1, 2, 3, etc. Next, unwanted objects such as debris or out of focus particles are removed using size thresholding which filters out objects bigger and smaller than the microswimmer. At this stage, the only remaining object is the microswimmer and the size of the microswimmer is defined as the number of pixel they occupied. Finally, the geometrical centroid (x, y) is calculated.

Chapter 7

Soft-Magnetic Swimmers

7.1 Introduction

The models discussed so far focus on hard magnets: ferromagnets with permanent magnetization. The soft-magnetic materials, on the other hand, do not preserve their magnetization upon the removal of the external magnetic field. As we discussed in chapter 2, soft magnets possess lower coercivity and in many cases, lower remanence relative to hard magnets. Figure 7.1 indicates this prominent difference between hard and soft magnets. There are a number of studies that proposed models for permanent magnets [2, 41–43] and paramagnets [2]. In 2007, Abbott *et al.* provided models for magnetic force and torque of soft-magnetic bodies [100]; however, to this date, no model has been reported for soft-magnetic microswimmers. In this chapter, we develop a model for swimmers that are fabricated from soft magnetic material in saturation regime based on the torque equations derived by Abbott *et al.* [100].To present our model, we assume a swimmer comprising of a prolate ellipsoidal head made from a soft ferromagnetic material and a nonmagnetic helical tail. the magnetic head is assumed to be polycrystalline with many randomly oriented grains, neglecting the magnetocrystalline anisotropy. Hence, the shape anisotropy is the only plausible

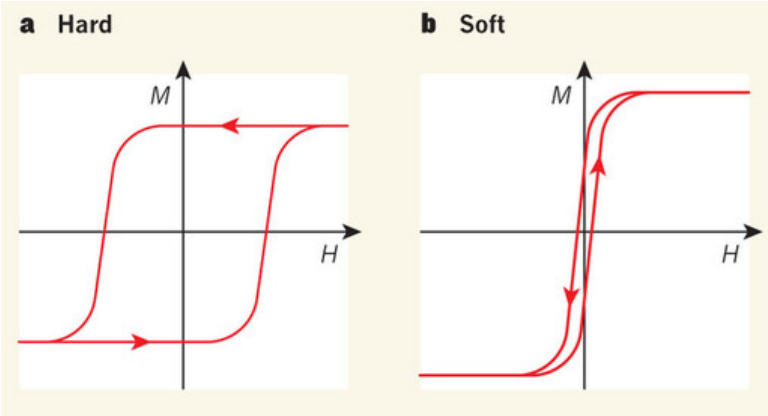

Figure 7.1: Typical hysteresis loops for hard (a) and soft (b) magnets. Hard magnets require higher magnetic fields to reach saturation, but they preserve most of their magnetization upon field removal, resulting in a permanent magnet. Soft magnets are more easily saturated, but magnetization drops significantly as the applied field decreases. Figure from [4].

anisotropy.

7.2 Methods

Figure 7.2 shows the schematic of the ellipsoidal head in the body frame. The $\mathbf{e}_1$ direction is the axis of symmetry of the ellipsoid. The directions of the magnetization and magnetic field are specified using two sets of azimuthal and altitudinal angles (θ_M, ϕ) and (θ_H, ϕ) respectively. Note that due to symmetry, $\mathbf{H}$, $\boldsymbol{\mathcal{M}}$ and $\mathbf{e}_1$ are coplanar.

The total energy of the system is the sum of the energy due to the shape anisotropy (e_a), eq. 2.20 and the potential energy (e_p), eq. 2.4. So the total energy is:

$$e = e_a + e_p = \frac{1}{2}\mu_0 V \left(n_r - n_a\right) \mathcal{M}_s^2 \sin^2\theta_M - \mu_0 V \mathcal{M}_s H \cos\left(\theta_H - \theta_M\right), \tag{7.1}$$

where n_a and n_r are the demagnetizing factors in the axial $(\mathbf{e}_1)$ and radial directions, respectively. $\mathcal{M}_s$ is the saturation magnetization and H is the field strength. For

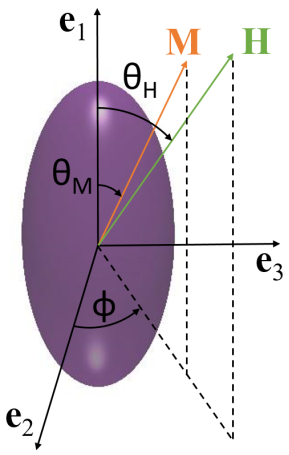

Figure 7.2: Schematic of the ellipsoidal head, coordinate system, magnetization and magnetic field.the **1** direction in chosen along the symmetry axis of the ellipsoid. Two sets of altitudinal and azimuthal angles, (θ_H, ϕ) and (θ_M, ϕ), are used to specify the directions of $\mathbf{H}$ and $\boldsymbol{\mathcal{M}}$ respectively.

a prolate ellipsoid such as the one in figure 7.2, the demagnetizing factors can be calculated from eq. 2.12. Assuming spontaneous dynamics of magnetic moment, we can establish a relationship between the orientations of $\mathcal{M}_s$ and H by minimizing the total energy with respect to θ_M.

$$(n_r - n_a)\,\mathcal{M}_s \sin(2\theta_M) = 2H \sin(\theta_H - \theta_M). \tag{7.2}$$

Equation 7.2 sets a relationship between allowable directions of $\mathbf{H}$ and $\boldsymbol{\mathcal{M}}$ in saturation regime.

The magnetic torque is associated with the changes in the states of energy, which correspond to different orientations of $\mathbf{H}$ in the swimmer's frame. To find the torque, let's assume that $\boldsymbol{\mathcal{M}}$ and $\mathbf{H}$ are on the $1-3$ plane without loss of generality. Any rotation about $\mathbf{e}_2$ changes θ_M so there is a component of torque along $\mathbf{e}_2$. To find this component, the total energy 7.1 needs to be differentiated with respect to θ_H. Using

chain rule, we get:

$$T_2 = \frac{\partial e}{\partial \theta_H} = \frac{\partial e_a}{\partial \theta_M^*}\frac{\partial \theta_M^*}{\partial \theta_H} + \frac{\partial e_p}{\partial \theta_M^*}\frac{\partial \theta_M^*}{\partial \theta_H} + \frac{\partial e_p}{\partial \theta_H} \tag{7.3}$$

where θ_M^* is the angle that minimizes the energy and is found from eq. 7.2. Note that the first two terms on the right-hand-side of eq. 7.3 vanish since $\frac{\partial e}{\partial \theta_M} = 0$. Hence the torque in $\mathbf{e}_2$ direction is

$$T_2 = \frac{\partial e_p}{\partial \theta_H} = \mu_0 V \mathcal{M}_s H \sin\left(\theta_H - \theta_M\right). \tag{7.4}$$

Any rotation about the $\mathbf{e}_1$ axis does not change the state of the energy since θ_H remains unchanged. Hence, component of toque along $\mathbf{e}_1$ is zero. We can show that the component of the torque along $\mathbf{e}_3$ is zero as well. In this case $\hat{\mathbf{H}} = (\cos\theta_H, 0, \sin\theta_H)$. If we rotate the geometry by angle α about $\mathbf{e}_3$ the new symmetry axis will be at $\mathbf{e}_1' = (\cos\alpha, \sin\alpha, 0)$ and the new altitudinal angle will be:

$$\theta_H' = \arccos\left(\hat{\mathbf{H}} \cdot \mathbf{e}_1'\right) = \arccos\left(\cos\theta_H \cos\alpha\right). \tag{7.5}$$

Then we investigate the change of θ_H' due to the rotation.

$$\left.\frac{\partial \theta_H'}{\partial \alpha}\right|_{\alpha=0} = \left(\frac{1}{\sqrt{1-\left(\cos\theta_H\cos\alpha\right)^2}}\cos\theta_H \sin\alpha\right)_{\alpha=0} = 0. \tag{7.6}$$

Hence, θ_H remains unchanged through this rotation and there is no torque along $\mathbf{e}_3$. This shows that the total torque is in $\mathbf{e}_2$ direction with the magnitude given by eq. 7.4. Therefore, the total magnetic torque in general form is precisely:

$$\mathbf{T} = \mu_0 V \left(\boldsymbol{\mathcal{M}}_s \times \mathbf{H}\right). \tag{7.7}$$

It follows from eq. 7.2 and eq. 7.7 that:

$$\mathbf{T} = \frac{\mu_0 V |n_r - n_a|}{2} \mathcal{M}_s^2 \sin(2\theta_M) \begin{pmatrix} 0 \\ -\sin\phi \\ \cos\phi \end{pmatrix}. \tag{7.8}$$

Then the angular velocity is given by

$$\mathbf{\Omega} = \mathbf{M}\mathbf{T} = \frac{\mu_0 V |n_r - n_a|}{2} \mathcal{M}_s^2 \sin(2\theta_M) \begin{pmatrix} -M_{12}\sin\phi + M_{13}\cos\phi \\ -M_{22}\sin\phi + M_{23}\cos\phi \\ -M_{32}\sin\phi + M_{33}\cos\phi \end{pmatrix}, \tag{7.9}$$

where $\mathbf{M}$ is the submatrix of mobility matrix that correlates the torque to angular velocity.

Assuming that the applied magnetic field is perpendicular to its axis of rotation, the solutions should satisfy $\mathbf{\Omega} \cdot \hat{\mathbf{H}} = 0$, where $\hat{\mathbf{H}} = \cos\theta_H \, \mathbf{e}_1 + \sin\theta_H \cos\phi \, \mathbf{e}_2 + \sin\theta_H \sin\phi \, \mathbf{e}_3$. The only nontrivial solution to this equation is:

$$\theta_H = \arctan \frac{M_{13}\cos\phi - M_{12}\sin\phi}{-M_{23}\cos 2\phi - (M_{33} - M_{22})\cos\phi\sin\phi}. \tag{7.10}$$

Equation 7.10 imposes a constraint on the allowable direction of the magnetic field and can be used to find θ_H. Moreover, in steady state, we can set a constraint on the direction of the magnetization by matching the magnitude of the angular velocity

from Eq. 7.9 with the experimental rotation rate of the magnetic field ω. It yields:

$$\theta_M = \begin{cases} \frac{1}{2}\arcsin A \\ \pi - \frac{1}{2}\arcsin A \\ \frac{\pi}{2} + \frac{1}{2}\arcsin A \\ \frac{\pi}{2} - \frac{1}{2}\arcsin A \end{cases}, \tag{7.11}$$

where

$$A = \frac{2\omega}{\mathcal{M}_s^2 \mu_0 |n_a - n_r| V} \frac{1}{\sqrt{\begin{array}{c} (M_{13}\cos\phi - M_{12}\sin\phi)^2 + (M_{23}\cos\phi - M_{22}\sin\phi)^2 \\ + (M_{33}\cos\phi - M_{23}\sin\phi)^2 \end{array}}}. \tag{7.12}$$

We can use Eq. 7.11 to find θ_M.

Equations 7.2, 7.10 and 7.11 establish a determined system from which we can numerically solve for θ_H, θ_M and ϕ. Once the $\mathbf{H}$ and $\boldsymbol{\mathcal{M}}$ are determined, the angular and linear velocities can be calculated.

The stability of solutions can be investigated using a method similar to what we discussed in [42]. The steady-state solutions are perturbed using an infinitesimal vector, $\boldsymbol{\sigma}$. The main difference between the stability analysis of soft magnets and hard magnets is that in the hard magnet case, the perturbed magnetization is not simply a rotation of the original magnetization by $\boldsymbol{\sigma}$. The new magnetization in the swimmer's basis is

$$\boldsymbol{\mathcal{M}}'^s = \boldsymbol{\mathcal{M}}^s + \mathbf{D} \cdot \Delta\mathbf{H}, \tag{7.13}$$

where $\mathbf{D} = \frac{\partial \boldsymbol{\mathcal{M}}^s}{\partial \mathbf{H}^s}$ and $\Delta\mathbf{H} = -\boldsymbol{\sigma} \times \mathbf{H}$. In these equations, the superscript s refers to the values in swimmer's basis. Tensor $\mathbf{D}$ is calculated using the chain rule from Eq.

7.2. Hence, the rate of change of $\boldsymbol{\sigma}$ with time can be formulated as:

$$\begin{aligned}\frac{\mathsf{d}\sigma_i}{\mathsf{d}t} &= (\epsilon_{ijk}D_{jl}\epsilon_{lmn}H_mH_k + M_{ij}\epsilon_{jkl}\mathcal{M}_k\epsilon_{lmn}H_m - \epsilon_{ijn}M_{jk}\epsilon_{klm}\mathcal{M}_lH_m) \\ &\equiv Q_{in}\sigma_n. \end{aligned} \tag{7.14}$$

Solutions are stable when all eigenvalues of $\mathbf{Q}$ have negative real parts. Note that in this work, we are not reporting the stability of solutions since our stability analysis is still in the verification stage.

We use *Buckingham-π* theorem to find the dimensionless groups. The dimensionless groups involved are: $|n_r - n_a|$, the dimensionless angular velocity $\tilde{\Omega} = \frac{\eta}{\mathcal{M}_s^2\mu_0}\Omega$ which can also be interpreted as the ratio of viscous torque to anisotropy torque, dimensionless magnetic field $\tilde{H} = \frac{H}{\mathcal{M}_s}$ and the dimensionless velocity $\tilde{v} = \frac{\eta}{\mu_0\mathcal{M}_sL}v$. In these equations, η is the viscosity of the fluid and L is the characteristic length of the swimmer, which we choose to be the total length of the swimmer.

Abbott *et al.* [100] explain the criterion for establishment of the saturation regime as:

$$H_s = \frac{\mathcal{M}_s n_a n_r}{\sqrt{n_a^2 \sin^2\theta_H + n_r^2\cos^2\theta_H}}. \tag{7.15}$$

For a prolate ellipsoid, $n_r > n_a$; therefore, the maximum and minimum of Eq. 7.15 correspond to $\tilde{H}_s = n_r$ and $\tilde{H}_s = n_a$, occurring at $\theta_H = \pi/2$ and $\theta_H = 0$, respectively. It is clear that for $\tilde{H} < n_a$ the material cannot be saturated for any direction of the field and therefore, the presented model is not valid. The present model is always valid for $\tilde{H} \geq n_r$ since it guarantees saturation for any direction of the magnetic field. When $n_a \leq \tilde{H} < n_r$, solution is not always guaranteed since the material will be saturated only for certain direction of the applied field. Therefore, for this range of field strengths, solutions are valid only for frequencies that result in directions of the magnetic field that correspond to a saturation scenario.

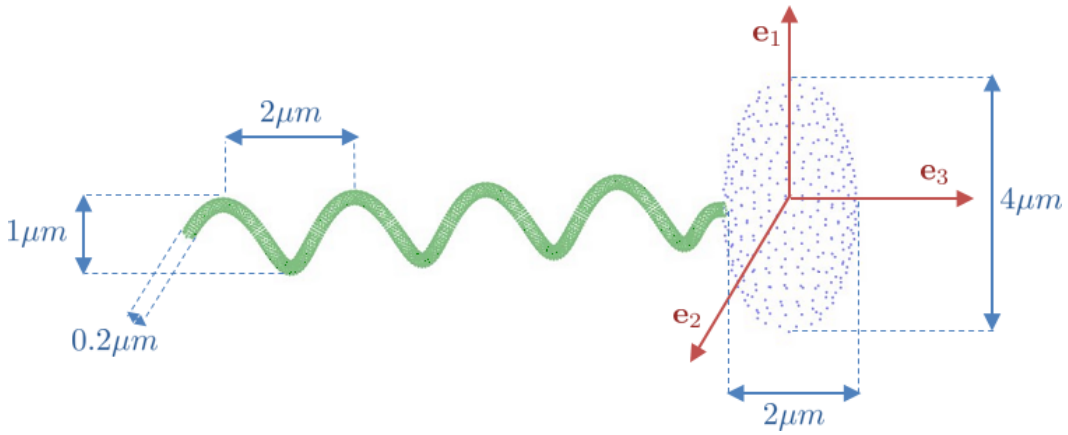

Figure 7.3: geometry used for the analysis. The ellipsoidal head has a semi-major axis of $a = 2\mu m$ and a semi-minor axis of $b = 1\mu m$. The head is discretized using 313 collocation points. The tail consists of a ellipsoid which is tapered where it connects to the head and a spherical cap at the free end. The tail is discretized by 3479 collocation points. The helix has a radius of $R = 0.5\mu m$, filament radius of $r = 0.1\mu m$ and axial pitch of $2\mu m$, and it consists of $n = 4$ total turns.

7.3 Results and discussion

To illustrate the behavior of saturated soft-magnetic swimmers, we compare a swimmer of this type with a swimmer made from permanent magnetic material of identical geometry. For the soft-magnetic swimmer, we use an ellipsoidal head with semi-principal axes of $a = 2\mu m$ and $b = 1\mu m$ made from a soft magnetic material. Attached to the head is a nonmagnetic tapered helical tail of length $8\mu m$ such that the axis of rotational symmetry of the helix is pointing in the $\mathbf{e}_2$ direction. The same geometry is used for the permanent magnetic swimmer. In this case, the magnetic head possesses a permanent dipole of magnitude $V\mathcal{M}_s$ in the $\mathbf{e}_2$ direction. We calculate the mobility matrix of the swimmers using the method of regularized stokeslet. Figure 7.3 shows the discretized surface of the swimmer.

From the experimental point of view, swimming speed needs to be controlled by the field's strength and rotational frequency. These parameters directly affect $\tilde{H}$ and

$\tilde{\Omega}$ in an independent fashion. Hence, we investigate the $\tilde{\Omega} - \tilde{V}_s$ response for a range of $\tilde{H}$. Figure 7.4 illustrates the velocity-frequency response of both the hard- and the soft-magnetic swimmers for $\tilde{H} = n_r$. The response of the hard-magnetic swimmer is linear. This behavior is very similar to that of headless permanent magnetic helices with magnetization in the $\mathbf{e}_2$ direction as was discussed in our earlier work [43]. The response of the soft-magnetic swimmer consists of a relatively short branch of negative velocities (marked with red circles) and a longer branch of positive velocities (marked with blue circles) that exist until the step-out frequency, $\tilde{\Omega}_0$. The blue branch associates with the propulsion solutions. [42, 43] These solutions correspond to when the axis for rotation ($\hat{\mathbf{\Omega}}$) is close to the long axis of the swimmer ($\mathbf{e}_3$). The red branch pertains to the tumbling solutions. [42, 43] Tumbling solutions occur when the axis of rotation is almost perpendicular to the long axis of the swimmer. As demonstrated by the graph, the hard- and soft-magnetic swimmers exhibit very similar responses for the propulsion solutions. Figure 7.4 amplifies two main differences between the soft- and hard-magnetic cases. Firstly, the soft-magnetic swimmer experiences a tumbling solution at lower frequency domain while the hard-magnetic swimmer does not have a stable tumbling solution. Secondly, the step-out frequency of the soft-magnetic swimmer is significantly lower than that of the hard-magnetic swimmers. For the conditions in figure 7.4, the dimensionless step-out frequency is about 0.076 for the hard-magnetic swimmer and about 0.024 for the soft-magnetic swimmer. Above the step-out frequency, steady orbits no longer exist.

We investigated the velocity-frequency response for different values of $\tilde{H}$ and found that they all obtain the same slope as in figure 7.4. However, the step-out frequency of the swimmers change with changing $\tilde{H}$. Figure 7.5 illustrates the nondimensional step-out frequency at different nondimensional field strengths. These results signify another important difference between the hard- and soft-magnetic swimmers. $\tilde{\Omega}_0$ of

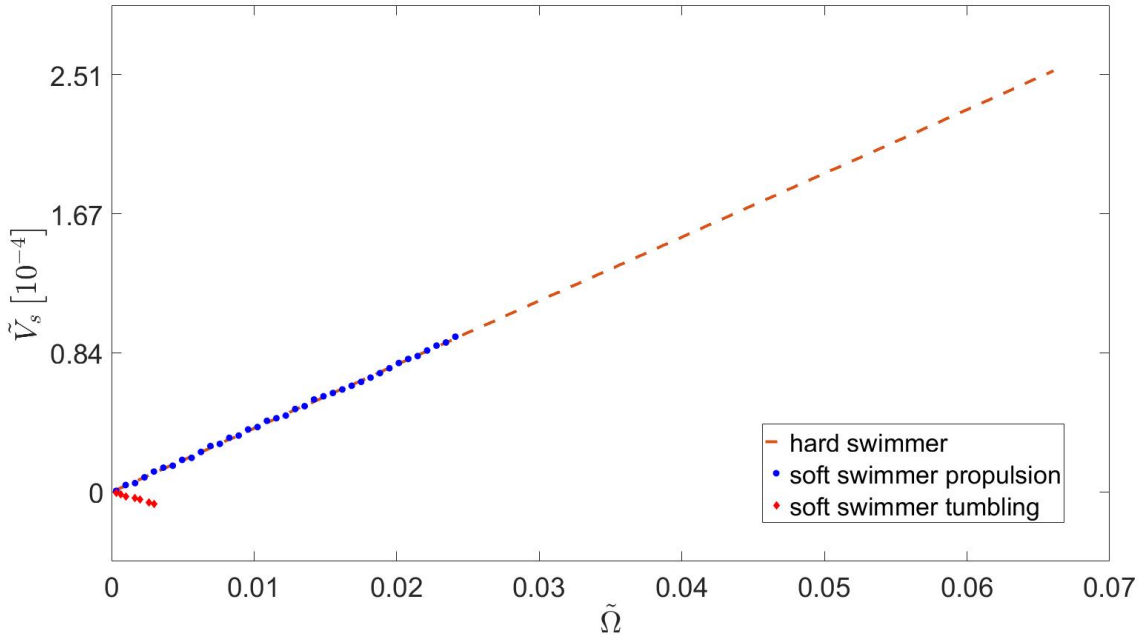

Figure 7.4: The dimensionless swimming velocity versus the dimensionless angular velocity at $\tilde{H} \approx 0.65$ for the hard-magnetic swimmer (orange dashed line) and soft-magnetic swimmer with $|n_r - n_a| \approx 0.48$. The blue circle markers correspond to the propulsion solutions and the red diamond markers correspond to tumbling solutions of the soft-magnetic swimmer.

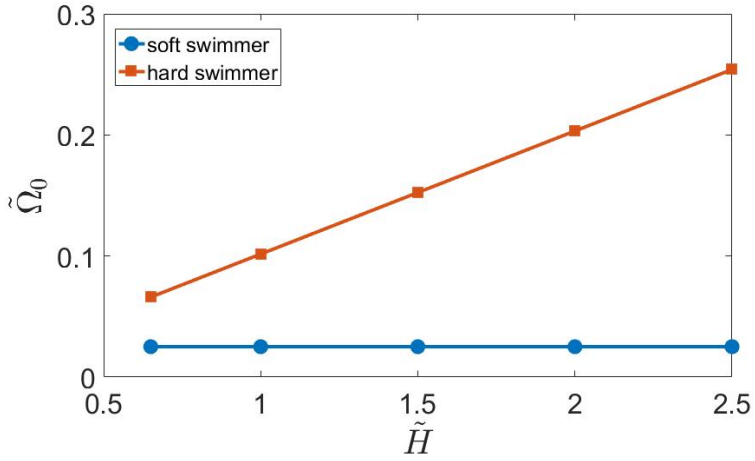

Figure 7.5: Nondimensionalized step-out frequency versus nondimensional magnetic field strength for the hard-magnetic swimmer (orange line and square markers) and the soft-magnetic swimmer (blue line and circular markers).

the hard-magnetic swimmer scales with $\tilde{H}$ and linearly increases with increasing $\tilde{H}$. For the soft-magnetic swimmer, however, $\tilde{\Omega}_0$ does not depend on $\tilde{H}$ for the ranges that we inspected. It is important to mention that the results presented here include all the solutions. The stability of these solutions has not been investigated.

The design implication of these results is that in order to achieve the highest steady-state swimming speed for soft-magnetic swimmers in the saturation regime, the swimmers need to be operated near their step-out frequencies. Additionally, Since the step-out frequency does not depend on the field strength, the swimmer can be operated at any saturating field.

In summary, we found that swimmers, made from saturated hard-magnetic material can exhibit tumbling and propulsion modes and that linear velocity-frequency responses are achievable. For equal field strengths, step-out frequencies of soft-magnetic swimmers are lower than those of their corresponding hard-magnetic swimmers. Finally, with increasing field strength, the step-out frequency increases for the hard-magnetic swimmers but remains constant for the soft-magnetic swimmers in the range

that we studied.

For future work, we are going to analyze the stability of solutions. We will investigate different geometries for the magnetic head and find the effects of various demagnetizing factors on the dynamics of the swimmers. Additionally, we are interested in deriving models for the low-field regime.

Chapter 8

Conclusion

The works presented in this dissertation aim to address two important technical difficulties pertaining to the implementation of magnetic microswimmers for their various biomedical applications.

The first issue is the fabrication of the microrobots. This can be challenging both from the material properties perspective and manufacturing process perspective. The notion of the minimum geometric requirements as was set forth in this work opens up opportunities for simpler and more cost-effective manufacturing processes. Moreover, the concerns about the appropriate size and shapes of swimmers for performance in various environments can be addressed by the modular units suggested in this work. From the material perspective, we developed predictive models for both the hard and soft magnetic material. These models can be used to inform design decisions.

Another practical difficulty associated with magnetic microswimmers is the controllability complications. The swimming speed and direction of swimming are often adjusted by varying the strength and frequency of rotation of the external magnetic field. However, the frequency-velocity response in many cases are not linear. Moreover, experimentalists have reported switching between different swimming modes at the same frequencies as well as wobbling motions which lead to lower swimming veloc-

ities and inefficiencies. Our models help expand our understanding of the dynamics of microswimmers. These models are capable of predicting the swimming velocities for different experimental settings. Based on these models, we explain how linear velocity-frequency responses can be obtained for helical swimmers and how wobbling motions can be minimized. We also illustrated that multiple stable orbits can exist at the same frequencies and showed that multistability can be avoided by changing the angle between the applied field and its axis of rotation. This gives a physics-based model of control. In case of modular microswimmers, our proposed model can help adapt effective strategies for successful assemblies. Our model for soft-magnetic swimmers describes the steady-state orbits and exhibits velocity-frequency response and the effect of the strength of the magnetic field. These predictions can be employed to implement control strategies.

Bibliography

[1] Bernard Dennis Cullity and Chad D Graham. *Introduction to magnetic materials*. John Wiley & Sons, 2011.

[2] Arijit Ghosh, Debadrita Paria, Haobijam Johnson Singh, Pooyath Lekshmy Venugopalan, and Ambarish Ghosh. Dynamical configurations and bistability of helical nanostructures under external torque. *Physical Review E*, 86(3):031401, 2012.

[3] Christian Peters, Olgac Ergeneman, Bradley J Nelson, and Christofer Hierold. Superparamagnetic swimming microrobots with adjusted magnetic anisotropy. In *Micro Electro Mechanical Systems (MEMS), 2013 IEEE 26th International Conference on*, pages 564–567. IEEE, 2013.

[4] Richard D James. Materials science: Magnetic alloys break the rules. *Nature*, 521(7552):298–299, 2015.

[5] Antoire Ferreira, Joel Agnus, Nicolas Chaillet, and J-M Breguet. A smart microrobot on chip: design, identification, and control. *Mechatronics, IEEE/ASME Transactions on*, 9(3):508–519, Sept 2004.

[6] Han Zhang, Dietmar W. Hutmacher, Franck Chollet, Aun Neow Poo, and Etienne Burdet. Microrobotics and mems-based fabrication techniques for scaffold-based tissue engineering. *Macromolecular Bioscience*, 5(6):477–489, 2005.

[7] Gorkem Dogangil, Olgaç Ergeneman, Jake J Abbott, Salvador Pané, Heike Hall, Simon Muntwyler, and Bradley J Nelson. Toward targeted retinal drug delivery with wireless magnetic microrobots. In *Intelligent Robots and Systems, 2008. IROS 2008. IEEE/RSJ International Conference on*, pages 1921–1926, Sept 2008.

[8] Stefano Fusco, George Chatzipirpiridis, Kartik M. Sivaraman, Olga Ergeneman, Bradley J. Nelson, and Salvador Pan. Chitosan electrodeposition for microrobotic drug delivery. *Advanced Healthcare Materials*, 2(7):1037–1044, 2013.

[9] Xinyu Liu, Keekyoung Kim, Yong Zhang, and Yu Sun. Nanonewton force sensing and control in microrobotic cell manipulation. *The International Journal of Robotics Research*, 28(8):1065–1076, 2009.

[10] Sangwon Kim, Famin Qiu, Samhwan Kim, Ali Ghanbari, Cheil Moon, Li Zhang, Bradley J. Nelson, and Hongsoo Choi. Fabrication and characterization of magnetic microrobots for three-dimensional cell culture and targeted transportation. *Advanced Materials*, 25(41):5863–5868, 2013.

[11] Sylvain Martel, Jean-Baptiste Mathieu, Ouajdi Felfoul, Arnaud Chanu, Eric Aboussouan, Samer Tamaz, Pierre Pouponneau, LHocine Yahia, Gilles Beaudoin, Gilles Soulez, and Martin Mankiewicz. Automatic navigation of an untethered device in the artery of a living animal using a conventional clinical magnetic resonance imaging system. *Applied Physics Letters*, 90(11):–, 2007.

[12] MS Grady, MA Howard III, JA Molloy, RC Ritter, EG Quate, and GT Gillies. Nonlinear magnetic stereotaxis: Three-dimensional, invivo remote magnetic manipulation of a small object in canine brain. *Medical Physics*, 17(3):405–415, 1990.

[13] Jean-Baptiste Mathieu, G. Beaudoin, and S. Martel. Method of propulsion of a ferromagnetic core in the cardiovascular system through magnetic gradients generated by an mri system. *Biomedical Engineering, IEEE Transactions on*, 53(2):292–299, Feb 2006.

[14] Edward B Steager, Mahmut Selman Sakar, Dal Hyung Kim, Vijay Kumar, George J Pappas, and Min Jun Kim. Electrokinetic and optical control of bacterial microrobots. *Journal of Micromechanics and Microengineering*, 21(3):035001, 2011.

[15] Dal Hyung Kim, U Kei Cheang, László Kőhidai, Doyoung Byun, Min Jun Kim, et al. Artificial magnetotactic motion control of tetrahymena pyriformis using ferromagnetic nanoparticles: A tool for fabrication of microbiorobots. *Applied Physics Letters*, 97(17):173702, 2010.

[16] Rustem F Ismagilov, Alexander Schwartz, Ned Bowden, and George M Whitesides. Autonomous movement and self-assembly. *Angewandte Chemie*, 114(4):674–676, 2002.

[17] Walter F Paxton, Kevin C Kistler, Christine C Olmeda, Ayusman Sen, Sarah K St. Angelo, Yanyan Cao, Thomas E Mallouk, Paul E Lammert, and Vincent H Crespi. Catalytic nanomotors: Autonomous movement of striped nanorods. *Journal of the American Chemical Society*, 126(41):13424–13431, 2004.

[18] Yang Wang, Rose M Hernandez, David J Bartlett, Julia M Bingham, Timothy R Kline, Ayusman Sen, and Thomas E Mallouk. Bipolar electrochemical mechanism for the propulsion of catalytic nanomotors in hydrogen peroxide solutions. *Langmuir*, 22(25):10451–10456, 2006.

[19] Wei Gao, Mattia D'Agostino, Victor Garcia-Gradilla, Jahir Orozco, and Joseph Wang. Multi-fuel driven janus micromotors. *Small*, 9(3):467–471, 2013.

[20] Jahir Orozco, Victor García-Gradilla, Mattia DAgostino, Wei Gao, Allan Cortes, and Joseph Wang. Artificial enzyme-powered microfish for water-quality testing. *ACS nano*, 7(1):818–824, 2012.

[21] Kalayil Manian Manesh, Maria Cardona, Rodger Yuan, Michael Clark, Daniel Kagan, Shankar Balasubramanian, and Joseph Wang. Template-assisted fabrication of salt-independent catalytic tubular microengines. *ACS nano*, 4(4):1799–1804, 2010.

[22] Alexander A Solovev, Yongfeng Mei, Esteban Bermúdez Ureña, Gaoshan Huang, and Oliver G Schmidt. Catalytic microtubular jet engines self-propelled by accumulated gas bubbles. *Small*, 5(14):1688–1692, 2009.

[23] JG Gibbs and Y-P Zhao. Autonomously motile catalytic nanomotors by bubble propulsion. *Applied Physics Letters*, 94(16):163104–163104, 2009.

[24] Timothy R Kline, Walter F Paxton, Thomas E Mallouk, and Ayusman Sen. Catalytic nanomotors: remote-controlled autonomous movement of striped metallic nanorods. *Angewandte Chemie*, 117(5):754–756, 2005.

[25] Yiying Hong, Nicole MK Blackman, Nathaniel D Kopp, Ayusman Sen, and Darrell Velegol. Chemotaxis of nonbiological colloidal rods. *Physical review letters*, 99(17):178103, 2007.

[26] Gábor Kósa, Péter Jakab, Gábor Székely, and Nobuhiko Hata. Mri driven magnetic microswimmers. *Biomedical microdevices*, 14(1):165–178, 2012.

[27] M Belovs and A Cēbers. Ferromagnetic microswimmer. *Physical Review E*, 79(5):051503, 2009.

[28] Rūdolfs Livanovičs and Andrejs Cēbers. Magnetic dipole with a flexible tail as a self-propelling microdevice. *Physical Review E*, 85(4):041502, 2012.

[29] Marcus Roper, Rémi Dreyfus, Jean Baudry, Marc Fermigier, Jérôme Bibette, and Howard A Stone. Do magnetic micro-swimmers move like eukaryotic cells? *Proceedings of the Royal Society A: Mathematical, Physical and Engineering Science*, 464(2092):877–904, 2008.

[30] Marcus Roper, Rémi Dreyfus, Jean Baudry, Marc Fermigier, Jérôme Bibette, and Howard A Stone. On the dynamics of magnetically driven elastic filaments. *Journal of Fluid Mechanics*, 554:167–190, 2006.

[31] Feodor Y Ogrin, Peter G Petrov, and C Peter Winlove. Ferromagnetic microswimmers. *Physical review letters*, 100(21):218102, 2008.

[32] Hassan Masoud and Alexander Alexeev. Modeling magnetic microcapsules that crawl in microchannels. *Soft Matter*, 6(4):794–799, 2010.

[33] Charles E Sing, Lothar Schmid, Matthias F Schneider, Thomas Franke, and Alfredo Alexander-Katz. Controlled surface-induced flows from the motion of self-assembled colloidal walkers. *Proceedings of the National Academy of Sciences*, 107(2):535–540, 2010.

[34] Pietro Tierno, Oriol Güell, Francesc Sagués, Ramin Golestanian, and Ignacio Pagonabarraga. Controlled propulsion in viscous fluids of magnetically actuated colloidal doublets. *Physical Review E*, 81(1):011402, 2010.

[35] Li Zhang, Tristan Petit, Yang Lu, Bradley E Kratochvil, Kathrin E Peyer, Ryan Pei, Jun Lou, and Bradley J Nelson. Controlled propulsion and cargo transport of rotating nickel nanowires near a patterned solid surface. *ACS nano*, 4(10):6228–6234, 2010.

[36] Jake J Abbott, Kathrin E Peyer, Marco Cosentino Lagomarsino, Li Zhang, Lixin Dong, Ioannis K Kaliakatsos, and Bradley J Nelson. How should microrobots swim? *The International Journal of Robotics Research*, 28(11-12):1434–1447, 2009.

[37] Prajnaparamita Dhar, Cheryl D Swayne, Thomas M Fischer, Timothy Kline, and Ayusman Sen. Orientations of overdamped magnetic nanorod-gyroscopes. *Nano letters*, 7(4):1010–1012, 2007.

[38] Kathrin Eva Peyer, Li Zhang, Bradley E Kratochvil, and Bradley J Nelson. Non-ideal swimming of artificial bacterial flagella near a surface. In *Robotics and Automation (ICRA), 2010 IEEE International Conference on*, pages 96–101. IEEE, 2010.

[39] Konstantin I Morozov and Alexander M Leshansky. The chiral magnetic nanomotors. *Nanoscale*, 6(3):1580–1588, 2014.

[40] Soichiro Tottori, Li Zhang, Kathrin E Peyer, and Bradley J Nelson. Assembly, disassembly, and anomalous propulsion of microscopic helices. *Nano letters*, 13(9):4263–4268, 2013.

[41] Yi Man and Eric Lauga. The wobbling-to-swimming transition of rotated helices. *Physics of Fluids (1994-present)*, 25(7):071904, 2013.

[42] Farshad Meshkati and Henry Chien Fu. Modeling rigid magnetically rotated microswimmers: Rotation axes, bistability, and controllability. *Physical Review E*, 90(6):063006, 2014.

[43] Henry C Fu, Mehdi Jabbarzadeh, and Farshad Meshkati. Magnetization directions and geometries of helical microswimmers for linear velocity-frequency response. *Physical Review E*, 91(4):043011, 2015.

[44] Arijit Ghosh, Pranay Mandal, Suman Karmakar, and Ambarish Ghosh. Analytical theory and stability analysis of an elongated nanoscale object under external torque. *Physical Chemistry Chemical Physics*, 15(26):10817–10823, 2013.

[45] Li Zhang, Jake J Abbott, Lixin Dong, Bradley E Kratochvil, Dominik Bell, and Bradley J Nelson. Artificial bacterial flagella: Fabrication and magnetic control. *Applied Physics Letters*, 94(6):064107, 2009.

[46] U Kei Cheang, Farshad Meshkati, Dalhyung Kim, Min Jun Kim, and Henry Chien Fu. Minimal geometric requirements for micropropulsion via magnetic rotation. *Physical Review E*, 90(3):033007, 2014.

[47] U Kei Cheang, Farshad Meshkati, Hoyeon Kim, Kyoungwoo Lee, Henry Chien Fu, and Min Jun Kim. Versatile microrobotics using simple modular subunits. *Scientific Reports*, 6, 2016.

[48] David Jiles. *Introduction to magnetism and magnetic materials*. CRC press, 2015.

[49] Edward M Purcell. Life at low Reynolds number. *Am. J. Phys*, 45(1):3–11, 1977.

[50] Prasanta Kumar Banerjee and Roy Butterfield. *Boundary element methods in engineering science*, volume 17. McGraw-Hill London, 1981.

[51] Ricardo Cortez. The method of regularized stokeslets. *SIAM Journal on Scientific Computing*, 23(4):1204–1225, 2001.

[52] Ricardo Cortez, Lisa Fauci, and Alexei Medovikov. The method of regularized stokeslets in three dimensions: analysis, validation, and application to helical swimming. *Physics of Fluids (1994-present)*, 17(3):031504, 2005.

[53] Yunkyong Hyon, Thomas R Powers, Roman Stocker, Henry C Fu, et al. The wiggling trajectories of bacteria. *Journal of Fluid Mechanics*, 705:58–76, 2012.

[54] Marco Leoni, Jurij Kotar, Bruno Bassetti, Pietro Cicuta, and Marco Cosentino Lagomarsino. A basic swimmer at low Reynolds number. *Soft Matter*, 5(2):472–476, 2009.

[55] Nobuhito Mori, Kaori Kuribayashi, and Shoji Takeuchi. Artificial flagellates: Analysis of advancing motions of biflagellate micro-objects. *Applied Physics Letters*, 96(8):083701, 2010.

[56] Charles E Sing, Lothar Schmid, Matthias F Schneider, Thomas Franke, and Alfredo Alexander-Katz. Controlled surface-induced flows from the motion of self-assembled colloidal walkers. *Proceedings of the National Academy of Sciences*, 107(2):535–540, 2010.

[57] Wang Xi, Alexander A Solovev, Adithya N Ananth, David H Gracias, Samuel Sanchez, and Oliver G Schmidt. Rolled-up magnetic microdrillers: towards remotely controlled minimally invasive surgery. *Nanoscale*, 5(4):1294–1297, 2013.

[58] Z Vaituzis and RN Doetsch. Relationship between cell wall, cytoplasmic membrane, and bacterial motility. *Journal of bacteriology*, 100(1):512–521, 1969.

[59] Li Zhang, Elisabeth Ruh, Detlev Grützmacher, Lixin Dong, Dominik J Bell, Bradley J Nelson, and Christian Schönenberger. Anomalous coiling of sige/si and sige/si/cr helical nanobelts. *Nano letters*, 6(7):1311–1317, 2006.

[60] Soichiro Tottori, Li Zhang, Famin Qiu, Krzysztof K Krawczyk, Alfredo Franco-Obregón, and Bradley J Nelson. Magnetic helical micromachines: fabrication, controlled swimming, and cargo transport. *Advanced materials*, 24(6):811–816, 2012.

[61] Ambarish Ghosh and Peer Fischer. Controlled propulsion of artificial magnetic nanostructured propellers. *Nano letters*, 9(6):2243–2245, 2009.

[62] U Kei Cheang, Dheeraj Roy, Jun Hee Lee, and Min Jun Kim. Fabrication and magnetic control of bacteria-inspired robotic microswimmers. *Applied Physics Letters*, 97(21):213704, 2010.

[63] Fatma Zeynep Temel and Serhat Yesilyurt. Magnetically actuated micro swimming of bio-inspired robots in mini channels. In *Mechatronics (ICM), 2011 IEEE International Conference on*, pages 342–347. IEEE, 2011.

[64] Piotr Garstecki, Pietro Tierno, Douglas B Weibel, Francesc Sagués, and George M Whitesides. Propulsion of flexible polymer structures in a rotating magnetic field. *Journal of Physics: Condensed Matter*, 21(20):204110, 2009.

[65] Rémi Dreyfus, Jean Baudry, Marcus L Roper, Marc Fermigier, Howard A Stone, and Jérôme Bibette. Microscopic artificial swimmers. *Nature*, 437(7060):862–865, 2005.

[66] Wei Gao, Daniel Kagan, On Shun Pak, Corbin Clawson, Susana Campuzano, Erdembileg Chuluun-Erdene, Erik Shipton, Eric E Fullerton, Liangfang Zhang, Eric Lauga, et al. Cargo-towing fuel-free magnetic nanoswimmers for targeted drug delivery. *small*, 8(3):460–467, 2012.

[67] On Shun Pak, Wei Gao, Joseph Wang, and Eric Lauga. High-speed propulsion of flexible nanowire motors: Theory and experiments. *Soft Matter*, 7(18):8169–8181, 2011.

[68] Eleftherios P Diamandis and Theodore K Christopoulos. The biotin-(strept) avidin system: principles and applications in biotechnology. *Clinical chemistry*, 37(5):625–636, 1991.

[69] Joyce Wong, Ashutosh Chilkoti, and Vincent T Moy. Direct force measurements of the streptavidin–biotin interaction. *Biomolecular engineering*, 16(1):45–55, 1999.

[70] Kenneth Kam-Wing Lo, Wai-Ki Hui, Chi-Keung Chung, Keith Hing-Kit Tsang, Terence Kwok-Ming Lee, and Dominic Chun-Ming Ng. Luminescent transition metal polypyridine biotin complexes. *Journal of the Chinese Chemical Society*, 53(1):53–65, 2006.

[71] Yu Sun, Stefan Duthaler, and Bradley J Nelson. Autofocusing in computer microscopy: selecting the optimal focus algorithm. *Microscopy research and technique*, 65(3):139–149, 2004.

[72] Howard C Berg. *Random walks in biology*. Princeton University Press, 1993.

[73] John Happel and Howard Brenner. *Low Reynolds number hydrodynamics: with special applications to particulate media*, volume 1. Springer, 1983.

[74] U Kei Cheang, Dejan Milutinovic, Jongeun Choi, and Minjun Kim. Towards model-based control of achiral microswimmers. In *Proceedings of the ASME 2014 Dynamic Systems and Control Conference*.

[75] Arijit Ghosh, Debadrita Paria, Govindan Rangarajan, and Ambarish Ghosh. Velocity fluctuations in helical propulsion: how small can a propeller be. *The journal of physical chemistry letters*, 5(1):62–68, 2013.

[76] DL Fan, FQ Zhu, RC Cammarata, and CL Chien. Electric tweezers. *Nano Today*, 6(4):339–354, 2011.

[77] Eric E Keaveny, Shawn W Walker, and Michael J Shelley. Optimization of chiral structures for microscale propulsion. *Nano letters*, 13(2):531–537, 2013.

[78] Stephen Childress. *Mechanics of swimming and flying*, volume 2. Cambridge University Press, 1981.

[79] Bruce Rodenborn, Chih-Hung Chen, Harry L Swinney, Bin Liu, and HP Zhang. Propulsion of microorganisms by a helical flagellum. *Proceedings of the National Academy of Sciences*, 110(5):E338–E347, 2013.

[80] Konstantin I Morozov and Alexander M Leshansky. Dynamics and polarization of superparamagnetic chiral nanomotors in a rotating magnetic field. *Nanoscale*, 6(20):12142–12150, 2014.

[81] Mark Yim, Ying Zhang, and David Duff. Modular robots. *IEEE Spectrum*, 39(2):30–34, 2002.

[82] Abraham Clearfield. Recent advances in metal phosphonate chemistry. *Current Opinion in Solid State and Materials Science*, 1(2):268–278, 1996.

[83] Rajesh Singh and James W Lillard. Nanoparticle-based targeted drug delivery. *Experimental and molecular pathology*, 86(3):215–223, 2009.

[84] Mei Lin Tan, Peter FM Choong, and Crispin R Dass. Recent developments in liposomes, microparticles and nanoparticles for protein and peptide drug delivery. *Peptides*, 31(1):184–193, 2010.

[85] You Han Bae and Kinam Park. Targeted drug delivery to tumors: myths, reality and possibility. *Journal of Controlled Release*, 153(3):198, 2011.

[86] Conroy Sun, Jerry SH Lee, and Miqin Zhang. Magnetic nanoparticles in mr imaging and drug delivery. *Advanced drug delivery reviews*, 60(11):1252–1265, 2008.

[87] Jon Dobson. Magnetic nanoparticles for drug delivery. *Drug development research*, 67(1):55–60, 2006.

[88] J Gray and GJ Hancock. The propulsion of sea-urchin spermatozoa. *Journal of Experimental Biology*, 32(4):802–814, 1955.

[89] K Berk Yesin, Philipp Exner, Karl Vollmers, and Bradley J Nelson. Design and control of in-vivo magnetic microrobots. In *International Conference on Medical Image Computing and Computer-Assisted Intervention*, pages 819–826. Springer, 2005.

[90] JE Avron, O Kenneth, and DH Oaknin. Pushmepullyou: an efficient microswimmer. *New Journal of Physics*, 7(1):234, 2005.

[91] Ali Najafi and Ramin Golestanian. Simple swimmer at low Reynolds number: Three linked spheres. *Physical Review E*, 69(6):062901, 2004.

[92] Mahmut Selman Sakar, Edward B Steager, Dal Hyung Kim, Min Jun Kim, George J Pappas, Vijay Kumar, et al. Single cell manipulation using ferromagnetic composite microtransporters. *Applied physics letters*, 96(4):043705, 2010.

[93] Hsi-Wen Tung, Kathrin E Peyer, David F Sargent, and Bradley J Nelson. Noncontact manipulation using a transversely magnetized rolling robot. *Applied Physics Letters*, 103(11):114101, 2013.

[94] Bradley J Nelson, Ioannis K Kaliakatsos, and Jake J Abbott. Microrobots for minimally invasive medicine. *Annual review of biomedical engineering*, 12:55–85, 2010.

[95] Kathrin E Peyer, Li Zhang, and Bradley J Nelson. Localized non-contact manipulation using artificial bacterial flagella. *Applied Physics Letters*, 99(17):174101, 2011.

[96] Wei Gao, Xiaomiao Feng, Allen Pei, Christopher R Kane, Ryan Tam, Camille Hennessy, and Joseph Wang. Bioinspired helical microswimmers based on vascular plants. *Nano letters*, 14(1):305–310, 2013.

[97] Xiaohui Yan, Qi Zhou, Jiangfan Yu, Tiantian Xu, Yan Deng, Tao Tang, Qian Feng, Liming Bian, Yan Zhang, Antoine Ferreira, et al. Magnetite nanostructured porous hollow helical microswimmers for targeted delivery. *Advanced Functional Materials*, 25(33):5333–5342, 2015.

[98] U Kei Cheang, Kyoungwoo Lee, Anak Agung Julius, and Min Jun Kim. Multiple-robot drug delivery strategy through coordinated teams of microswimmers. *Applied physics letters*, 105(8):083705, 2014.

[99] Li Zhang, Bradley J Nelson, and Lixin Dong. Magnetic-field-based self-assembly. In *Encyclopedia of Nanotechnology*, pages 1264–1275. Springer, 2012.

[100] Jake J Abbott, Olgaç Ergeneman, Michael P Kummer, Ann M Hirt, and Bradley J Nelson. Modeling magnetic torque and force for controlled manipulation of soft-magnetic bodies. *IEEE Transactions on Robotics*, 23(6):1247–1252, 2007.